

INTEGRATING NOVEL RHEOLOGICAL TOOLS WITH MICROSCOPY TO
CHARACTERIZE VISCOELASTIC PROPERTIES
OF COMPLEX MATERIALS

by

Shalaka Karbhari Kale

A thesis submitted to the Faculty and the Board of Trustees of the Colorado School of Mines in partial fulfillment of the requirements for the degree of Doctor of Philosophy
(Chemical Engineering)

Golden, Colorado

Date _____

Signed: _____

Shalaka Karbhari Kale

Signed: _____

Dr. Joseph R. Samaniuk

Thesis Advisor

Golden, Colorado

Date _____

Signed: _____

Dr. Anuj Chauhan

Professor and Department Head

Department of Chemical and Biological Engineering

ABSTRACT

Rheological property of any material is the mechanical response when it undergoes stress or deformation. Characterizing these properties is essential because it can help in optimizing the formulation and processing of the materials. Over the years, different rheological techniques have evolved, however, with the growth of science and technology, the realm of material characterization faces new challenges, and this demands for developing innovative rheological tools. In this thesis, we identify certain limitations of the available techniques in the field of microrheology and interfacial rheology and overcome them using the novel rheological techniques that we have developed.

Passive particle tracking microrheology (PTM) is a technique that uses Brownian motion of colloidal probe particles to characterize the mechanical properties of materials at micron length scales. However, this method cannot be used in higher modulus materials ($G^* > 10^1$ Pa) because the particles experience restricted Brownian motion. To overcome this, we have developed a form of active microrheology that uses electromagnetic tweezers to induce an artificial thermal noise on a superparamagnetic particle in the form of a random white noise signal. The main advantage of this technique is that the induced random motion of the particle allows one to use conventional hydrodynamic models to obtain material functions without needing to measure a defined strain field.

Fluid-fluid interfaces undergo variety of deformations during the processing steps. Often the contribution of individual deformation type needs to be separated but it's difficult to achieve with most of the traditional methods. Further, interfacial rheological properties of complex interfaces are strongly influenced by the film microstructure. Experimental investigations for

isolating the deformation type, correlating interfacial morphology and rheology are challenging. We developed a miniaturized radial Langmuir trough to study complex fluid-fluid interfaces under purely dilatation deformations that operates in tandem with a conventional inverted microscope for simultaneous interfacial visualization. In our findings, we were able to evaluate rheological properties like compressional and viscoelastic dilatational modulus of complex interfaces and were able to correlate them with the underlying interfacial microstructure.

TABLE OF CONTENTS

ABSTRACT	iii
LIST OF FIGURES	viii
ACKNOWLEDGEMENTS	xiv
CHAPTER 1 INTRODUCTION AND BACKGROUND	1
1.1 Why Rheology?	1
1.2 Methods in Rheology	2
1.3 Thesis Organization and Major Contributions	3
1.4 Background	5
1.4.1 Rheology Basics	5
1.4.2 Microrheology	9
1.4.2.1 Principles of Passive Microrheology	10
1.4.2.2 Passive Microrheology Techniques	14
1.4.2.3 Active Microrheology Techniques	16
1.4.3 Thesis Statement I	19
1.4.4 Interfacial Rheology	22
1.4.4.1 Interfacial Rheology Techniques	23
1.4.5 Thesis Statement II	25
CHAPTER 2 ACTIVE PARTICLE TRACKING MICRORHEOLOGY USING ARTIFICIAL THERMAL NOISE	26
2.1 Introduction and Background	26
2.2 Materials and Methods	33
2.2.1 Single-coil Tweezer Setup	33
2.2.2 Force Calibration	36
2.2.3 Displacement Analysis	38

2.3	Results and Discussions	40
2.4	Conclusions	45
CHAPTER 3 A MINIATURIZED RADIAL LANGMUIR TROUGH FOR SIMULTANEOUS DILATATIONAL DEFORMATION AND INTERFACIAL MICROSCOPY		
		47
3.1	Introduction	47
3.2	Instrumental Concept and Design	53
3.3	Materials and Methods	58
3.3.1	Silanization	58
3.3.2	Sample Preparation	59
3.3.3	Interface Preparation	59
3.3.4	Surface Tension Measurement	60
3.3.5	Sample Visualization	61
3.4	Results and Discussions	62
3.4.1	PtBMA at Air-Water Interface	62
3.4.2	DPPC at Air-Water Interface	70
3.4.3	Capillary Deformation and Surface Pressure	78
3.5	Conclusions	82
CHAPTER 4 OSCILLATORY DILATATIONAL DEFORMATIONS OF FLUID-FLUID INTERFACES USING RADIAL LANGMUIR TROUGH		
		85
4.1	Introduction	86
4.2	Methods and Materials	89
4.2.1	Dilatational Area Oscillations	90
4.2.2	Sample Preparation	92
4.3	Results and Discussions	93
4.3.1	Dilatational Oscillatory Measurements	94
4.3.2	Visualization Experiments	100

4.4	Conclusions.....	102
CHAPTER 5 FUTURE WORK.....		104
5.1	Artificial Thermal Noise for Viscoelastic Materials	104
5.2	Interactions of Lipid Membranes and 2D Particles	105
CHAPTER 6 CONCLUSIONS.....		108
REFERENCES CITED.....		111
APPENDIX A SUPPLEMENTARY MATERIAL MAGNETIC TWEEZERS		127
A.1	Estimating the Cutoff Frequency	127
A.2	MATLAB Algorithm for Randomizing ‘Directed’ Displacements.....	127
A.3	Scanning Electron Microscopy (SEM) of Probe Particles.....	130
APPENDIX B SUPPLEMENTARY MATERIAL RADIAL LANGMUIR TROUGH.....		131
B.1	SolidWorks Drawings for the Radial Trough Parts	131
B.2	Calibration and Interfacial Area Calculations.....	135
B.3	Error Propagation.....	136
B.4	Dilute PtBMA Sample at Air-Water Interface.....	137
B.5	Reproducible DPPC Surface Pressure Measurement	138
B.6	Dilute DPPC Sample at Air-Water Interface	139
B.7	Reproducible Compression-Expansion Curves of Concentrated DPPC Sample.....	140
B.8	DPPC Visualization During Expansion	141
B.9	Meniscus Contour Plots/ Interaction of Menisci	142
B.10	Contact Angle Measurement.....	143
B.11	Combining Clean Water and PtBMA/DPPC Film Compression Measurement.....	144
APPENDIX C ZABER CONSOLE SCRIPTS.....		146
APPENDIX D COPYRIGHT PERMISSIONS		150

LIST OF FIGURES

Figure. 1.1	Preliminary MSD versus time data set of 0.45 wt.% of calcium alginate gel. The black curve is the passive PTM measurement, and the red curve is MSD data obtained after applying white noise signal. 20	20
Figure 2.1	a) Schematic illustration that explains the definition of lag time (τ) b) x-direction passive MSD data as a function of τ of a single particle trajectory for different calibration (Newtonian) oils, 0.1 Pa·s (yellow circles), 1.8 Pa·s (blue circles), 35.1 Pa·s (green circles) and 103 Pa·s (red circles). Gray box represents the operating range of passive PTM for our setup. 28	28
Figure 2.2	a) Schematic setup of the single-coil electromagnetic tweezer used to generate artificial thermal noise b) (Left) White noise signal with an average current of 0.75A, (Right) Random Gaussian distribution (green line) of the same white noise signal with a Gaussian fit (solid black line). 34	34
Figure 2.3	a) Force calibration for single-coil electromagnetic tweezer as a function of input current b) Illustration of 1d particle diffusion in absence (top) and presence (bottom) of electromagnetic tweezer. 36	36
Figure 2.4	a)x-MSD data as a function of lag time estimated for active microrheological measurement performed on a 35.1 Pa·s calibration oil using a white noise signal with average current of 0.5 A. Orange data is Directed MSD (with slope 2) and green data is Randomized MSD (with slope 1) b) x-position versus lag time data for the same data set in part a. c) Gaussian random distribution of the displacements of a particle present in 35.1 Pa·s calibration oil evaluated at lag frame 1. Orange data shows the Directed displacements with a non-zero mean displacement while the green data shows Randomized displacements with a mean displacement of zero. Black solid line and black dashed line are the Gaussian fit for the directed and randomized displacement distributions respectively. d) Passive and active x-MSD measurements for 35.1 Pa·s Newtonian fluid. Active measurements are performed on a same single particle with three different white noise signals with average currents, 0.25 A (blue solid circles), 0.5 A (yellow solid circles) and 0.75 A (red solid circles). Gray shaded area is the typical operating range of passive PTM setup. 40	40
Figure 3.1	Schematic representation of compression assembly. a) Exploded view: Base plate holds six fingers that support the elastic barrier at each finger-tip. Inset shows schematic side-view of a single finger and the position of the elastic barrier. Support plate couples the base plate and optical diaphragm and holds	

a linear stepper-motor that actuates compression. OD stands for outer diameter. b) Assembled view: Support plate is fixed to the base plate with M2.5×15 mm screws while the optical diaphragm is compression fit. Optical diaphragm surrounds the finger-heads and is actuated by the stepper-motor. The dashed, double-arrow line indicates the motion of the stepper-motor. The optical diaphragm further actuates the finger motion and thus the elastic barrier position. 54

Figure 3.2 Schematic illustrations of the stainless-steel sample container that serves as the sample trough. (Left) Exploded view with all the components of the sample container. Parts are compression fit with M3×8 mm screws. (Right) The assembled view shows the various internal diameters of rings that create pinning points for fluid-fluid interfaces. 55

Figure 3.3 Illustrations of the top view (left) and side view (right) of the base plate seated on the sample container with an air-water interface. Top view shows the fully open configuration of the radial trough. Open holes in the base plate that align with the M3×8 mm screws of the sample container fix the position of base plate over the sample chamber and set screws in threaded holes in the base plate allow for height adjustment between the sample container and the base plate. In open configuration, the six fingers and elastic barrier form a hexagonal interfacial area and are held in this default position by using the elastic bands. Each finger is fixed on to a linear slide bearing (see side view). The dashed, double-arrow lines indicate the direction of the movement of the fingers. OD stands for outer diameter. 56

Figure. 3.4 a) Surface pressure (π) as a function of mean monomer area for PtBMA at air-water interface is plotted on the primary y-axis. Both the radial trough measurements (orange line) and rectangular trough measurements (green line) are the initial compression cycle. The grey error bars (radial trough data) and black error bars (rectangular trough data) indicate the uncertainty in calculating mean monomer area. Filled squares are plotted against the secondary y-axis are the normalized capillary radius (R_n) as a function of mean monomer area. b) Micrographs for PtBMA at an air-water interface taken independently during first compression cycle in the radial trough using phase contrast microscopy. Images 1, 2, 3 and 4 are captured at corresponding mean monomer areas indicated as in a). The dashed ovals indicate a common reference point in each image. Solid and dotted arrows indicate wrinkling formed during interfacial compression. Solid arrows point towards larger wrinkling period while the dotted arrows point towards smaller wrinkling period. Scale bars represent 250 μm . c) Micrograph of the same PtBMA interface taken at the full compression point 4 (see part a, interfacial area $\sim 120.2 \text{ mm}^2$) but at a different location of the interface.

Dotted arrows show the small wrinkling periods that are used to average the low wavelength (λ_{low}) value. 63

Figure 3.5 a) Surface pressure (π) as a function of mean molecular area for DPPC at an air-water interface. Three consecutive continuous compressions (orange line) measured using the radial Langmuir trough are shown. The grey error bars indicate the uncertainty in estimating the mean molecular area. b) The green line indicates DPPC surface pressure measured using the rectangular Langmuir trough, while the orange line is the same second compression curve that is plotted in a). Black error bars on rectangular trough data set represent the uncertainty in estimating mean molecular area of DPPC. The secondary y-axis data (solid blue squares) is the measured normalized capillary radius (R_n) as a function of mean molecular area. 70

Figure 3.6 Micrographs of DPPC at an air-water interface captured independently using epifluorescence microscopy. The top row contains images acquired during the first compression cycle in the radial Langmuir trough, and the bottom row has images taken during the second (subsequent) compression cycle. Approximate mean molecular area for each image is shown at the bottom such that every column of micrographs is captured at same compression point. Scale bars for main micrographs represent 50 μm . Inset images are digitally magnified regions of the corresponding main micrographs with scale bar representing 20 μm . These inset images are enhanced with higher contrast for improved visibility. 76

Figure 3.7 Effect of silanization of the elastic barrier and the finger-tips on the apparent surface pressure (π) measurement of a clean air-water interface in the radial Langmuir trough. Apparent π , is plotted as a function of the normalized separation distance between the finger tips and the Wilhelmy rod, R_f/R_{f0} , where R_{f0} is the maximum value of R_f . The inset illustration shows the definition of the measured values of R_f , and R_b . The width of a finger-tip cross section, h , is also indicated. Orange circles represent apparent π for the non-silanized system, while the black circles represent the silanized system. Values for normalized capillary radius (R_n) are shown with the dashed black line and are associated with the secondary y-axis. Error bars represent the maximum and minimum surface pressures measured between the two set of measurements..... 80

Figure 4.1 Surface pressure (π) of DPPC at air-water interface as a function of mean molecular area. The dotted lines indicate the different phase regions of DPPC during compression of the interface. The black solid circle represents lower surface coverage, and the red solid circle is a higher surface coverage. The

	corresponding surrounding boundaries (black oval and red oval) are the region of oscillation amplitude.	94
Figure 4.2	a) Induced sinusoidal area oscillations as a function of time. The y-axis represents the physical oscillatory signal expressed as mean molecular area of DPPC. Black curve is induced oscillations at lower DPPC coverage while red curve is for higher DPPC coverage. b) Surface pressure (π) response of the DPPC air- interface measured with Wilhelmy balance. Black curve is the π response at low DPPC coverage and red curve the π response at high DPPC coverage. In both part a and part b, locations 1, 2 and 3 are the points where DPPC microstructures were recorded in-situ.....	95
Figure 4.3	DPPC at air-water interface visualized under fluorescent microscopy. Images 1, 2 and 3 in each row correspond to location in Fig. 4.2. The scale bar represents a size of 50 μm and the total width of the image is close to 320 μm . In both top row ($A_0 \sim 50 \text{ \AA}^2$) and bottom row ($A_0 \sim 34 \text{ \AA}^2$), location 1 indicates the microstructure at A_0 before the oscillations begin, 2 is the microstructure at the highest compression region in small amplitude oscillation and 3 is the microstructure again at A_0 but after oscillations are completed.....	101
Figure A.1	Yellow circles show the power estimated for the electromagnetic coil as a function of frequency. Power is calculated from the amplitude ratio of a sine wave at 1A evaluated at various frequencies. The cutoff frequency is approximately 60Hz at -3dB. Based on this, the operational or usable signal frequency that is selected for this work is 25Hz.	127
Figure A.2	SEM image of 1 μm diameter superparamagnetic probe particles.	130
Figure B.1	a) Calibration curve for estimating radial distance, R_b , as a function of stepper-motor position, L for the radial Langmuir trough. b) Illustration of the top view of air-water interface in presence of platinum Wilhelmy rod. Inset is the magnification of finger-tip section that sits at the interface. The shaded region is occupied the elastic barrier.	135
Figure B.2	Surface pressure (π) of compression curve with dilute PtBMA sample (ten times low concentration i.e., 0.02 mg/mL) and initial surface coverage of $\sim 0.75 \text{ mg/m}^2$ obtained using radial Langmuir trough. Error bars represent percentage uncertainty of 5.55% in estimating the mean monomer area. The curve does not show any apparent rise in π	137
Figure B.3	Surface pressure (π) measurement of independently prepared DPPC at air-water interface obtained using radial Langmuir trough. Orange line data shows the consecutive compressions while blue line data shows the	

consecutive expansions. Arrows indicate the order of compression and expansion. Error bars represent percentage uncertainty of 6.05% in estimating the mean molecular area. For convenience error bars are only provided for first compression and expansion. Initial surface coverage is $\sim 0.75 \text{ mg/m}^2$ 138

Figure B.4 Surface pressure (π) of first and second compression curves of dilute DPPC sample with ten times low concentration (0.02 mg/mL) and initial surface coverage of $\sim 1.1 \text{ mg/m}^2$ obtained using radial Langmuir trough. Error bars represent percentage uncertainty of 6.35% in estimating the mean molecular area. The curve does not show an apparent rise in π 139

Figure B.5 Surface pressure (π) measurement of relatively concentrated DPPC (0.2 mg/mL) at air-water interface showing three continuous compression-expansion curves. Orange line data shows the consecutive compressions while blue line data shows the consecutive expansions. Arrows indicate the order of compression and expansion. Error bars represent percentage uncertainty of 6.5% in estimating the mean molecular area. For convenience error bars are only provided for the first compression-expansion cycle. Initial surface coverage is $\sim 1.1 \text{ mg/m}^2$ 140

Figure B.6 Micrographs of DPPC at air-water interface during expansion. The images are acquired using radial Langmuir trough and are of the same interface whose compression micrographs are reported in Fig. 6 of main manuscript. 1st expansion is imaged with 40 \times objective while 2nd expansion was imaged with 100 \times objective. 141

Figure B.7 Theoretical meniscus shape of an air-water interface. Interface pinning height (z) due to meniscus formation is normalized by the capillary length scale (C_L) of water at 20 °C i.e. 2.72 mm, and is plotted as a function of normalized separation distance (R_f) between the Wilhelmy rod and finger-tip. Meniscus shape at the finger-tip and the Wilhelmy rod are calculated separately. The inset illustration qualitatively shows a side view of the meniscus formation at the air-water interface in the presence of the finger-tip, elastic barrier and the Wilhelmy rod. The pinning height (z) as a function of contact angle (θ_0) is calculated for three different values of θ_0 for the finger tips. $\theta_0 = 0^\circ$ (solid orange line) for complete wetting, $\theta_0 = 50^\circ$ (dashed green line) and $\theta_0 = 85^\circ$ (dashed purple line). For the platinum Wilhelmy rod we plot the result for constant contact angle of $\theta_0 = 0^\circ$ (solid black line). 142

Figure B.8 Contact angle measurement for not silanized (pre-treated) and silanized (post treated) finger and elastic barrier processed using ImageJ software. The estimated value for contact angle (θ_0) is mentioned on the top right corner of each image. 143

Figure B.9 Apparent surface pressure (π , solid line) during compression, is plotted as a function of the normalized separation distance between the finger tips and the Wilhelmy rod, R_f/R_{f0} , where R_{f0} is the maximum value of R_f . Red, green and black lines are the data set obtained with radial trough for PtBMA at air-water interface (Fig. 3.4a), DPPC at air-water interface (Fig. 3.5b) and clean water (Fig. 3.7) interface respectively. Gray error bars for the clean water data shows the maximum and minimum values of π obtained from two independent measurements. The secondary y-axis represents the normalized capillary radius (R_n , dashed lines). The interface is compressed such that the compression ratio is approximately 4. 144

ACKNOWLEDGEMENTS

It is a genuine pleasure to express my deep sense of thanks and gratitude to my advisor Dr. Joseph Samaniuk. Your knowledge and experience have inspired me in all times of my academic research and daily life. This work has been a roller-coaster ride filled with uncertainty, excitement, and novelty. Truly, your endless support through all of this has been the sole reason for this dissertation to reach its culmination. Your encouragement, optimism, understanding during the toughest time and above all your balanced approach has immensely helped me towards the completion of this work. I greatly appreciate you for all the things that you have taught me in the last five years, and they will remain an integral part of my life. I am forever grateful to you for providing me the opportunity to work with you. I am also thankful to my committee members, Dr. Melissa Krebs, Dr. Andrew Petruska, and Dr. Ning Wu for their time and patience. Knowingly or unknowingly, you all have played a key role towards my scientific development.

Thank you to my dear lab mates, David Goggin, Ben Appleby, Jess Troxler and Amy Chacon. David, I vividly remember the day I came to know that you were going to be my lab mate and honestly, I couldn't be happier! Since that day and even after you graduated you have always helped me in all capacities. Thank you for the thorough research discussions, for never judging my failures and simply for being there for me. I will forever cherish our friendship and I know no matter which part of the world we live in I can always count on you. Ben, I am so glad to see how our bond grew over the years. Thank you for patiently listening to my life stories, for sharing your opinions in both research and life, for your willingness to try Indian cuisine and for

being friends with me. Jess and Amy, thank you for always willing to provide suggestions and offering help.

A heartfelt thank you to Andrew Cope (Drew), the wonderful undergraduate researcher who assisted me. Drew, it was a pleasure to work with you! I truly believe that without you we wouldn't have achieved the success with the radial trough project. Thank you for never saying no and for being available anytime I texted you.

Fernando, we only got a year to spent together in our lab. But even in this short period of time we managed to become good friends! I thoroughly enjoyed our long chats. Thank you for hearing me out and sharing your knowledge with me.

To my parents Mumma and Pappa, my siblings Prajakta (Tai) and Saurabh, I thank you from the bottom of my heart. Mumma, your prayers were the reason for my strength and motivation throughout this process. Pappa, your unbeatable optimism gave me the hope that I needed in my most critical times. Tai, your firm belief, and appreciation was the cause that kept me going. Saurabh, you always boosted me by paying heed to my problems and giving the most unbiased opinions. Thank you all for standing by me in the lowest phases and never letting me doubt myself. It was not easy to pursue my degree in a foreign country that is thousands of miles away from home. However, it was your relentless emotional support, care and encouragement that has helped me to reach this point. Achieving this milestone has been our collective dream and each one of you has contributed significantly towards it.

Last, but not the least, my best friend and soon to be my husband, Mihir. No words are enough to describe the gratitude that I feel for you. You gave me the confidence when I lost hope and you believed in me more than myself. You had no idea of what my research was about, but

you made sincere efforts to solve the questions that I bombarded on you under frustration. You were truly the calmness in this chaotic journey! Thank you for showing how proud you are of me. Thank you for everything! I wouldn't have been able to finish this without your unconditional love and support.

This thesis is dedicated to

My maternal and paternal grandparents who always thought ahead of their times and believed in education. You all are my inspiration!

My mother, Pradnya Kale, and my father, Karbhari Kale, for making me ambitious and capable.

CHAPTER 1

INTRODUCTION AND BACKGROUND

“Success is not measured in achievement of goals, but in the stress and strain of meeting those goals”

-Spencer W. Kimball

1.1 Why Rheology?

The formal genesis of rheology as a discipline is dated back in 1929, however its origin has roots in antiquity [1, 2]. The term rheology is inspired by a quote from a Greek philosopher that means “everything flows” [3] and in fact, it is true, everything does flow. For instance, even rigid structures like mantle rocks tend to flow under conditions like huge deformation timescales, temperature, pressure, etc. [4]. However, the flow behavior is different for different materials. What rheology does is that it describes the flow behavior of any material by understanding the relationship between the applied stress or strain under varied conditions. This rheological knowledge affects our day-to-day life. It can help us to understand simple everyday phenomena like why pouring ketchup from a bottle requires a slight push, or why the wall paints do not drip after brushing. The answers lie in the rheology of those materials i.e., ketchup won't flow without a minimum 'stress' because it has a certain yield stress [5] and paints do not drip after brushing because the paint viscosity increases after the brush strokes are slowed (or strain is reduced) [6]. This understanding of material behavior can also be used to manipulate the material properties according to consumer needs. Products like foaming shampoos or shower gels [7], spreadable butter [8], biomimetic tissue [9], etc. are a few examples from different sectors of human utilities whose rheological properties are controlled for a specific function. Overall,

rheology can help in tuning the factors like product design, formulation, stability, and processing ultimately governing its quality and performance.

1.2 Methods in Rheology

Many materials of interest like food, cosmetics, polymers, or biological samples are viscoelastic in nature which means their behavior is somewhere in between viscous fluids and elastic solids. Such materials are considered as complex materials. Over the years, the analysis methods, and techniques to characterize viscoelastic properties have grown and they are typically developed according to the applications. For example, understanding the role of elongational flow in the processing of food [10] and polymers [11, 12] brought in the development of extensional rheology. In case of bulk rheology, specialized geometries are developed to encompass events like wall-slip that occur in materials like mayonnaise, vane geometries for gel-like materials or geometries that cover specific range of viscoelastic moduli [13]. Mechanical response of biological systems like cells or tissues is important in biotechnology [14, 15]. The viscoelastic properties in such systems vary at micron or sub-micron length scales and thus rheological characterization must be carried out locally. This is achieved with a relatively new approach called microrheology. High interfacial materials like foams and emulsions, bio membranes, etc. demand the use of interfacial rheological methods to probe viscoelastic properties at fluid-fluid interfaces [16]. Further, it won't be an exaggeration to say that for almost every material the intrinsic rheological behavior is tied to the underlying macro or micro or molecular structure. Examples include, but are not limited to, molecular structure of polymeric materials [17, 18], colloidal glass structures [19, 20], molecular or microstructure of surfactants at fluid-fluid interfaces [21, 22]. To establish the structure-property relationships for such materials rheological investigations are either supported with ex-situ or in-situ structural

analysis. For in-situ analysis, rheometers are combined with microscopy or specific tools like small-angle-neutron scattering [21, 23]. Sometimes methods are also classified based on types of deformations. For instance, in passive microrheology the random local deformation is caused by the inherent thermal or Brownian motion of colloidal scale particles that are used as probes for local strains. In case of interfacial rheology, tools are typically defined by the applied deformation type, e.g., interfacial shear rheometry (constant interfacial size) or dilatational rheometry (constant interfacial shape) techniques. Overall, there is a vast range of rheological techniques that are created for different applications and purposes. As the science and technology grows, the rheological techniques are expected to improvise to accommodate the new challenges of that come along. These challenges can be in the form of expansion of operating range of viscoelastic moduli, investigating specialized innovative materials like polymers composites or printable biomaterials, or lack of ability of a method to visualize underlying structures that influences viscoelastic properties.

This thesis covers a discussion on microrheology and interfacial rheological methods and highlight certain challenges with their conventional methods. It introduces two novel rheological techniques in these domains that are combined with microscopy with an aim to address the challenges in the traditional methods and characterize viscoelastic properties of complex materials.

1.3 Thesis Organization and Major Contributions

This thesis is divided into six chapters. Chapter 1 includes the introduction and background of the field and comprises the thesis statement. It also gives a brief overview of conventional techniques available in microrheology and interfacial rheology. Chapter 2

introduces a new method in microrheology area while Chapter 3 describes a new interfacial rheology tool for true dilatational deformations with in-situ interfacial visualization. Chapter 3 is focused on constant rate of change of area deformations. Chapter 4 employs the same technique from Chapter 3 but is confined to oscillatory area deformations to extract dilatational viscoelastic moduli. Chapter 5 talks about the possible future work using the newly developed devices. Chapter 6 is the summary of conclusions of the thesis work.

Chapter 2 describes an active microrheology technique that was developed to overcome limitations of the widely used passive particle tracking microrheology (PTM) method. Passive PTM microrheology employs the inherent Brownian motion of colloidal scale particles that are embedded in the sample and tracks their motion using video microscopy to relate it to the material's local properties like the viscosity. In relatively stiffer materials, the particle displacement due to Brownian motion is hindered owing the resistance from the stiffer material. Displacements are therefore not distinguishable under microscope and the technique reaches its upper limit to estimate the material properties. We developed single coil electromagnetic tweezers that induces artificial thermal noise or in other words artificial Brownian motion as an external force. This fluctuates the colloidal superparamagnetic particle with energy on the order of 10 kT and enables the displacements to be distinguishable under microscope. The advantage of this method is that the probing of the particle in a random Brownian fashion allows us to use the standard hydrodynamic models like that used in passive PTM. This is unlike other active methods that typically uses oscillatory forces and require prior knowledge of strain field before evaluating the viscoelastic properties.

Chapter 3 illustrates the development of an interfacial rheology tool names as radial Langmuir trough that can perform true dilatational deformation of fluid-fluid interfaces with

simultaneous interfacial visualization using microscopy. It emphasizes the need for methods that can isolate the contribution of different deformation type like shear versus dilatational.

Experiments techniques that can execute pure dilatational deformation along with in-situ interfacial visualization is rare and therefore this work is an important contribution to understanding the structure-property relationship of complex fluid-fluid interfaces. We show the application of this device in two systems: PtBMA at air-water interface which is a polymeric film and DPPC at air-water interface which is a model lung surfactant. For PtBMA at air-water interface we were able to characterize the dilatational compression modulus or the Young's modulus by investigating the interfacial film structure. For DPPC we able to relate the surface pressure measurements with the microscopic structure.

Chapter 4 focuses on the oscillatory dilatational area deformations of model lung surfactant i.e., DPPC at air-water interface. Here, we characterize the dilatational viscoelastic moduli of DPPC air-water interface at different strain percentages. Further, we were able to correlate the microstructure to the viscoelastic properties. Major contribution of this work is the ability to perform oscillatory area deformation with simultaneous visualization. Overall, the development of the radial Langmuir trough can be extended to study constitutive equations of complex fluid-fluid interfaces.

1.4 Background

1.4.1 Rheology Basics

Rheology is a multidisciplinary field which studies the flow and deformation of matter under applied stresses [3, 24-28]. Polymers, emulsions, food products, cosmetics, gels, paints and many other ubiquitous materials are of rheological interest. The rheological properties of these materials serve as vital operating parameters in industrial processing and fabrication, thus

affecting the product quality [29, 30]. The study aims at understanding the relation between structure and flow properties of any such material under the influence of stress. Fundamental equations are developed from rheological studies that relates the deformations and stresses (or forces) [25, 31]. These equations known as constitutive equations can then be used to predict the material's response under various deformation conditions.

A rheological quantity is a result of material's mechanical response when probed under an applied stress (τ) or strain (γ). If the material is probed at the macroscopic scale, the resultant measurements quantify bulk properties and hence termed as bulk rheology. The magnitude, time and spatial orientation of deformations also affect the measured rheological quantity [3] especially in case of viscoelastic materials. For example, in complex viscoelastic samples, the time scale of deformation determines the dominance of solid or liquid like behavior. In many cases, the viscoelastic material has an intermediate behavior. When probed, a true elastic solid stores energy and behaves like a spring. The constitutive relation for elastic solids is given by the Hooke's law of elasticity stated as $\tau = G\gamma$. Here, G is the rheological quantity known as the elastic modulus and can be calculated by simple re-arrangement of the Hooke's law equation. On the other hand, for a purely viscous fluid the material dissipates energy and the rheological quantity associated with it is called viscosity η . It is defined by another well-known constitutive equation, Newton's law of viscosity given as $\tau = \eta\dot{\gamma}$, where $\dot{\gamma}$ is the strain rate. Further, as one can observe, the aforementioned equations describe only the two limiting domains of materials independently. Now, to characterize prevalent viscoelastic materials, the experiments must effectively probe both the viscous and elastic nature of the sample. Traditionally, this is reliably done by applying a small amplitude oscillatory shear strain (SAOS) measurement. Here, the small amplitude being such that it does not disturb the sample's equilibrium and hence only

probes the linear viscoelastic (LVE) properties. This implies that, any higher amplitude will introduce non-linear probing in the sample and thus must be modeled differently. The SAOS is applied as a sinusoidal input given by equation 1.1:

$$\gamma(t) = \gamma_0 \sin(\omega t) \quad (1.1)$$

Where, γ_0 is the amplitude, ω is the frequency, and t is the duration of the input oscillatory strain. Now, because the amplitude is small and the material is not deformed out of equilibrium, the stress ($\tau(t)$) developed is linearly proportional to strain [25, 26]. The time-dependent stress obtained is defined by equation 1.2:

$$\tau(t) = \gamma_0 [G'(\omega) \sin(\omega t) + G''(\omega) \cos(\omega t)] \quad (1.2)$$

In this equation, $G'(\omega)$ is the storage or elastic modulus in phase with the applied sinusoidal strain and $G''(\omega)$ is loss or viscous modulus in phase with the strain rate. Equations 1.3 and 1.4 define $G'(\omega)$ and $G''(\omega)$ respectively, with δ as the phase difference between applied strain and corresponding stress response.

$$G'(\omega) = \frac{\tau_0}{\gamma_0} \cos(\delta) \quad (1.3)$$

$$G''(\omega) = \frac{\tau_0}{\gamma_0} \sin(\delta) \quad (1.4)$$

The complex shear modulus is then defined as:

$$G^*(\omega) = G'(\omega) + i G''(\omega) \quad (1.5)$$

Equation 1.5 captures the complex modulus of not only viscoelastic samples but of any material in general. In case of viscous Newtonian fluid, $G'(\omega) = 0$ and $\eta^*(\omega) = G''(\omega)/i\omega$ where,

$\eta^*(\omega)$ is the complex viscosity. Similarly, for a Hookean elastic solid $G''(\omega) = 0$ and $G'(\omega) = G$. The description of the above two moduli can be understood by drawing an analogy with the two laws stated earlier and is thus evident from equation 1.2 as well. Individually these moduli are non-zero for a viscoelastic material and are function of frequency.

Despite the widespread application of bulk rheology, it faces significant practical limitations. Bulk rheometers apply considerably higher stresses and strains on larger areas and thus captures only the averaged or bulk mechanical response of the sample [26-28, 32, 33]. The length scales at which bulk rheology operates is also very large (usually millimeter or more). Therefore, it evidently neglects spatial heterogeneity and changes in rheological properties at smaller length scales, thus failing to characterize the local microenvironment. For instance, cellular processes like organelle and biomolecule transport, cell matrix, complex polymer networks and microgels display rheological properties at small length scales (micrometer) which bulk rheology cannot capture. Further high magnitudes of stresses and deformations are physically detrimental to many fragile soft matters like biological samples, hydrogels and colloidal systems [27]. Requirement of large sample volumes, limited range of probing frequency (up to tens of Hz) and small range of measurable moduli, are other major disadvantages associated with bulk rheometry. These shortcomings of bulk rheology are countered by a relatively new technique known as microrheology. Various sub-techniques in microrheology have greatly evolved during the past few decades [27, 34] extending the scope bulk rheology and answering fundamental question like how does the rheological property change over micro-length scales [34-36]. Brief description of microrheology is provided in next section.

1.4.2 Microrheology

Microrheology is a promising field that has been developed to measure rheological properties of mainly viscoelastic samples at micron and sub-micron length scales [37, 38]. As mentioned in the last section, there are several materials like food emulsions, cellular environment, complex gel matrix and polymer networks that exhibit variations in rheological properties at smaller length scales. Microrheological tools help characterize these samples and in most instances bulk and microrheology prove to be complementary [39]. The basic principle of microrheology is to use colloidal scale particles embedded in the material of interest and track their motion to back-out the local mechanical response. The particle displacements depend on the rheological nature of the specimen enabling to quantify the rheological properties. Further, the small size of the colloidal beads allows to probe ‘micro’-rheological properties. It offers several advantages over the conventional bulk rheology techniques. Requirement of small sample volumes typically in few micro-liters (vital for precious biological samples), extended range of probing frequencies (up to few MHz) due to better temporal resolution when Diffusive Wave Spectroscopy (DWS) is used [26, 33, 37, 40], ability to perturb microenvironment and hence deduce local rheology, ability to map spatial heterogeneity, significantly short data acquisition time, easy and non-destructive experimentation and many others are the benefits of microrheology [27, 33, 35, 37, 40].

Depending on whether the motion of the beads is driven by inherent thermal energy (kT) or external stimuli, there are two main modes of operation in the field of microrheology. First is passive microrheology, in which the probe particles display measurable Brownian motion (random fluctuations) owing to significant internal thermal energy. Second is active microrheology, where particles are set into motion externally with the aid of magnetic or optical

forces. The random Brownian fluctuations are hindered in comparatively rigid materials and hence active techniques are more suitable in these cases [37].

1.4.2.1 Principles of Passive Microrheology

Passive microrheology relies purely on the inherent thermal fluctuations of the colloidal particles, also called as the Brownian motion. This Brownian motion originates from constant bombardment from surrounding fluid molecules in the form of random thermal forces. As a result, the particle experiences a drag force slowing its motion. Both the thermally fluctuating force and the dissipative drag force are generated from the same collisions and thus maintain equilibrium. This phenomenon is therefore a manifestation of the famous *fluctuation-dissipation theorem* [41]. Brownian motion is truly random in nature and hence the mean displacement of particles over statistically significant time is zero. However, the mean squared displacement (MSD) of each particle is non-zero and serves as the measurable quantity in the microrheology experiments. The resistance from the medium is reflected in the magnitude and time-dependency of MSD, thus quantifying the material's rheological property. The thermal energy kT where k is the Boltzmann's constant and T is the absolute temperature of the fluid, is small such that it perturbs only the linear viscoelastic properties of the medium [27, 37]. Due to this, passive microrheology is suitable for relatively softer materials with weak complex moduli [40].

The Generalized Stokes Einstein Relation (GSER) is the principle equation governing passive microrheology [27, 40] for viscoelastic sample. It relates the MSD of the randomly fluctuating particle with the material's rheological property. For the derivation of GSER we will begin with the Langevin equation (equation 1.8) for a viscous medium, which describes the random motion of the particle in accordance to Newton's second law of motion. A spherical

particle of mass m and radius of a , suspended in a medium of viscosity η with its velocity $v(t)$, will have acceleration due to net force acting on it and is given by:

$$m \frac{dv(t)}{dt} = -fv(t) + F(t) \quad (1.8)$$

Equation 1.8 is the relates the stochastic thermal force $F(t)$ and the frictional force $fv(t)$, where f is the Stokes friction coefficient given by $f = 6\pi\eta a$ in case of viscous medium. $F(t)$ has a characteristic Gaussian white noise spectrum, whose power spectral density is independent of frequency. Equation 1.8 satisfies FDT and for an equilibrium system it ensures that passive and active methods give same results [27]. In equation 1.9, the equipartition and FDT demonstrates MSD ($\langle \Delta r^2(t) \rangle$) as a function of time and diffusivity (D) of the particle.

$$\langle \Delta r^2(t) \rangle = \frac{2kT}{f} t = 2dDt \quad (1.9)$$

Where $r(t)$ is the particle position, and d is the number of dimensions for which the displacements are tracked. The symbol $\langle \dots \rangle$ in the above equation indicates that MSD is an ensemble time average for each particle or an ensemble average over several particle trajectories (path traveled by a particle). Being an average quantity, the statistics can be improved by performing the experiment for long time or by tracking large number of particles for short time. Experimental determination of MSD will be discussed in the in section 1.2.2 of this chapter. The famous Stokes-Einstein relation (SER) defines diffusivity for a viscous medium in terms of the thermal energy as

$$D = \frac{kT}{f} = \frac{kT}{6\pi a \eta} \quad (1.10)$$

Combining the above equations 1.9 and 1.10 for a viscous medium, we can define the MSD as

$$\langle \Delta r^2(t) \rangle = \frac{dkTt}{3\pi a\eta} \quad (1.11)$$

Further for a purely elastic medium with elastic modulus G , equation 1.11 can be modified as

$$\langle \Delta r^2(t) \rangle = \frac{dkT}{3\pi aG} \quad (1.12)$$

In case of a viscoelastic medium, the friction coefficient will be a function of time. Using one-sided Fourier Transform the time-dependent friction coefficient can be expressed in frequency domain. This is done because, expressing the complex shear modulus in frequency domain is desirable as it can then be compared with bulk rheology [40]. According to Corresponding Principle [40], the frequency domain friction coefficient after a Fourier Transform is given as

$$\tilde{f}(\omega) = 6\pi a\eta^*(\omega) \quad (1.13)$$

From the definition of complex viscosity mentioned in section 1.1, we have

$$\eta^*(\omega) = \frac{G^*(\omega)}{i\omega} \quad (1.14)$$

Using the above definitions, one can now easily understand the Generalized Stokes Einstein Relation (GSER) developed by Mason and Weitz in 1995 [42]

$$G^*(\omega) = \frac{dkT}{3\pi a(i\omega)\langle \Delta \tilde{r}^2(t) \rangle} \quad (1.15)$$

Where, $\langle \Delta \tilde{r}^2(t) \rangle$ is the unilateral (one sided) Fourier Transform of the MSD. Similar results can be obtained if Laplace transforms are used. The use of GSER depends on two main assumptions:

1) The continuum assumption that satisfies Stokes Einstein Relation in which particle must experience continuous microenvironment and 2) a state of thermal equilibrium which ensures linear viscoelastic regime (LVE). Equation 1.15 gives the complex shear modulus for a

viscoelastic material. Fourier transform assumes an infinite time series which is not practically possible. Estimating Fourier Transforms of MSD term for discrete times introduces significant truncation errors that ultimately affects the measured complex modulus [28, 40]. To account for such errors, Mason [43] suggested a power-law approximation to evaluate the MSD at each sample time t_0 as

$$\langle \Delta r^2(t) \rangle \approx \langle \Delta r^2(t_0) \rangle (t/t_0)^{\alpha(t_0)} \quad (1.16)$$

Here, $\alpha(t_0)$ is the logarithmic slope of MSD which is calculated at t_0 and is defined as

$$\alpha(t_0) = \left. \frac{d(\ln \langle \Delta r^2(t) \rangle)}{d(\ln t)} \right|_{t=t_0} \quad (1.17)$$

The MSD can also be expressed in terms of lag time (τ), which can be thought of an average of all the time differences (Δt). All the previously mentioned time-dependent equations can be expressed with τ by simply replacing t with τ . For instance, MSD and logarithmic slope can be written in terms of τ as the following equations

$$\langle \Delta r^2(\tau) \rangle = 2dD\tau = \langle [r(t + \tau) - r(t)]^2 \rangle \quad (1.18)$$

$$\alpha(\tau_0) = \left. \frac{d(\ln \langle \Delta r^2(\tau) \rangle)}{d(\ln \tau)} \right|_{\tau=\tau_0} \quad (1.19)$$

The value of the above logarithmic slope ranges from 0 to 1 based on the type of medium. MSD is linearly proportional to time in case of viscous fluids (diffusive motion) and is independent of time for elastic samples. As viscoelastic medium has characteristics of both mediums, the slope is in between 0 and 1 and the motion is sub-diffusive. When the motion of the probe is directed, usually due to external forces, the slope of MSD is greater than 1 and the motion is termed as

super-diffusive. The value of the slope is used to calculate the storage ($G'(\omega)$) and loss ($G''(\omega)$) moduli as follows [40]

$$G'(\omega) = |G^*(\omega)|\cos(\delta) = |G^*(\omega)| \cos(\pi\alpha(\omega)/2) \quad (1.20)$$

$$G''(\omega) = |G^*(\omega)|\sin(\delta) = |G^*(\omega)| \sin(\pi\alpha(\omega)/2) \quad (1.21)$$

With δ being the phase difference as described previously (section 1.1) and from above equations it is defined as $\delta(\omega) = \pi\alpha(\omega)/2$. Since the slope $\alpha(\omega)$ may have values from 0 and 1, δ varies from 0 and $\pi/2$. Evidently it is zero for elastic medium and $\pi/2$ for viscous medium. The MSD is directly related to another rheological property i.e., the averaged creep compliance. It can be understood as the total strain developed in the material due to the average thermal stress experienced by the particle[40]. The following equation defines the creep compliance in terms of MSD

$$J(t) = \frac{3\pi a}{dkT} \langle \Delta r^2(t) \rangle \quad J(t) \propto \frac{\langle \Delta r^2(t) \rangle}{kT/a} \leftrightarrow \frac{\text{Strain accumulated}}{\text{Average Stress}} \quad (1.22)$$

1.4.2.2 Passive Microrheology Techniques

There are few different methods to experimentally calculate the MSD of the embedded particles. Trajectories of the diffusing particles can be tracked directly using video-based microscopy (particle tracking microrheology) or scattered light intensities [27].

Dynamic light scattering (DLS) is a technique that uses a light beam to illuminate the sample containing the probe particles and measures the scattered light intensity developed due to fluctuating particles. In a typical setup, the light beam (laser) hits the particles and as the particles undergo Brownian motion and diffuse through the sample, the scattered light intensity changes as a function of time [36]. This scattered light is measured using a laser beam detector

and it generates an autocorrelation function ($g(t)$) using Siegert relation [28, 40] which depends on the scattering angle. This function can be expressed in terms of MSD in which $g(t)$ is calculated using the fluctuations in the detector and the only unknown is the MSD. Rheological properties are then evaluated from the measured MSD. This method is suitable for dilute samples where multiple scattering is avoided to accurately measure the scattering angles.

Another light scattering technique is Diffusive Wave Spectroscopy (DWS) which has similar setup as DLS except that of the detector position. Unlike DLS, it uses high probe concentration and relies on multiple scattering of photons resulting from these probes [35]. MSD is calculated from correlations of the transmitted light (or photons) which is detected by the detector. Even a small change in the particle position causes a huge change in the diffusion path of the photons as the effect gets multiplied. Thus, it is more sensitive in comparison to DLS and is suitable for opaque samples. The temporal resolution for a typical DWS setup is $\sim 1\mu\text{s}$ [35, 40] allowing to have better resolution for measuring MSD. Both DLS and DWS are based on averaged particle trajectories and hence are not appropriate in case of heterogeneous samples. Due to higher particle concentration required for DWS experiments it may affect the material rheology itself [39].

Video based particle tracking or particle tracking microrheology (PTM) is one of the simplest and extensively adopted method for calculating the MSD of the particles [27]. It combines traditional microscopy techniques with high-speed CMOS or CCD cameras. The particle motion is directly recorded as a video using the camera and trajectories for each particle are measured. The particle position is measured to sub-pixel accuracy using a center of mass estimation or intensity-weighted calculations. The recorded video is analyzed frame by frame and particle tracking algorithm is applied to quantify the MSD. Open-source algorithms in

MATLAB, IDL and LabVIEW are available which allows the widespread use of this technique. In Chapter 2, we focus on the passive PTM method and its limitation. We developed an active microrheology tool to overcome this limitation and is discussed in detail in Chapter 2. Before that, we give a brief overview of active microrheology technique.

1.4.2.3 Active Microrheology Techniques

In this method of microrheology, the particle motion is imposed using external forces which are notably higher in magnitude than the Brownian force. These extra forces (apart from intrinsic thermal fluctuations) allow to probe relatively rigid specimens which are otherwise inaccessible to passive microrheology. Active method has found its traces older than passive method and can be dated back to examples from the study of Heilbronn [44] and Seifriz [45], where they used active motion of iron filings and nickel particles (respectively) to measure mechanical properties of biological fluids like slime molds and sand dollar eggs [40]. Magnetic, optical, and atomic forces are typically used to probe microrheology of the material. Like bulk rheological probing described previously, active methods usually perform oscillatory or creep deformations on samples with particles as probing agents.

Optical tweezers or laser tweezers use the optical force generated by a strong laser beam to trap and manipulate the probe particles [27]. Dielectric particles under the influence of laser get polarized and an optical dipole is created. By moving the trapping laser focus, localized optical field gradients are generated by which particle position can be controlled [28]. The particle displacement is captured by quadrant photodiode from which MSD data is calculated. Limited forces up to piconewton range can be produced [26, 28] using optical fields. The advantage of optical tweezers is that the particle position is easily manipulated with very localized force generation. However, the laser beam used are usually very strong which causes

considerable local heating of the sample [27, 28, 46]. Furthermore, phototoxicity or photodamage can be an important issue in case of biological samples [26].

Magnetic tweezers or magnetic rheometry employ magnetic field generated by either using strong permanent magnets or electromagnetic coils to move magnetic particles. Mainly two types of magnetic particles are used, ferromagnetic or superparamagnetic particles. Ferromagnetic beads have their own dipole moment even in absence of external field, on other hand superparamagnetic beads acquire dipole moment only in the presence of external magnetic field. Magnetic fields produced by permanent magnets have less scope of manipulation in terms of field strengths. In case of electromagnetic coils, the amount of current following through coils and number of turns in a coil determine the strength of the magnetic field generated, thus providing a better control. Permanent magnets can produce large forces in nanonewton range, while with electromagnetic setup piconewton forces are more common [27]. Particles can rotate in constant magnetic fields thus allowing torque measurements. With field gradients, particle displacement motion is possible. Apart from rotational method (usually performed with permanent magnets), creep and oscillatory methods (usually performed with electromagnetic coils) are frequently used to study microrheological properties. In all cases, the particle position and displacement can be measured with video particle tracking. As compared to optical fields, magnetic field causes negligible sample heating [27, 46] and is thus more acceptable to use with biological samples. Further magnetic fields are known to have impact only on the magnetic particles and very weakly affects the material being probed (like biological samples and polymers) [27].

Atomic Force Microscopy (AFM) is a probe-free active microrheological technique. It addresses two physical aspects, one being the topographical structure and other being the

mechanical response. The harmonic motion of the cantilever tip is used as the external force to indent the material and its response is measured to back-out the material's rheological properties. A laser beam focused on the cantilever deflects with its motion and enables to measure the response. AFM has been very useful in probing the dynamics of cellular processes like cell division and migration [27]. A major disadvantage of AFM microrheology is that it is an invasive method which is not favorable for many specimens.

With brief overview of available microrheological techniques covered here, one can understand that each technique is suitable for a particular range of moduli and applications and has its own pros and cons. For instance, in a stiffer material with lower compliance where particle displacement is restricted, DWS method is more favorable as it has the capability to measure such tiny displacements. On the other hand, active methods in such cases are limiting due to larger force requirement to displace the probe which is already competing with the material's resistance. Magnetic and optical tweezers have been extensively used for micromanipulation of DNA, living cells, and single biomolecules [47-53], which cannot be performed with simple passive approach. In addition, combining passive and active techniques with different analysis methods broadens the scope of rheological measurement and often prove to be complementary.

In this work, we plan to focus on the restrictions of passive PTM and aim to counter it with active approach while maintaining the essence and ease of passive method. Passive PTM is most practical approach as it is easy to implement experimentally and furthermore, it utilizes the straightforward GSER equation to measure rheological properties. It models the inherent thermal fluctuations of the material without harming the structure and equilibrium of the system. However, along with these advantages, passive particle tracking faces a major pitfall and that is

the considerably low range of measurable moduli. In other words, passive method is suitable with highly compliant softer specimens where the Brownian motion of the probe particle is significant. The actual quantitative operating limit depends on the particle size and the spatial resolution of the microscope which is typically 10nm [40]. With this resolution and 1 μ m particle, the upper maximum measurable modulus translates to $\sim 10^0$ Pa [40]. To have measurable MSD within a microscope's resolution limit, one way is to increase the magnitude of MSD. Evidently, this can be achieved by using external active forces. Conventional active approaches similar to bulk counterparts like oscillatory [54, 55] or constant creep measurements (different from equation 1.22) [54, 56] can also be restraining. This is because they require prior idea of the strain field before measurements. Therefore, we have chosen a unique approach for the type of external force and i.e., to mimic thermal forces such that the particle still fluctuates randomly and produces a Brownian-like motion. We refer this external random force as artificial thermal noise. The corresponding random energy supposedly exceeds the thermal energy kT . Within the linear regime, these active random forces will apparently mimic the inherent thermal forces simply allowing us to use classic hydrodynamic model which is GSER for evaluating the complex viscoelastic modulus. This led to our first thesis statement.

1.4.3 Thesis Statement I

Artificial thermal noise can induce random motion to the probe particle and the resulting random displacements can be used in the classic hydrodynamic models based on the passive Brownian motion.

In this thesis, we make use of electromagnetic tweezers as a source of active or external forces. For convenience, we implement the idea of artificial thermal noise in 1d. In an electromagnet, the current flowing to the coil produces magnetic field. Therefore, a random

current signal will give desired random magnetic field. The fluctuating field can be used to manipulate the position of a superparamagnetic particle in a random fashion. To achieve this, we first worked on generating the artificial thermal force which is a white noise signal. Ideally, the mean value of the signal must be zero so that it maintains a mean displacement of zero for the particle motion. Such a current signal will have positive and negative magnitudes. A straightforward way to get 1d fluctuations of the particle is to use a two-coil system that acts in tandem, and the total white noise signal is divided across both the coils. This way, half the signal arrives from the first coil and the second half from the other coil. The experimental details of how the signal is generated and the specifics of the coil geometry are mentioned in Chapter 2. Here, we only discuss the one preliminary result with a viscoelastic sample.

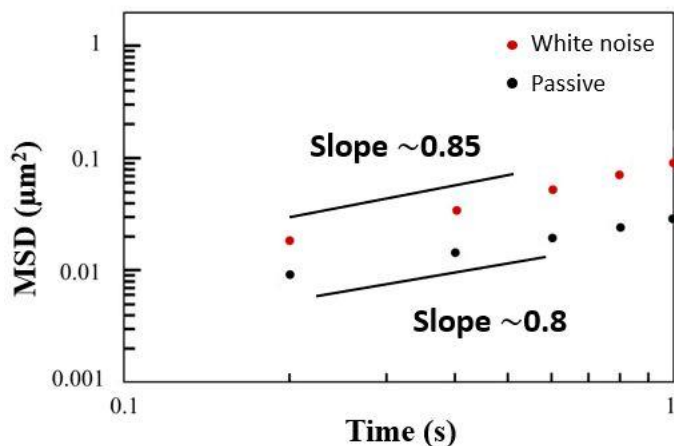


Figure. 1.1 Preliminary MSD versus time data set of 0.45 wt.% of calcium alginate gel. The black curve is the passive PTM measurement, and the red curve is MSD data obtained after applying white noise signal.

Fig. 1.1 shows MSD versus time data of viscoelastic alginate gel sample. Alginate gels are very commonly used in hydrogels and scaffolds [57-59] and can easily form homogenous viscoelastic gels. Thus, we use this as our viscoelastic model system in our preliminary

experiments. Since it is a viscoelastic material, we expect the MSD slope to be <1 . So, we performed first performed a passive PTM measurement on this sample (black curve). As seen in the figure, the slope is approximately 0.8 confirming the viscoelastic nature. An additional external artificial noise should ideally maintain the slope value but increase the magnitude of MSD. We clearly see that the MSD magnitude increases but the slope remains almost the same. This shows that the implementation of artificial thermal noise is feasible with a two-coil system. This alginate sample was made with relatively low modulus complex viscoelasticity (G^* is approximately on the order of 0.05 Pa) and this was well within the passive PTM operating range. This is because, in this preliminary case, we didn't have an idea of the magnitude of forces we could generate with given set of coils and at given distance away from target particles. For a given set of coils, the magnitude of force can be increased by moving the coils closer. In our initial experiments, we learnt that as we attempt to test relatively high moduli viscoelastic materials that are on the order of 1 Pa or higher, we needed larger forces. The easiest route was to move the coils physically closer. However, at closer distances between the two coils, there is significant coil-coil interference. This directly affects the magnetic field generated by both coils. Thus, at smaller distances, the coils did not function as expected. Therefore, with a two-coil system we were limited to measure low moduli viscoelastic samples. This clearly defeats the motivation of this approach. Thus, we chose a different approach to continue the idea. We implemented artificial thermal noise with a single coil system. The entire detail for the methodology is provided in Chapter 2. As a result of this single coil approach, we eliminated the limitation of coil-coil interference. With single coil system we able to probe a Newtonian fluid with viscosity that is one order of magnitude higher than the maximum upper limit of passive PTM.

1.4.4 Interfacial Rheology

Interfacial rheology is class of rheological technique that investigates the rheological properties of complex fluid-fluid interfaces. Fluid-fluid interfaces are commonly observed many natural and synthetic systems, like biological membranes, foams and emulsions found in various application like food, cosmetics, etc. Interfaces are formed when two immiscible phases come in contact. Fluid-fluid interfaces are either liquid-liquid or liquid-gas interfaces. For pure or clean interface of the two phases, there is net cohesive force that acts towards the bulk of the material, and this gives rise to surface tension. For example, at air-water interface, the bulk of air or water have attractive forces in all directions, but near the interface there unbalanced cohesive force that acts towards the bulk side. When surface-active agents at present at such clean interfaces, extra and deviatoric forces are present apart from the surface tension force [60]. The overall interfacial stress (σ^s) can be written as a combination of the stress from the surface tension (σ^e) that is function of surface concentration of surface-active agents and the extra surface stress that arises due to the rheological and deformation reasons [60-62]. The equation for the total stress at interfaces with surface-active materials is given below:

$$\sigma^s = \sigma(\Gamma)I + \sigma^e \quad (1.23)$$

Here, σ is the surface tension of the interface in presence of surface-active material, and I is the surface unit stress tensor. When the interfacial area is deformed the concentration of the surface-active material changes that gives rise to compressibility (Gibbs elasticity) and/or there are Marangoni effects to gradient in concentration. Additionally, the lateral interactions of the interfacial material tend to resist the change in area deformations. This even more true when the material is highly structured and is because of the extra rheological stresses [61, 62]. Like bulk rheology these extra stresses are evaluated based on the deformations type and the corresponding

constitutive equations that are modeled for interfaces. Thus, the relationship between the interfacial deformation and the resulting extra interfacial stresses defines the interfacial material functions.

There can be different modes of interfacial deformations elongation, shear, or dilatational deformations. Our discussion is limited to shear and dilatational deformations. When the interfacial area is deformed such that the size or the total interfacial area is retained but the shape is deformed then it's termed as shear deformation [16, 63]. On the other hand, when the interfacial area is deformed such that the shape of the area is maintained but its size is altered then it is called as dilatational deformation [16, 63]. The thesis work is prioritized in dilatational deformations of interfaces.

1.4.4.1 Interfacial Rheology Techniques

Interfacial rheological methods to induce true shear deformations are well developed in the literature. There are various robust techniques that are conventionally and commercially available. One of the simplest rheometers that was developed was magnetic rod interfacial shear rheometer [64, 65]. Here, a magnetic rod is placed at the fluid-fluid interface and is oscillated using an oscillatory force from the magnetic field generated by Helmholtz coil. The rod motion is detected using a microscope attached to the device. The phase difference of the oscillatory strain i.e., the displacement of the magnetic rod and the applied force is used to estimate the viscoelastic moduli. A similar concept of using magnetic field to induce shear strains was employed with a disc shape magnetic micro button [66, 67]. The advantage in this method is that the probe dimension is small and therefore a more localized and sensitive response can be obtained. Both magnetic rod and magnetic micro button methods can probe relatively low moduli material [60]. For relatively stiffer interfaces, method like bicone rheometer [68] or

double wall ring (DWR) rheometers [69] are used. In both methods the geometries i.e., the bicone and DWR are attached to the motor of a sensitive traditional rheometer thus extending the operating range. However, the geometry for DWR is much thinner providing a better inherent sensitivity than bicone [60].

Techniques that induce true dilatational deformations include two main categories. Curved interface methods that include drop/bubble-based methods, or capillary tensiometers and planar methods [60] that include Langmuir trough methods. In the curved interfaces of drop/bubble-based methods the interfacial area is deformed by changing the volume. The surface pressure is estimated via shape analysis tools that use the Young-Laplace equation. In planar interfaces, the interfacial area is deformed by moving some type of barrier and the interfacial tension is measured force exerted on a Wilhelmy probe that is attached to a Wilhelmy balance. Surface pressure (π) is estimated by the difference in the surface tension of clean interface (σ_o) and that of interface with surface-active material ($\sigma(\Gamma)$). It is given by the formula, $\pi = \sigma_o - \sigma(\Gamma)$. Curved interface methods have an advantage that the frequency of probing the material is high, especially in the capillary tensiometers. But a main drawback with curved interfaces is that at high interfacial coverage with highly structured materials, the interface tends to buckle and the shape analysis is not accurate and it is not trivial to perform corrections [60]. This gives error with the surface pressure analysis. In case of commercially available planar Langmuir trough methods, mixed deformations field are observed at high coverages and compression of the interface [60, 61]. This means at compression ratio, both shear and dilatational deformations are included. Thus, true dilatational deformations are not obtained. This is not favorable because there are instances where contribution of dilatational deformations is crucial [61]. Another aspect of interfacial rheological investigation is structure visualization. It is well recognized from the

literature that the interfacial rheological properties are correlated to the underlying structure [16, 70]. In many cases, the visualization is performed ex-situ. However, to truly analyze the dynamic properties, it is important to look at the in-situ dilatational visualization of interfaces. With curved interfaces it is very difficult to include in-situ visualization techniques. Further, attempts to include visualization techniques in trough-based methods can be costly and tedious. The details of the above limitations and the past research attempts to overcome them have been discussed in Chapter 3.

These above limitations suggest that there is a need for developing new and improved interfacial rheological tools that can perform true dilatational deformations and interfacial visualization. For this we have proposed a compact device named miniaturized radial Langmuir trough. It is a planar trough device that can radially compress the fluid-fluid interface without introducing extra shear effects. We have customized it to be compact and transparent at the base such that it easily fits on the microscope stage of an inverted microscope setup. This leads to the second thesis statement of this work.

1.4.5 Thesis Statement II

Combined dilatational deformations and interfacial visualization can be achieved with a miniaturized radial Langmuir trough and this allows us to investigate the structure-property relationship of complex fluid-fluid interfaces.

CHAPTER 2

ACTIVE PARTICLE TRACKING MICRORHEOLOGY USING ARTIFICIAL THERMAL NOISE

Modified from a paper published in *Journal of Rheology*¹
Shalaka K. Kale², Andrew J. Petruska³, Joseph R. Samaniuk⁴

2.1 Introduction and Background

Characterizing mechanical properties of materials like polymers, paints, cosmetics, biological samples, etc., is essential from both an industrial and scientific standpoint, and such measurements can help to optimize the design, processing, and fabrication of material to improve product quality [29]. The rheological properties of a material govern its response when the material is deformed under stress or strain. When these properties are characterized at a macro-scale a conventional bulk rheometer is used, but such measurements will not capture rheological property variations that may exist a scale smaller than the length scale of deformation in the equipment. Examples of materials with micron-scale variations in rheological properties that are difficult or impossible to measure in a conventional rheometer include biological systems such as a cell's cytoplasm [71], protein interactions [72, 73] and biofilms [74, 75]. In order to probe the local rheological properties in such materials, microrheology can be used. Particle-tracking

¹ Reproduced from “S.K. Kale, A.J. Petruska, J.R. Samaniuk, Active particle tracking microrheology using artificial thermal noise, *Journal of Rheology* 6(1) (2022) 187-195” with permission from the Society of Rheology. All the supplementary material is provided in APPENDIX A.

² Primary Author and Graduate researcher, Department of Chemical and Biological Engineering, Colorado School of Mines, Golden, CO.

³ Co-Author, Department of Mechanical Engineering, Colorado School of Mines, Golden, CO.

⁴ Graduate Advisor and Author for correspondence, Department of Chemical and Biological Engineering, Colorado School of Mines, Golden, CO.

microrheology (PTM) uses colloidal-scale particles to deform the material at micron and sub-micron length scales, and has the advantages of: requiring small sample volumes, generally being non-destructive to the sample, requiring relatively short data acquisition times, and can capture high-frequency rheology beyond what is typical for bulk rheometers [26, 28, 36, 76-78]. For these reasons, along with advances in microscopy, microrheological investigations have become popular in the last few decades.

One of the simplest and most widely used techniques in microrheology is passive PTM [36, 79, 80]. It relies on the inherent thermal fluctuations of a particle, also known as the Brownian motion [26, 38, 40, 42, 81]. The inherent Brownian motion of the particle locally stresses the material, and the magnitude of particle displacement over time depends on the material's rheological properties. Passive PTM employs this fundamental relationship between displacement and material properties to measure the material's rheological properties. This relationship is described by the Langevin equation, which captures the dynamics of Brownian motion through a force balance. Consider a neutrally buoyant spherical particle with radius a dispersed in a purely viscous environment with viscosity η : It primarily experiences two types of forces: First, the fluctuating thermal force (f_{th}) arises from the continuous bombardment of the fluid molecules which sets the particle in random motion. Second, the dissipative drag force (f_d) retards the particle motion because of resistance from viscous drag. The overall net force acting on the particle is captured with the Langevin equation [40, 81]:

$$m \frac{dU}{dt} = -f_d + f_{th} \quad (2.1)$$

In equation 2.1, the left-hand side is the net force on the particle which is given by mass (m) times the acceleration (dU/dt) where U is the particle velocity. The right-hand side of the

equation is the sum of the stochastic force from thermal energy, f_{th} , and a deterministic drag force, f_d . Under the assumption of continuum limit in a viscous (or Newtonian) fluid, the drag force is given by the Stokes formula, $f_d = 6\pi\eta aU$, where $6\pi\eta a$ is viscous drag coefficient, ζ . The thermal force, on the other hand, is stochastic and uncorrelated. Thus, it can be modeled as white noise [40, 81]. Overall, f_{th} introduces the thermal energy, kT , where k is the Boltzmann constant and T is temperature, to the particle. In order to maintain a thermal equilibrium with the surroundings, the particle dissipates its kinetic energy back to the fluid, which is captured by f_d [40]. The relationship between the stochastic fluctuating force and the deterministic drag force is captured by the fluctuation-dissipation theorem (FDT) [40, 41]. FDT is a driving principle underlying the use of passive PTM.

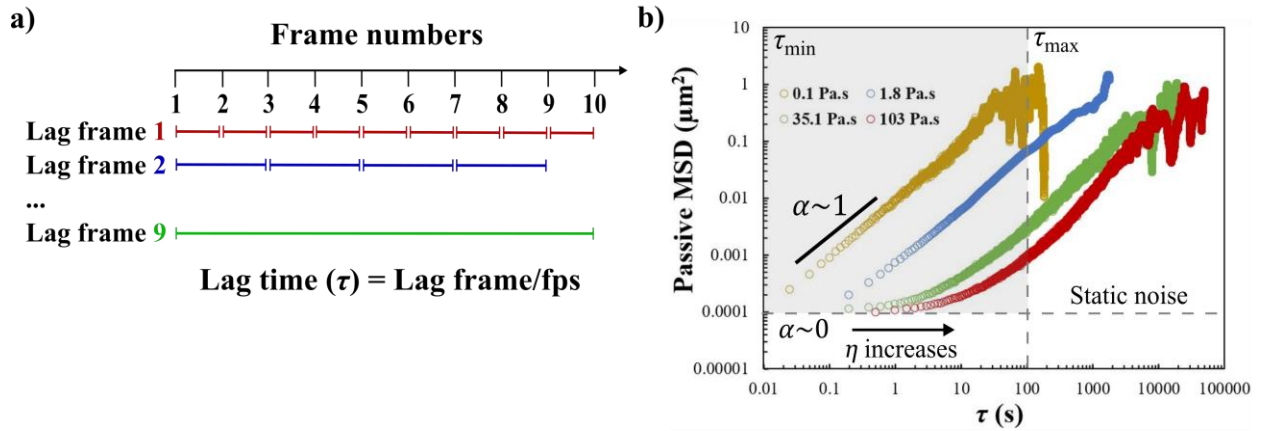


Figure 2.1 a) Schematic illustration that explains the definition of lag time (τ) b) x-direction passive MSD data as a function of τ of a single particle trajectory for different calibration (Newtonian) oils, 0.1 Pa.s (yellow circles), 1.8 Pa.s (blue circles), 35.1 Pa.s (green circles) and 103 Pa.s (red circles). Gray box represents the operating range of passive PTM for our setup.

In PTM, the probe's real-time Brownian motion is captured via video optical microscopy and the movie is converted to position versus lag time (τ) data (or tracks) using an image analysis software. As these tracks are random trajectories arriving from a fluctuating force, they

are treated statistically and reduced to an ensemble-averaged mean squared displacement (MSD) value as a function of τ . Further, the MSD is analyzed to obtain local rheological properties. The ensemble average can be taken over time or over multiple identical particles, but for this work we focus only on ensemble time average MSD of a single particle trajectory. Use of single particle tracking is advantageous because it focuses more on the local properties. Tracking single particle trajectories is also of high relevance in the field of biology where it is used to study the microscopic transport in cells [82, 83], investigating binding properties [84], diffusion and biomechanics using individual biomolecules like mRNA [85] or mitochondria [82].

Every MSD value at a given τ in x -direction (1d) can be written as, $\langle \Delta x^2(\tau) \rangle = \langle (x(t + n\tau) - x(t))^2 \rangle$, where the angle brackets represent ensemble time average, t is any time instance and $n = 1, 2, 3 \dots N$ where N is the maximum number of frames acquired in a video. To understand lag time, consider a video with ten frames (see Fig. 2.1a) acquired at a certain acquisition rate i.e., frames per second (fps). Each frame gives the absolute position of the particle and the difference of positions between the frames gives the particle displacement. Thus, the smallest displacements are captured at lag frame 1 or minimum lag time, $\tau_{min} = 1/fps$ and it corresponds to the minimum MSD value recorded. τ can take values between $1/fps \leq \tau \leq N/fps$, where N/fps is the total observation time (τ_{max}). As the lag frame increases the lag time step also increases, but the number of realizations decreases. Thus, MSD at smaller τ values are more statistically significant.

According to the Einstein equation [40], $MSD = 2dD\tau^\alpha$, where d is the number of dimensions in which the displacement is recorded, D is diffusivity of the probe particle in the sample, and α is the diffusive exponent, or the logarithmic slope of MSD. The value of α depends on the nature of the material and it can vary between $0 \leq \alpha \leq 1$ [40, 77, 80]. A slope of

zero indicates that the sample is elastic, while a slope of one indicates the sample is purely viscous, and anything in between represents a viscoelastic material. Values greater than 1 generally suggest that there is some external driving force such as drift or directed motion, and this condition is called as super-diffusive motion. For purely viscous liquids or Newtonian fluids probed in 1d, the MSD is given by, $MSD = \langle \Delta x^2(\tau) \rangle = 2D\tau$. Assuming that the particle satisfies the Stokes regime, the diffusivity of a particle in a Newtonian fluid is given by $D = kT/\zeta = kT/(6\pi\eta a)$, and thus the MSD becomes $\langle \Delta x^2(\tau) \rangle = 2kT\tau/(6\pi\eta a)$, the Stokes-Einstein-Sutherland relation [40, 86]. Since particle displacement is inversely proportional to the viscosity of the sample, the minimum displacement that can be resolved sets an upper limit on the maximum measurable viscosity for a particular observation duration. In PTM, the typical tracking/localization error or spatial resolution is specific to the equipment and depends on various factors like numerical aperture of the objective, signal to noise ratio during image acquisition, tracking algorithm, etc. [79, 87-89], but for our equipment and for most modern optical microscopes the accuracy of particle center point measurements is approximately 10 nm [40, 88]. Typically, for an optical microscope that uses visible light, this resolution and a 1 μm diameter particle, the maximum measurable viscosity is on the order of 10^0 Pa·s (or modulus on the order of 10^0 Pa), for periods of particle observation on the order of 10^4 sec (approximately 3 hours). This is illustrated in Fig. 2.1b that contains 1d passive MSD data for different Newtonian calibration oils at room temperature. For the 0.1 Pa·s viscosity oil the MSD curve has a slope of 1 for the entire range of observed lag times, but as the oil viscosity increases the slope of the MSD curve near lower lag times tends to zero despite the fact that the fluid is Newtonian. This limiting behavior is referred to as the “static noise” limit that arises due to the constraint on the spatial resolution of the setup [87] and is approximately $1 \times 10^{-4} \mu\text{m}^2$ for our setup. Typically,

passive PTM is performed on multiple particles for better statistics. However, here we are tracking single particle. To improve the statistics on our data we tracked each particle for sufficiently long period and there are about 50k and 125k frames to average for the first data point in 35.1 Pa·s and 103 Pa·s fluids. Many soft materials of interest such as adhesives, coatings, hydrogels, bio-scaffolds, etc. have much higher viscoelastic modulus than the range of PTM measurements performed over reasonable time scales. Here, note that the 103 Pa·s viscosity oil data shown in Fig. 2.1b required 16 hours of observation time. Thus, the feasible observation time, or τ_{max} , also contributes to the operating regime of passive PTM.

The typical upper limit of the passive PTM can be overcome by using small particles as probes [40]. However, in some cases where material heterogeneity is observed at small length scales it is not desirable to use small size particles as it may interfere with the continuum assumption of the Stokes regime [40] as studied by Cohen and Weihs in viscous honey samples [90]. Passive microrheology can also be investigated by using a light scattering technique called diffusive wave spectroscopy (DWS) but it is limited to using ensemble averaging of scattered light from multiple particles and cannot be used with a single particle. In this work, we focus to overcome the limitations of passive PTM, in particular the maximum value of the measurable rheological properties. We use active microrheological methods for this purpose. Active PTM is performed when a probe particle is subjected to external driving forces such as magnetic force (magnetic tweezers), or optical forces (optical tweezers) [28, 49, 77, 78, 91, 92]. Conventionally, external forces in active PTM are applied as either sinusoidal inputs, or as step stress inputs for creep compliance measurements. Challenges with these techniques are that often large forces are required to obtain sufficient deformation. To generate large forces large currents are needed with electromagnets, and for optical tweezers high intensity lasers are needed. In both situations, the

result can be local heating of the sample [78]. Moreover, large deformations may require a known strain field before the extraction of true rheological properties. This is especially problematic for small sample containers/geometries, or when there are particle-scale heterogeneities within the sample. Thus, small deformations of spherical particles are favorable as they require smaller forces, remain closer to thermal equilibrium, and allow application of Stokes Law.

In this work we accomplish this using a form of active microrheology with single-coil magnetic tweezers where a superparamagnetic probe particle is driven by artificial thermal noise. Using noise signals as external forces has proven to be useful in past studies of cell stimulation and signaling [93] and for studying Brownian motion in active matter [94]. The artificial thermal noise signal used here is analogous to thermal fluctuation forces, f_{th} , but with an amplitude that is orders of magnitude larger. Due to the larger amplitude, the artificial thermal noise provides energy to the probe particle with magnitudes much greater than kT , and thus the displacement of the probe particle can be amplified orders of magnitude. Like other active microrheological approaches, the addition of artificial thermal force violates the FDT out of necessity, but the magnitude of excess energy is generally small enough to maintain thermal equilibrium. The advantage of artificial thermal noise as the external driving force is that it allows the use of hydrodynamic models like the Stokes-Einstein-Sutherland equation to extract rheological material functions generally without the need for a defined strain field. In this work, we produce 1d artificial thermal noise that is used to probe a single superparamagnetic probe particle placed in Newtonian fluids with viscosities beyond the typical operating range of passive PTM.

2.2 Materials and Methods

2.2.1 Single-coil Tweezer Setup

Fig. 2.2a shows the schematic setup of the single-coil electromagnetic tweezer equipment. The electromagnetic tweezer is made of a metal core (6 mm diameter and 150 mm long) and copper wound coil (American wire gauge 23 and 2500 turns). The core material (EFI Alloy 79, Ed Fagan Inc., USA aka HyMu80, Carpenter Technology Corp., Reading, PA) was selected such that it has high permeability and low coercivity, an important consideration here as the magnetic fields generated are strongly time dependent. The magnetic force depends on the field gradient, field strength, the separation distance (d_0) between the tip of the core and probe particle, and the particle properties. The needle-like shape of the core increases the field gradient near the tip [95], and the initial separation distance was maintained constant during all experiments at 175 μm .

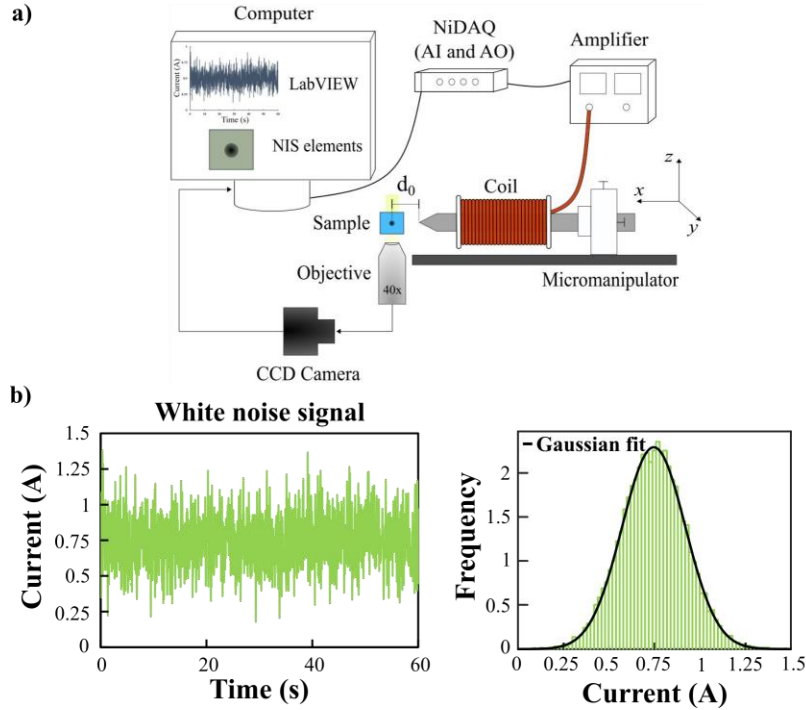


Figure 2.2 a) Schematic setup of the single-coil electromagnetic tweezer used to generate artificial thermal noise b) (Left) White noise signal with an average current of 0.75A, (Right) Random Gaussian distribution (green line) of the same white noise signal with a Gaussian fit (solid black line).

The electromagnetic coil is attached to a three-axis manual micromanipulator (MS3, XYZ translational stage, Thorlabs, USA) to position the coil in 3d space with a resolution of 250 μm /revolution. The current supplied to the coil was controlled using a custom LabVIEW program that outputs the desired signal to the signal generating device (NI 9263, National Instruments, USA) from where the signal is sent to the amplifier (TS200, Accel Instruments, USA) for amplitude modification. The applied artificial thermal noise was a white noise signal (see left part of Fig. 2.2b) generated using MATLAB's built-in function with known bounds on the minimum and maximum current (e.g., a white noise signal between 0 to 1.5 A and average 0.75 A). This script was then integrated in a LabVIEW code that controlled the final signal input

to the electromagnetic coil. For this work the signal input frequency was held at 25 Hz, which was selected based on the cutoff frequency of the electromagnetic coil (see Fig. S1 of Supplementary Material or Fig.A1 of Appendix A). The white noise signal was random, with a Gaussian distribution (see right part of Fig. 2.2b). In Fig. 2.2a, the sample chamber is shown as a blue square box with a superparamagnetic probe particle. The sample chamber was a square glass capillary (BMC-020-076-50, Friedrich & Dimmock Inc., USA). Newtonian calibration fluid with viscosity 35.1 Pa·s (Test fluid E40000, Thermo Fischer, France) was used in our experiments. Monodisperse spherical superparamagnetic particles of 1.05 μm diameter (Dynabeads MyOne, Carboxylic acid, Invitrogen, USA) were used. To prepare the stock samples, 1 μL of 1 mg/mL aqueous particle solution was allowed to dry in a sample vial, and then 2 mL of calibration fluid was poured into the same vial and mixed by hand. The final particle concentration in the stock sample was 0.0005 mg/mL, which ensured that the particles were on average at least 10 diameters away from each other inside the capillary. The square glass capillary was placed on the stage of a Nikon Eclipse Ti-U inverted optical microscope, and images were recorded with a CMOS camera (C13440-20CU, Hamamatsu ORCA-Flash4.0 V3 digital) attached to the optical microscope, and unless otherwise indicated images were captured using a CFI60 Plan Apochromat 40 \times objective (NA 0.8, WD 3.5 mm). The camera exposure time (σ) was 10 ms and the frame acquisition rates (f_{ps}) of 5 Hz and 2.5 Hz were used i.e., τ_{min} is 0.2 s and 0.4 s respectively. In the work by T. Savin and P.S. Doyle [87] they show that these settings ($\sigma/\tau_{min} \ll 1$) help to reduce the ‘dynamic error’ in particle tracking. It is the error in tracking the particle when it is moving during the exposure time or when the camera shutter is open. The NIS elements software was used for live sample scanning and selecting a desired/target probe particle in the center of the glass chamber. The length measurement tool of

NIS elements software aids estimating the separation distance d_0 ($175 \mu\text{m}$) and helps in 3d alignment of core tip position. Before any measurement, a single probe particle was selected, and the core tip was aligned such that they both were in the same focal plane and at a distance d_0 . The superparamagnetic probe particles used in this work have a high saturation magnetization (36 kA/m , as provided by Invitrogen, USA) and this value was significantly greater than the maximum magnetization applied by the electromagnetic tweezer, thus ensuring that the particles are not saturated during the experiments. The two characteristic features of a superparamagnetic particle are that the magnetization occurs only in the presence of an external magnetic field, and that it can switch its direction of magnetization almost instantaneously with negligible hysteresis when the field direction changes [40]. Although the latter feature would be essential for multiple-coil magnetic tweezers where field direction can rapidly change, the most important property for single-coil tweezers is the former.

2.2.2 Force Calibration

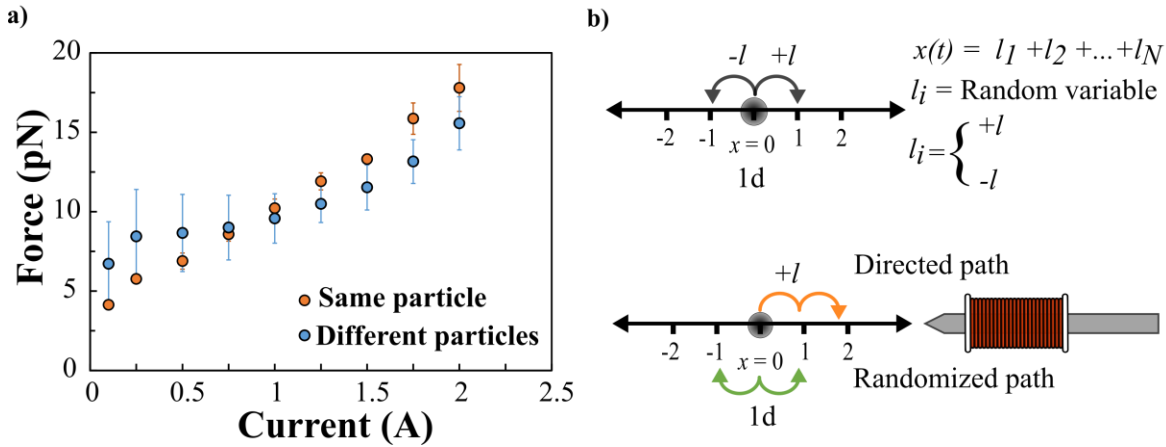


Figure 2.3 a) Force calibration for single-coil electromagnetic tweezer as a function of input current b) Illustration of 1d particle diffusion in absence (top) and presence (bottom) of electromagnetic tweezer.

Fig. 2.3a shows the magnetic force calibrated as a function of current at a distance d_0 . To estimate the force at a given current value we use Stokes law, which states that in a purely viscous fluid the drag force (F_d) is given by $F_d = 6\pi\eta av$. In the presence of a magnetic force (F_m), and when fully developed flow exists, the drag force equals the magnetic force and one can say that $F_m = 6\pi\eta av$, where v is the velocity of the particle with radius a in a Newtonian fluid with viscosity η . For the purpose of force calibration, we use standard Newtonian fluids with a known viscosity of 6.27 Pa·s (Test fluid E6000, Thermo Fischer, France) mixed with low concentrations of superparamagnetic 1 μm diameter particles. For every calibration point, a single particle was dragged for 5 μm , enough to achieve steady-state velocity. The velocity was estimated by tracking the particle position as a function of time. Over the course of particle travel, the change in force due to the change in distance between the particle and the electromagnet was observed to be less than 5 %. The blue circles in Fig. 2.3a represents the average force estimated for ten different superparamagnetic particles at a given current in the same specimen. The same ten particles were used for each current amplitude. The standard deviation as indicated by the error bars may originate from the difference in physical properties of the individual particle such as volume, shape or magnetic susceptibility. To ensure this is true, we performed three repeats of force calibration on a same single particle and the results are shown with orange circles in Fig. 2.3a. The standard deviation is less than it is with the “Different particles” data set, indicating the presence of variability in particle properties. For the range of applied currents, both calibration data sets show a linear trend for the force as a function of current. The non-zero y-intercept indicates that there is some remnant magnetization, and to mitigate contributions from this the coils were degaussed between every measurement.

2.2.3 Displacement Analysis

The aim of our active measurement is to enhance the inherent Brownian motion of the particle in 1d with artificial thermal noise. Diffusion of a true Brownian particle in 1d can be understood with a 1d random walk model, illustrated in Fig. 2.3b. At $t = 0$ we can consider a particle at position $x = 0$ and ask how far the particle is likely to travel after N steps. During each discrete time step, we assume that the particle moves with a step size of l , with equal probability in either the positive or the negative direction. As all the steps are independent of each other, and have equal probability, the expected value or the mean displacement of the particle can be estimated as $\langle x(t) \rangle = \langle \sum_1^N l_i \rangle = 0$, where l_i is defined in Fig. 2.3b. The zero mean displacement ensures that the particle is moving randomly, but to answer how much the particle is likely to travel in N steps we consider the variance of particle position, or the mean squared displacement (MSD), which is non-zero. Here, the MSD is given by, $\langle x^2(t) \rangle = \langle (\sum_1^N l_i)^2 \rangle \propto Nl^2 \propto t$.

Although the mean particle position is centered around zero, its MSD increases linearly with time. This quantitative relationship between the MSD data and observation time can then be used to estimate the material properties, as shown by the Stokes-Einstein-Sutherland equation. If we now consider a case where the particle experiences a force of random magnitude, but only in one preferential direction (illustrated in the bottom of Fig. 2.3b as the “directed path”), as we would expect from a single-coil electromagnetic tweezer arrangement, then on average the particle will preferentially move in that direction. As a consequence, the mean displacement will be linearly proportional to time $\langle x(t) \rangle = Nl \propto t$ and the MSD will be proportional to the square of time, $\langle x^2(t) \rangle \propto N^2 l^2 \propto t^2$. Thus, the directed motion due to the single-coil tweezer becomes super-diffusive and it results in MSD data that has a slope of 2. This information cannot be directly used with traditional hydrodynamic models that require diffusive transport to estimate material

properties. However, the directed motion of the particle is an artifact of the one-sided nature of the random force applied using the single-coil tweezer, but otherwise no different from thermal fluctuations that gives diffusive motion. In order to extract diffusive motion from a super-diffusive motion, we postprocess the directed displacements such that all recorded displacements are given an equal chance to take on a positive or negative value that consequently returns a random path. This type of displacement modification is acceptable, as we perform active measurements in a viscous fluid that has no memory i.e., all the displacements are independent of one another, and this allows us to manipulate the observed super-diffusive displacements without introducing a bias. In effect, this postprocessing step is the virtual equivalent of allowing the electromagnetic coil to pull, as well as push, the particle, resulting in an artificial diffusive motion that gives MSD data with a slope of 1. This modified diffusive MSD can then be analyzed using the Stokes-Einstein-Sutherland model.

2.3 Results and Discussions

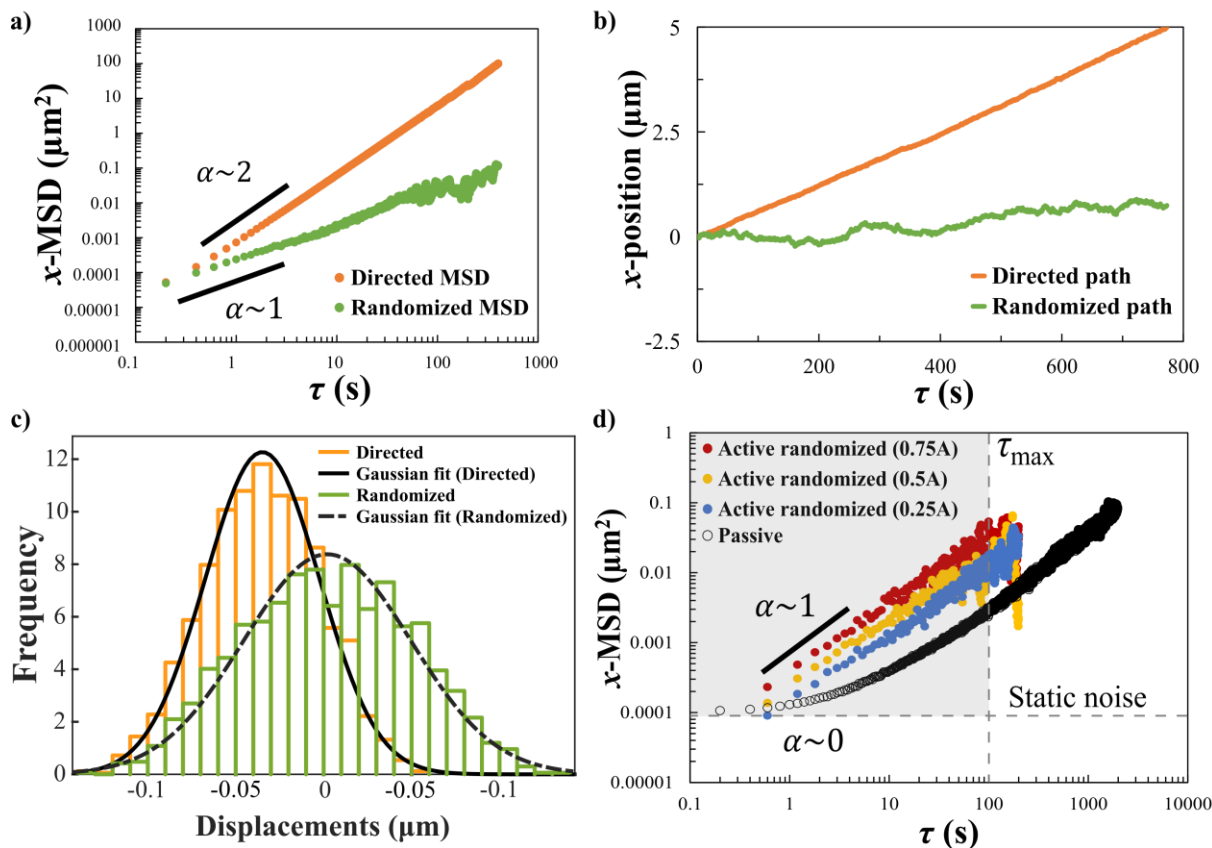


Figure 2.4 a) x -MSD data as a function of lag time estimated for active microrheological measurement performed on a $35.1 \text{ Pa}\cdot\text{s}$ calibration oil using a white noise signal with average current of 0.5 A . Orange data is Directed MSD (with slope 2) and green data is Randomized MSD (with slope 1) b) x -position versus lag time data for the same data set in part a. c) Gaussian random distribution of the displacements of a particle present in $35.1 \text{ Pa}\cdot\text{s}$ calibration oil evaluated at lag frame 1. Orange data shows the Directed displacements with a non-zero mean displacement while the green data shows Randomized displacements with a mean displacement of zero. Black solid line and black dashed line are the Gaussian fit for the directed and randomized displacement distributions respectively. d) Passive and active x -MSD measurements for $35.1 \text{ Pa}\cdot\text{s}$ Newtonian fluid. Active measurements are performed on a same single particle with three different white noise signals with average currents, 0.25 A (blue solid circles), 0.5 A (yellow solid circles) and 0.75 A (red solid circles). Gray shaded area is the typical operating range of passive PTM setup.

Fig. 2.4a shows active 1d MSD or x -MSD data as a function of τ for a single superparamagnetic particle embedded in $35.1 \text{ Pa}\cdot\text{s}$ Newtonian calibration fluid. Here, the probe

particle was subjected to a white noise signal with average current of 0.5 A or a corresponding average force of 7.24 pN. Since the active force acts only on one side of the probe particle, the resulting x -MSD is super-diffusive with a slope of 2 and we call this the ‘Directed MSD’. The position versus time data of the probe particle in the Fig. 2.4b shows the corresponding ‘Directed path’ (orange data). The non-zero mean displacement of this directed motion was confirmed by evaluating the Gaussian of the ‘directed’ displacements (see orange data in Fig. 2.4c). Further, to analyze the Directed MSD data set using the Stokes-Einstein-Sutherland equation we postprocess the particle position such that it produces an apparent random path. We achieve this by using a MATLAB algorithm in which the direction of the displacements obtained from ‘Directed path’ are altered such that each displacement is equally likely to occur either in positive or negative x -direction. This randomization does not affect the statistical variability of MSD magnitude beyond what is expected from a typical passive PTM experiment. Details of the MATLAB algorithm are provided in the Supplementary Material (or in Appendix A). The resulting ‘Randomized path’ is the green line in Fig. 2.4b, and its zero-mean random Gaussian distribution is shown in Fig. 2.4c (green data set). Note that the randomization approach only changes the probable direction and does not change the magnitude of the displacement. The magnitude of each displacement originates from the actual force acting on the probe particle. The ‘Randomized path’ is used to generate x -MSD data which we call the ‘Randomized MSD’ (see Fig. 2.4a). The slope of Randomized MSD is 1 and one can use the Stokes-Einstein-Sutherland equation to analyze this data to extract the viscosity of the medium. In order to calculate a viscosity from the active Randomized MSD (MSD_R) data, we must quantify the energy applied to the probe particle. To achieve this, we need to appreciate that the active MSD_R is the product of the superposition of displacements from thermal forces as well as the added magnetic forces.

The stochastic nature of the two forces means that the relationship between their average energies and the MSD is similar, and can be expressed as:

$$MSD_R = \frac{2}{6\pi\eta a} (kT + kT_{act})\tau \quad (2.2)$$

Where, kT_{act} is equivalent to externally added average artificial thermal energy, or the active energy, T_{act} is the apparent temperature increase if the active energy added to the system were expressed as thermal energy. The right-hand side depends the average force acting on the particle. MSD_R can also be written as:

$$MSD_R = \frac{2kT_{eff}}{6\pi\eta a} \tau \quad (2.3)$$

Where T_{eff} is an effective temperature of the particle surroundings, which, due to the extra energy added to the system, is greater than the measured temperature, as shown by its relationship to the ambient temperature: $T_{eff} = T + T_{act}$. Rearranging equation 2.2 and 2.3 we get an expression from which T_{act} can be estimated:

$$T_{act} = \frac{MSD_R}{\left[\frac{2k}{6\pi\eta a} \tau \right]} - T \quad (2.4)$$

The ratio of active to thermal energy can be expressed as $c = kT_{act}/kT$, and is a dimensionless quantity that is independent of the fluid properties and indicates whether the probe particle is driven primarily by artificial thermal forces ($c \gg 1$), or by background thermal forces ($c \ll 1$). Since c depends only on the background temperature and the magnetic force, and not on the fluid properties, c values calculated by applying various active noise force magnitudes to a known particle in a fluid of known rheological properties can act as calibration values for a particular electromagnetic coil. Thus, one can apply a known value of c to similar probe particles

in a Newtonian fluid with unknown viscosity and calculate that viscosity from MSD_R . The x -MSD results shown in Fig. 2.4d are the active MSD_R obtained from three different white noise signals applied to a same probe particle in 35.1 Pa·s fluid. By applying the signal to the same probe particle, we ensured that the particle properties remain unchanged during the estimation of c values. We applied a white noise signal with increasing average current (or increasing average artificial thermal force) with values 0.25 A (5.2 pN), 0.5 A (7.5 pN) and 0.75 A (8.3 pN). The corresponding c values obtained from these measurements are $c_{0.25} = 5.10$, $c_{0.5} = 9.01$ and $c_{0.75} = 15.31$. The results show that we can probe a Newtonian fluid with a viscosity one order of magnitude higher than the operating range of passive PTM (see the gray shaded area in Fig. 2.4d). To get a perspective of the active energy magnitude in comparison to thermal energy, the passive x -MSD (black circles) of a thermally driven particle is shown in Fig. 2.4d. In order to use the c value as a calibration constant to determine the viscosity of an unknown fluid, high reproducibility is required. However, as mentioned earlier, the variability in particle properties of an individual probe particle significantly affects the magnitude of applied forces and thus translates to variability in the estimated c values. For a white noise signal with average current of 0.75 A applied to three different probe particles in the same specimen (35.1 Pa·s fluid) the average c value turned out to be $c_{0.75} = 17.98 \pm 4.06$. On the other hand, three repeats of white noise signal with an average current of 0.5A applied to a same probe particle present in 35.1 Pa·s fluid gave an average c value of $c_{0.5} = 8.68 \pm 0.52$. These results for c values align with our force calibration data (see Fig. 2.3a) where we observe that there is high error involved in calibration of different particles as compared to the calibration of a single particle. The force calibration data in Fig. 2.3a can be used to estimate variation in particle properties. For instance, consider that the error in force calculation of an individual particle originates from its magnetic susceptibility. For

low field intensities, particle magnetization and susceptibility are linearly proportional and the theoretical magnetic force (F_m) can be estimated as $F_m = \mu_0 V \chi H \nabla H$, where H is the field intensity [40]. In Fig. 2.3a the force has an error of approximately 20%, which translates to an error of approximately 45% in magnetic susceptibility. Similarly, variations in other physical properties like the particle shape and volume can also contribute to the error in force estimation. We have observed from scanning electron microscopy of particles deposited on silica substrates (see Fig. S2 of Supplementary Material or Fig. A2 of Appendix A) that the particle radii can vary on the order of 0.05 μm , which for a 1 μm diameter particle leads to 30% variability in particle volume. Therefore, characterization of the probe particle is critical for the accuracy of this method in measuring viscosity in unknown materials.

This technique, where postprocessing uses the assumption that directionality of displacements is random and independent of one another, is not applicable for a viscoelastic material. However, there are ways to overcome this in future efforts, as one might use a pair of electromagnetic tweezers placed on opposite sides of the probe particle to produce forces in either direction in a closer analog to 1d thermal noise without the need for postprocessing, or a single-coil approach may be used with ferromagnetic particles if the timescale of particle rotation is much longer than the time scale of magnetic field fluctuation. In this way a single coil could be made to push as well as pull the probe. In such measurements with viscoelastic materials, identification of the boundary between linear and non-linear regimes could be established with a set of active microrheology creep compliance measurements or oscillatory strain sweep measurements and they can be performed either before or after the artificial thermal noise measurements.

2.4 Conclusions

Artificial thermal noise can be used to probe a Newtonian material with a viscosity beyond the typical operating range of passive PTM. A single-coil electromagnetic tweezer was used to apply external energy to a 1 μm diameter superparamagnetic particle on the order of approximately 10 kT. The primary advantage of the technique is the potential to apply it in environments where micron- and sub-micron scale material heterogeneities preclude the use of traditional active microrheology methods. However, with heterogenous materials, it is necessary to ensure that the probe particle experiences continuum environment and near thermal equilibrium conditions to satisfy the assumptions of the Stokes-Einstein-Sutherland equation [40]. The near thermal equilibrium conditions are maintained as we introduce small deformations to material which also reduces the force amplitude. One approach to check for continuum environment to particles with different sizes or different surface chemistries [40]. Other advantages of this technique are that it showcases the approach to build stochastic magnetic forces and these can act as unique stimulations in biological cells [93] and such forces can offer new in-sights to understand or mimic the mechanisms of natural [96] or synthetic [97] active matter. We expect that the method can be extended to probe viscoelastic materials via either a pair of electromagnetic tweezers on opposite sides of a superparamagnetic probe particle, or with a single-coil and a ferromagnetic particle where the timescale of rotation is much longer than the time scale of field fluctuation. A limitation of any of these techniques utilizing magnetic tweezers with a single particle is that significant error can be introduced from variability in the physical properties of that individual particle. Although particle fabrication technology has evolved greatly over the previous three decades, it is clear that the variation in the magnetic susceptibility from particle to particle is high, which also translates to error in the measured

viscosity when using artificial thermal noise. Despite this, the technique here provides a foundation for understanding how we may use external noise as an input signal to extend PTM beyond current limitations.

CHAPTER 3

A MINIATURIZED RADIAL LANGMUIR TROUGH FOR SIMULTANEOUS DILATATIONAL DEFORMATION AND INTERFACIAL MICROSCOPY

Modified from a paper published in *Journal of Colloid and Interface Science*¹

Shalaka K. Kale², Andrew J. Cope³, David M. Goggin⁴, Joseph R. Samaniuk⁵

3.1 Introduction

Complex fluid-fluid interfaces are common in many natural and synthetic systems, such as pulmonary surfactants adsorbed at lung alveoli [98], biofilms [99], biological membranes [100, 101], foams and emulsions [63, 102-106], particle laden interfaces [107-112], colloidal hydrogels [113], etc. The interfacial properties in these systems are often accompanied with underlying complex microstructures that have significant impact on their bulk phase dynamics, functioning, stability, and mechanical response upon deformations [16, 60, 70, 114-116]. For example, the morphology of lung surfactants is significantly altered in the presence of cholesterol, affecting its surface viscosity and dynamics [117]. Biofilm strength is governed by the film's viscoelasticity, that can influence its microstructure [99]. The formulation and stability

¹ Reproduced from "S.K. Kale, A.J. Cope, D.M. Goggin, J.R. Samaniuk, A miniaturized radial Langmuir trough for simultaneous dilatational deformation and interfacial microscopy, *Journal of Colloid and Interface Science* 582 (2021) 1085-1098" with permission from *Journal of Colloid and Interface Science*. All the Supporting Material is added in APPENDIX B.

² Primary Author and Graduate researcher, Department of Chemical and Biological Engineering, Colorado School of Mines, Golden, CO.

³ Co-Author, Department of Chemical and Biological Engineering, Colorado School of Mines, Golden, CO.

⁴ Co-Author, Department of Chemical and Biological Engineering, Colorado School of Mines, Golden, CO.

⁵ Graduate Advisor and Author for correspondence, Department of Chemical and Biological Engineering, Colorado School of Mines, Golden, CO.

of foams and emulsions also depends on their microstructure [102, 103], while the structural self-assembly of colloidal particles can be correlated to their interactions and application in foods, coatings, films, and optical devices [107, 110, 118, 119]. The coupling of interfacial rheology with visualization techniques can thus play a crucial role in understanding and manipulating structure-property relationships in such interfacial systems. Interfacial rheology commonly involves two types of deformations, constant area or shear deformations, and constant shape or dilatational deformations. Methods for true interfacial shear deformations [16, 60, 64, 68, 69] along with visualization [109, 120-122] have been well developed, however methods for achieving true dilatational deformations with in-situ visualization are uncommon and challenging.

Surface stress tensor is required to understand the stress-strain relationship of a complex fluid-fluid interface. It has contributions from the surface tension that varies according to the interfacial material's surface concentration and extra rheological stresses that are a result of the interface's resistance to change in area and shape. When the interface is deformed symmetrically, retaining its shape, then the extra rheological stresses are then dominated by the dilatational response. This dilatational response helps in obtaining a full rheological description in the case of compressible materials such as polymers or surfactants at fluid-fluid interfaces [123-131]. In certain cases, it is more relevant than shear deformations, for example, protein particle formation accelerates under dilatational deformation [132-134]. Commercially available methods for dilatational deformations include drop or bubble-based techniques or rectangular Langmuir-Pockels trough apparatus. In drop or bubble-based methods the dilatational deformations are achieved by changing the drop or bubble volume. Surface tension measurements performed in these methods rely primarily on the drop or bubble shape analysis,

and the accuracy is strongly affected by the changes in drop or bubble shape. These changes can occur either due to wrinkling (for structured interfaces) or sagging (effect of gravity) [60, 61]. There are approaches for improving this accuracy [60], but drop and bubble-based methods have other challenges such as the lack of control over surface coverage and their incompatibility with densely packed complex structured interfaces that may be associated with anisotropic stresses. A rectangular Langmuir trough produces planar dilatational deformations by moving barriers at a fluid-fluid interface. An important drawback of this method is that at high compressions the deformation can involve changes in both area and shape of the interface. This induces mixed deformation fields at the interface activating both shear and dilatational moduli that are difficult to uncouple [60-62, 70] and therefore this makes the method non-ideal for pure dilatational deformations. Similar mixed deformation fields can also occur in a drop-based method when interfaces with complex microstructures are investigated [61, 135]. These constraints of the above techniques highlight the necessity for methods that can truly isolate dilatational deformations. Several efforts have been made to obtain pure dilatational deformations in a planar geometry. Some methods included radial compressions [136-139], while others implemented symmetric isotropic deformations using movable [140] or elastic [141] barriers. In the design by Abraham et al. [136], a Teflon cup with sloping walls was used to compress the interface by moving the cup upwards while simultaneously emptying the fluid from the bottom. This approach had potential issues like sample leakage, sample adsorption on the walls, and increased complexity in mechanical analysis. Matsumoto et al. [138] implemented a unique design for radial compression where they used twenty curved blades placed at the interface, which operated like an iris diaphragm of a lens. Although the diaphragm blades avoided leakage during the compression, the movement of the blades could potentially cause rotational deformations near

the edges. Miyano et al. [140] built a trough with four movable barriers, but the no-slip conditions and sticking of the interfacial material at the barrier produced undesirable shear stresses. Bohanon et al. [141] improved on this design and eliminated such shear effects by using an elastic barrier instead of a stiff barrier for isotropic interfacial compression. These listed designs found application in limited cases because of their design limitations [60, 61]. Recently, a more versatile Langmuir trough with general applicability for studying pure dilatational deformation in fluid-fluid interfaces was proposed by Pepicelli and co-workers [61], which they refer to as the “radial” trough. Similar to the work from Bohanon et al. [141], they used an elastic barrier that ensured elimination of shear effects. The elastic barrier was held by twelve fingers with radial symmetry to create an isotropic, planar compression of a complex interface. For a complex and structured fluid-fluid interface, the interfacial stress tensor is given by a combination of isotropic stress originating from surface-tension and the extra rheological surface stress due to interfacial deformation. This extra stress contains both isotropic (dilatational) and deviatoric (shear) effects that are difficult to deconvolute especially when using a commercial apparatus like a rectangular Langmuir trough for interfacial deformation. In this regard, the radial Langmuir trough developed by Pepicelli et al. [61] has an advantage since it has the ability to avoid shear deformations. In their work, they also derived a constitutive ‘neo-Hookean’ model for elastic interfacial stresses that theoretically elucidates the separation of mixed deformation fields and lays a foundation for developing 2D constitutive models for viscoelastic materials.

In addition to isolating dilatational deformations, investigation of the interfacial morphology can aid in correlating structure and the changes in dilatational properties [126, 142, 143] and can further facilitate development of constitutive models [60]. The design constraints of most of the devices discussed previously makes it difficult to incorporate methods that can

analyze interfacial morphology while simultaneously deforming the interface. Thus, and in general, interfacial visualization with dilatational deformations is accomplished *ex situ*.

Langmuir-Blodgett (LB) depositions and subsequent use of atomic force microscopy (AFM) [110, 144-146] fall under this category. Brewster Angle Microscopy (BAM) in combination with Langmuir troughs can be used to study interfacial structure formation *in situ* [147-149], but it is generally only useful for resolving domain formation in interfaces at the micron scale.

Additionally, the oblique angle configuration of a conventional BAM produces spatial distortion in the acquired images, impairing its quality [150]. Optical or confocal microscopy is another way that can be incorporated into commercially available Langmuir troughs [66] or drop-based methods [142] for interfacial visualization, but the complexity of combining a microscopy setup with these techniques requires special customizations and is thus a considerable hurdle.

Moreover, limitations like the presence of mixed deformation fields cannot be neglected for these approaches. Doing a similar visualization modification with the radial Langmuir trough designed by Pepicelli and coworkers [61] is an added challenge primarily due to its large size. In our work we overcome this hurdle by designing a simple miniaturized radial Langmuir trough that can perform *in-situ* microscopy visualization of the interface while symmetrically deforming it.

We develop a radial Langmuir trough designed to fit on a standard inverted microscope, a development that allows us to perform simultaneous interfacial visualization and pure planar dilatational deformations. There are two distinct parts of the assembly: a reservoir, or trough, to contain the bulk fluid phases, and a support structure for the elastic barrier that includes a linear stage and optical diaphragm to actuate motion of the barrier. The reservoir is a custom sample container with a glass bottom that enables microscopy on an inverted microscope. Interfacial

compression is carried out with an elastic barrier attached to the tips of six “fingers” that sit at the interface in radial symmetry. The heads of these fingers are surrounded with a round optical diaphragm that acts to actuate all six fingers simultaneously. We utilize this equipment to directly observe poly(*tert*-butyl methacrylate) (PtBMA) and dipalmitoylphosphatidylcholine (DPPC) spread at an air-water interface with phase contrast microscopy and epifluorescence microscopy, respectively. Viscoelastic properties of monolayered polymer thin films affect a wide range of technological applications including lubrication, coating, wetting and dewetting, biocompatible surfaces, etc. [131, 151]. PtBMA is an acrylate polymer that belongs to this family, and is well-studied with respect to its interfacial rheological properties [151-154] making it a suitable system for this work. DPPC is a major component of a mixture of lung surfactants present at the air-water interface of lung alveoli [155-158] and undergoes dilatational deformation during each breathing cycle. As such, the dilatational interfacial rheological properties of DPPC have been the focus of numerous studies [98, 156, 159, 160] and makes for another model system that we investigate in this work. The ability to capture morphology with the radial Langmuir trough is exploited in this work to quantify mechanical properties and film thickness of PtBMA at an air-water interface, and to investigate relationships between morphology and surface pressure in DPPC at an air-water interface. Moreover, for both materials, we perform independent surface pressure measurements with our radial Langmuir trough using a Wilhelmy probe and compare the results with measurements performed on a commercially available rectangular Langmuir trough. Due to the reduced size of the radial Langmuir trough developed here, there is potential for the trough length scales to interact with capillary length scales, and as a consequence we quantify and discuss the influence of capillary interactions on surface pressure measurements made with Wilhelmy probes.

The chapter is divided into three main sections. Section 2 is devoted to a brief explanation of the concept and design of the radial Langmuir trough instrument. Section 3 talks about the materials and methods used in experiments. Section 4 covers the results and discussion for interfacial measurements of PtBMA and DPPC at air-water interface. Challenges associated with any miniaturized Langmuir trough design, such as the influence of capillary deformation on the measured surface pressure, has been reported in last part of section 4.

3.2 Instrumental Concept and Design

The radial Langmuir trough is designed to fit on an inverted microscope stage and is comprised of two main components. The first component is the compression assembly, shown in Fig. 3.1, that is in contact with the interface and responsible for producing interfacial deformations. Fig. 3.1a shows the exploded view of the compression assembly and Fig.3.1b shows the assembled view. A base plate with outer diameter (OD) of 110 mm and 5.3 mm height is made of polylactic acid (PLA). It holds six linear slide bearings (see Fig.3.3) spaced 60 degrees apart around a 29.5 mm opening in the middle of the base plate. Six PLA ‘fingers’ are placed on top of these linear slide bearings and support an elastic band that contacts the interface. This elastic band is a 9.5 mm inner diameter, non-latex, medium force, orthodontic band (Sonic Dental Supply, USA). It is situated at the finger-tips such that the interface is pinned to the band and acts as the barrier (see Fig. 3.3). A PLA support plate is placed on top of the base plate to provide support and coupling between the linear stepper-motor and optical diaphragm. The 3D modeling of these three PLA parts was performed in SolidWorks software and they were fabricated via 3D printing (Ultimaker 3 Extended, USA). Each part was printed with a PLA filament of 2.85 mm diameter (Hatchbox, USA), with a 60 μm layer thickness and 30% infill density. Fig. 3.1b shows the final setup of the compression assembly.

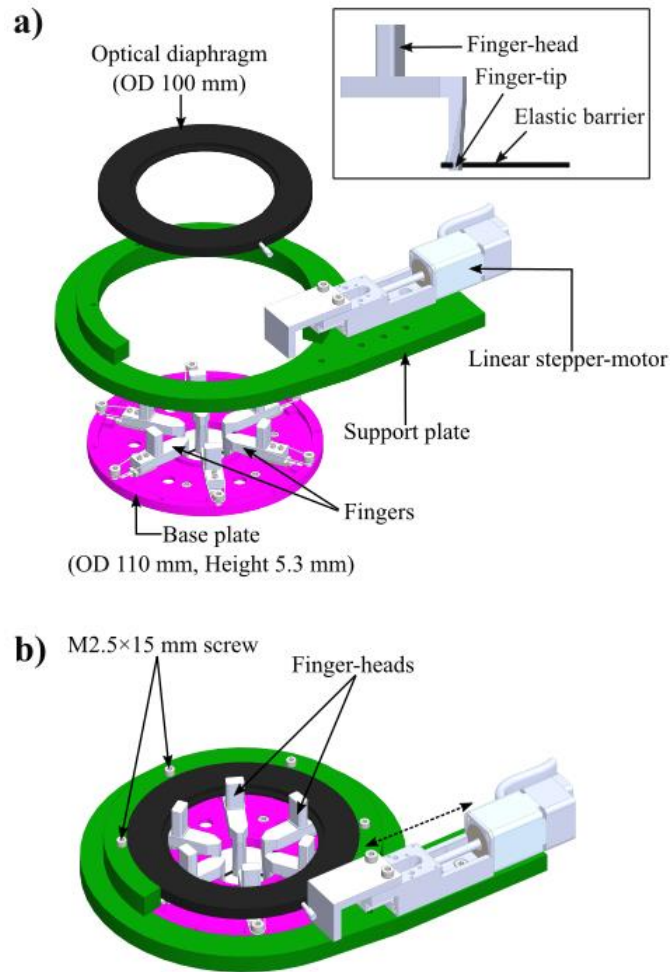


Figure 3.1 Schematic representation of compression assembly. a) Exploded view: Base plate holds six fingers that support the elastic barrier at each finger-tip. Inset shows schematic side-view of a single finger and the position of the elastic barrier. Support plate couples the base plate and optical diaphragm and holds a linear stepper-motor that actuates compression. OD stands for outer diameter. b) Assembled view: Support plate is fixed to the base plate with M2.5×15 mm screws while the optical diaphragm is in compression fit. Optical diaphragm surrounds the finger-heads and is actuated by the stepper-motor. The dashed, double-arrow line indicates the motion of the stepper-motor. The optical diaphragm further actuates the finger motion and thus the elastic barrier position.

Radial movement of the fingers is driven by opening and closing of the 100 mm wide optical diaphragm (Edmund optics, USA). This motion of the diaphragm is controlled with the

linear movement of the stepper-motor as indicated by the double-headed dashed arrow line in Fig. 3.1b. The optical diaphragm is compression fit within the inner rim of the support plate and is located such that it sits concentric around the head of the trough fingers. The support plate is attached to the base plate using M2.5×15 mm screws, as indicated in Fig. 3.1b, to provide structural stability to the entire compression assembly.

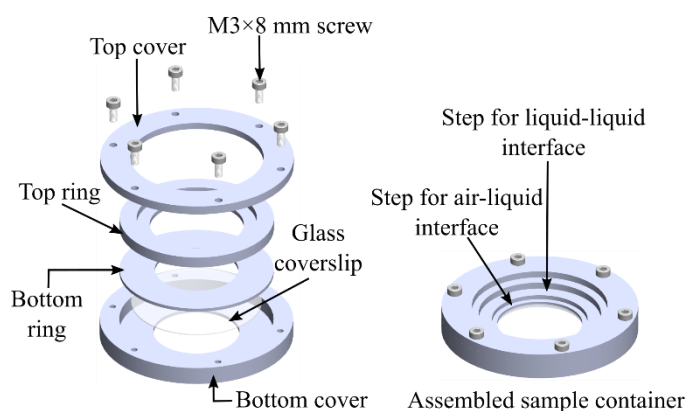


Figure 3.2 Schematic illustrations of the stainless-steel sample container that serves as the sample trough. (Left) Exploded view with all the components of the sample container. Parts are compression fit with M3×8 mm screws. (Right) The assembled view shows the various internal diameters of rings that create pinning points for fluid-fluid interfaces.

The second main component of the radial trough is a custom sample container, shown in Fig. 3.2, that contains the sub-phase and super-phase fluids on a round microscope coverslip with No. 1 thickness and 42 mm diameter (G401-42, ProSciTech, Australia). The sample container is comprised of four annular stainless-steel rings that are held together with M3×8 mm screws. The coverslip is compressed between the bottom cover and bottom ring to form the base of the trough. The steps formed by the presence of the bottom ring and top ring are used to pin either air-liquid or liquid-liquid interfaces. The details of the dimensions for all radial trough parts are

as provided. The second main component of the radial trough is a custom sample container, shown in Fig. 3.2, that contains the sub-phase and super-phase fluids on a round microscope coverslip with No. 1 thickness and 42 mm diameter (G401-42, ProSciTech, Australia). The sample container is comprised of four annular stainless-steel rings that are held together with M3×8 mm screws. The coverslip is compressed between the bottom cover and bottom ring to form the base of the trough. The steps formed by the presence of the bottom ring and top ring are used to pin either air-liquid or liquid-liquid interfaces. The details of the dimensions for all radial trough parts are as provided as SolidWorks 2D drawings in Supporting Material (or Appendix B).

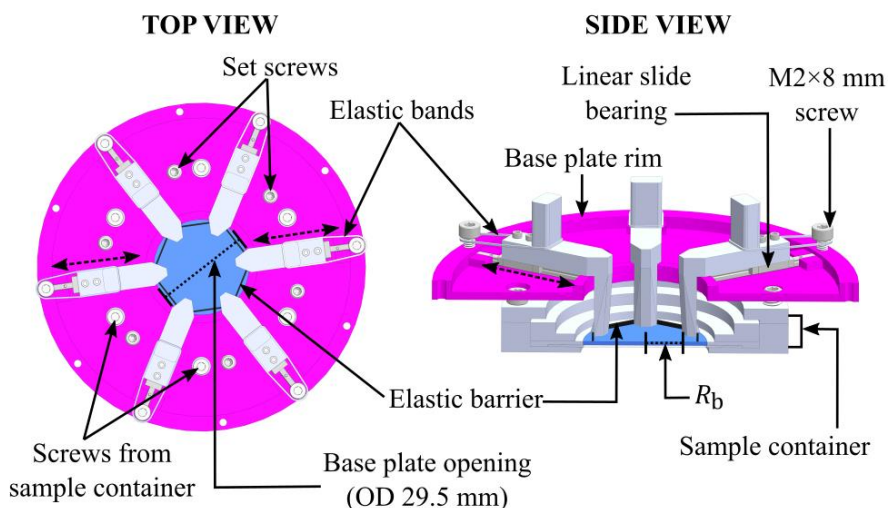


Figure 3.3 Illustrations of the top view (left) and side view (right) of the base plate seated on the sample container with an air-water interface. Top view shows the fully open configuration of the radial trough. Open holes in the base plate that align with the M3×8 mm screws of the sample container fix the position of base plate over the sample chamber and set screws in threaded holes in the base plate allow for height adjustment between the sample container and the base plate. In open configuration, the six fingers and elastic barrier form a hexagonal interfacial area and are held in this default position by using the elastic bands. Each finger is fixed on to a linear slide bearing (see side view). The dashed, double-arrow lines indicate the direction of the movement of the fingers. OD stands for outer diameter.

The compression assembly has holes within the base plate that align with the M3 screws of the samples container to allow the two sections to fit together. This connection between the two assemblies is shown in Fig. 3.3. Set screws (5 mm diameter and 0.5 mm pitch) incorporated into the base plate of the compression assembly allow for fine height adjustment of the compression assembly above the sample container in order to adjust the height of the elastic barrier to the fluid-fluid interface. Each finger is seated on a linear slide bearing that is 2 mm wide and 32 mm long (8381K29, McMaster-Carr, USA). The default position of each finger is maintained in a fully open state (top view of Fig. 3.3) by attaching elastic bands (inner diameter 8 mm, Sonic Dental Supply, USA) between each finger-head and the M2×8 mm screw on the base plate rim. These bands provide a restoring force such that they maintain a smooth expansion of the fingers when the stepper motor enlarges the optical diaphragm. It is noteworthy that these elastic bands are different than the elastic band used as the interfacial barrier that we refer as the elastic barrier. The symmetric, hexagonal arrangement of fingers can produce pure dilatational deformation of a planar fluid-fluid interface. However, not all fingers need to be used to support the elastic barrier, which enables other forms of interfacial deformation to be performed such as non-symmetric (e.g., rectangular) and other symmetric modes (i.e., triangular) of deformation. The stepper-motor has a spatial resolution of $\sim 0.02 \mu\text{m}$, a speed resolution of $\sim 0.015 \mu\text{m/s}$, and a travel length of 25 mm. It is connected to a desktop computer via an X-MCB1 stepper-motor controller (Zaber Technologies, Canada) and is controlled with algorithms written in C++. A constant rate of area deformation was chosen for use in the radial trough and was programmed into the Zaber Console software. This enabled a direct comparison between rectangular and radial Langmuir trough data and accounted for the squared dependence of interfacial area on the linear stepper-motor position, L . Stepper-motor position and radial position of the elastic barrier

have a linear relationship, but area enclosed by the elastic barrier, A , depends on the square of the radius and is approximated as $A = \pi R_b^2$, where R_b is the radius measured from the center of the trough to the edge of the elastic barrier, as indicated in the side view of Fig. 3.3. A calibration was performed to establish the relationship between L and R_b and is provided in Fig. S1a of the Supporting Material (or Fig.B1a of Appendix B). Using $\frac{dA}{dt} = 2\pi R_b \frac{dR_b}{dt} = C$, where C is a constant rate of interfacial area deformation, one can maintain the same value of C for both the radial and rectangular trough. Motor position is recorded during measurements and used to back-calculate radial barrier position and hence the interfacial mean monomer/molecular area.

3.3 Materials and Methods

3.3.1 Silanization

The PLA fingers and the elastic barrier were silanized (dichlorodimethylsilane, 5% in heptane, Sigma-Aldrich, USA) to achieve a water contact angle approaching 90°. Finger-tips were silanized by immersion in silanization solution in an open container for approximately 2 hours. The fingers were then washed thoroughly with ultra-pure water having a resistivity of 18.2 M Ω ·cm obtained from a PURELAB Ultra Analytical purification unit (ELGA LabWater, UK). The fingers were then kept immersed in ultra-pure water for at least 12 hours. The elastic barrier was first washed with ultra-pure water, dried, and then immersed in silanization solution for 15 minutes. Subsequently, it was removed from the solution and left to dry for 2 hours. The band was washed with ethanol and ultra-pure water before use. A new elastic band was used as the barrier for every interface. All the results produced in this work are performed with the silanized radial trough system, unless and otherwise stated.

3.3.2 Sample Preparation

Poly(*tert*-butyl methacrylate) (PtBMA) with average molecular weight of 170 kDa was obtained from Sigma-Aldrich in crystalline solid form and used as received. A stock solution of PtBMA in chloroform with 0.22 mg/mL concentration was prepared in HPLC-plus grade chloroform (Sigma-Aldrich, USA). Before each measurement the PtBMA stock solution was bath sonicated at 4 °C for 30 min. Interfaces were prepared via drop-wise addition of the stock solution using either a 10 μ L Hamilton glass syringe (80330, Hamilton Company, USA) for the radial trough or a 50 μ L Hamilton glass syringe (80530, Hamilton Company, USA) for the rectangular trough. Initial surface coverages of 0.75 mg/m² and 0.79 mg/m² were used for rectangular trough and radial trough, respectively. After spreading PtBMA the interface was left to rest for 45 min for solvent evaporation.

Racemic dipalmitoylphosphatidylcholine (DPPC) in chloroform at 25 mg/mL (Avanti Polar Lipids Inc., USA) was diluted to 0.2 mg/mL with HPLC-plus grade chloroform. The fluorescent dye Texas red, 1,2-dihexadecanoyl-*sn*-glycero-3-phosphoethanolamine (TR-DHPE) (Invitrogen, USA) was added to the diluted DPPC solution at a concentration of 0.1 wt. % dye. The solution was stored in the freezer until use and was mixed thoroughly using a vortex mixer (Maxi Mix II, Thermolyne, USA) for 30 s before use. The spreading method was the same as described above for PtBMA. Initial surface coverage of \sim 1 mg/m² was used for both radial and rectangular Langmuir troughs, and the interface was left to rest for at least 30 min for solvent evaporation. Measurements for both PtBMA and DPPC were performed at 21 °C.

3.3.3 Interface Preparation

The sample container was filled with ultra-pure water with a resistivity of 18.2 M Ω ·cm obtained using a PURELAB Ultra Analytical purification unit (ELGA LabWater, UK). The

compression assembly with a clean elastic barrier was then placed on top such that the elastic barrier touched the air-water interface. The set screws were then adjusted to locate the air-water interface at approximately the mid-point of the elastic barrier. For microscopy images, the entire setup sat on the microscope stage, while a Wilhelmy balance equipped with a Wilhelmy rod was used to obtain surface pressure measurements. Both types of measurements were made independently. The surface tension of the clean air-water interface was measured before each experiment to confirm that contamination of the interface did not occur during preparation. For surface pressure measurements, the Wilhelmy rod was placed at the interface prior to spreading PtBMA or DPPC. All surfaces in contact with the air-water interface were silanized to obtain a contact angle of nearly 90° and therefore the air-water interface was assumed to be flat. Initial surface coverage of the sample was calculated using the interfacial area of the open trough configuration. This area was estimated from the radius and geometry of the elastic barrier with a correction made for the area occupied by the finger-tips that were in contact with the interface and the Wilhelmy rod (if present). Details for this area calculation are provided in the Supporting Material (Appendix B).

3.3.4 Surface Tension Measurement

A ribbon Langmuir trough, model KN 2005 (Biolin Scientific, Finland) with a width of 67.7 mm was used for rectangular trough experiments. Surface tension in the rectangular Langmuir trough was measured with a platinum Wilhelmy plate with a perimeter of 39.4 mm attached to a Wilhelmy balance (Biolin Scientific, Finland). Data was collected at 1 Hz. The recorded data includes the surface pressure, barrier position, and the trough area as function of time. Pure water or clean interface surface pressure was below 0.5 mN/m for the entire compression expansion cycle.

Surface pressure measurements in the radial Langmuir trough were made with the same Wilhelmy balance used for the rectangular Langmuir trough, but instead a platinum Wilhelmy rod (wetted perimeter of 3.2 mm) was used to maintain symmetry during compression. Surface tension data was recorded in KSV NIMA software independently of trough position data recorded in Zaber Console software. Both the KSV NIMA and Zaber Console softwares record CPU time, and this time stamp was used to correlate both data sets in post processing.

In both the rectangular and radial Langmuir troughs constant rate of change of interfacial area was maintained and was kept at $3.4 \text{ mm}^2/\text{s}$. This corresponds to a 1.5 mm/min barrier speed (one sided) in the rectangular Langmuir trough, and a variable barrier speed (2.4 mm/min and 4.4 mm/min) in the radial Langmuir trough. For the surface tension and visualization measurements, both the interfacial materials were compressed to 77.4% of the initial interfacial area.

3.3.5 Sample Visualization

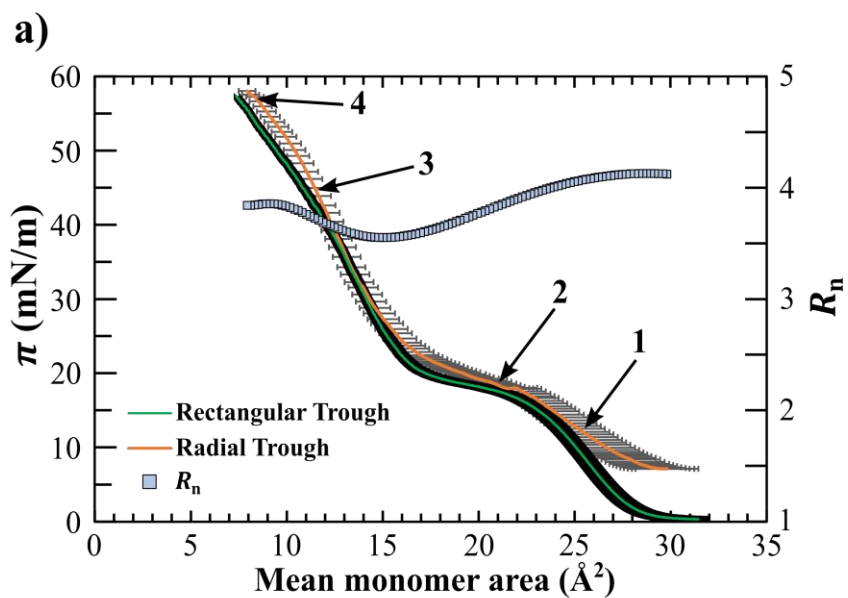
The radial trough assembly was arranged on an inverted microscope stage for microscopy. The inverted fluorescence microscope (Nikon Ti-U) was equipped with an ORCA-Flash 4.0 V3 CMOS camera and a filter cube turret that included a C-FL Texas Red cube. The objectives used in this study included a CFI60 Plan Fluor Phase Contrast DLL 10× Lens (Numerical aperture (NA) 0.3, working distance (WD) 0.16 mm) and a CFI60 Plan Apochromat 40× Water Dipping Lens (NA 0.8, WD 3.5 mm). NIS elements software was used for image acquisition and post-processing. PtBMA interfaces were imaged with Phase Contrast microscopy using the 10× objective and DPPC was visualized with epifluorescence microscopy using the 40× objective. Real time images were captured during interfacial compression by programming the stepper-motor to pause at specified locations or at the desired mean monomer/molecular area for up to 1 min. All images were taken approximately at the central region of the trough.

3.4 Results and Discussions

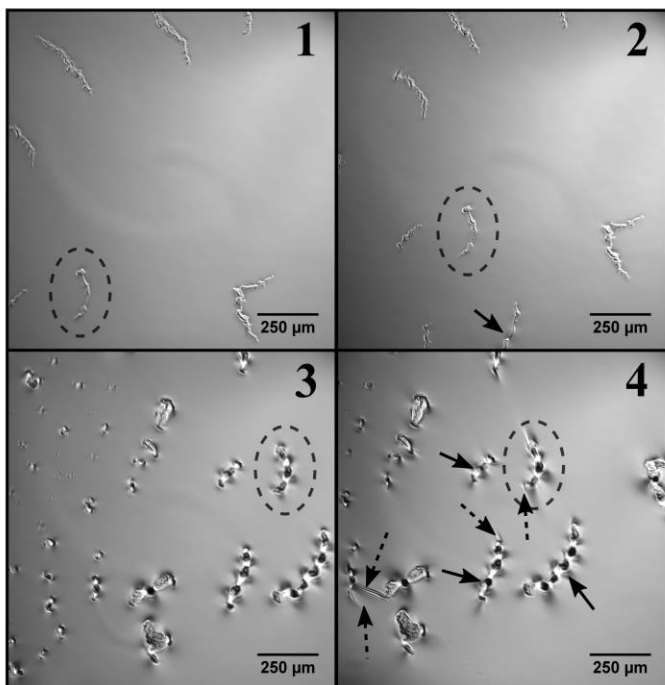
3.4.1 PtBMA at Air-Water Interface

The radial trough was used to make compression-expansion measurements of PtBMA at an air-water interface and to visualize PtBMA films with phase contrast microscopy. Fig. 3.4a shows the surface pressure (π) of PtBMA as a function of the mean monomer area at an air-water interface obtained with a commercial rectangular Langmuir trough and with our radial Langmuir trough. The green data set in Fig. 3.4a is the first compression cycle of PtBMA measured in the rectangular Langmuir trough. Black error bars represent 1.8% uncertainty in the calculated mean monomer area for rectangular trough data and is based on error propagation in estimating trough area, sample concentration, and volume of sample deposited. This measurement is in good agreement with other studies [61, 154]. The orange data set was obtained with the radial Langmuir trough using the same PtBMA stock sample and with similar initial surface coverage. Error bars for the radial trough data (grey) are larger than for the rectangular Langmuir trough and represent 5.5% uncertainty in the calculated mean monomer area. This is a consequence of the increase in uncertainty associated with spreading small sample volumes to prepare the interface for radial Langmuir trough measurements. The error propagation used to obtain these uncertainties is included in the Supporting Material (Appendix B). The secondary y-axis represents the values for normalized capillary radius (R_n) as a function of mean monomer area of PtBMA. The utility of the R_n value is explained later in the last part of the results and discussion section. In Fig. 3.4b, images 1, 2, 3 and 4 of PtBMA at an air-water interface correspond to the mean monomer area labeled on the radial trough curve in Fig. 3.4a with the same notations.

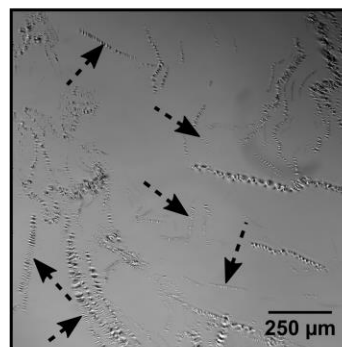
Figure. 3.4 a) Surface pressure (π) as a function of mean monomer area for PtBMA at air-water interface is plotted on the primary y-axis. Both the radial trough measurements (orange line) and rectangular trough measurements (green line) are the initial compression cycle. The grey error bars (radial trough data) and black error bars (rectangular trough data) indicate the uncertainty in calculating mean monomer area. Filled squares are plotted against the secondary y-axis are the normalized capillary radius (R_n) as a function of mean monomer area. b) Micrographs for PtBMA at an air-water interface taken independently during first compression cycle in the radial trough using phase contrast microscopy. Images 1, 2, 3 and 4 are captured at corresponding mean monomer areas indicated as in a). The dashed ovals indicate a common reference point in each image. Solid and dotted arrows indicate wrinkling formed during interfacial compression. Solid arrows point towards larger wrinkling period while the dotted arrows point towards smaller wrinkling period. Scale bars represent 250 μm . c) Micrograph of the same PtBMA interface taken at the full compression point 4 (see part a, interfacial area $\sim 120.2 \text{ mm}^2$) but at a different location of the interface. Dotted arrows show the small wrinkling periods that are used to average the low wavelength (λ_{low}) value.



b)



c)



Both compression curves in Fig. 3.4a agree well and show known characteristics of PtBMA at an air-water interface. The appearance of a plateau region at $\pi \sim 18$ mN/m (and the corresponding mean monomer area at ~ 23 Å²) is consistent with past studies and is indicative of beginning of the structural and rheological transitions [61, 154]. However, we observe some deviation between the two compression curves at larger and smaller mean monomer areas. We attribute the discrepancy in the data at larger mean monomer area (~ 27 Å² to ~ 30 Å²) to localized spreading effects that are different in the radial and rectangular troughs specifically due to the small area available for spreading within the radial trough. Spreading a small sample volume within a small surface area is more likely to manifest as an interface with heterogeneous surface coverage. We believe that initially heterogeneous surface coverage in the radial Langmuir trough gives rise to the high π values (~ 7.5 mN/m) observed at large areas per monomer in the first compression. We regularly observe this behavior in independently prepared interfaces in the radial Langmuir trough. A similar finding with true dilatational deformations in the form of surface pressure noise in the beginning of first compression curve was reported by Miyano and Maeda [140]. They observed this repeatedly with newly prepared interfaces and attributed this behavior to the island formation during initial sample spreading. Depositing a dilute sample at the interface can mitigate heterogenous spreading effects and thus possibly subside the apparent rise in π . To evaluate this, we performed surface pressure measurements with ten times dilute PtBMA sample (0.02 mg/mL) than what was being used to produce results in Fig. 3.4. Considering the large sample volume of the dilute sample, it was spread in the absence of the elastic barrier and the Wilhelmy probe. The results show that in the first compression curve obtained with dilute PtBMA sample π does not show an apparent rise at low mean monomer areas (data shown in Fig. S2 of Supporting Material or Fig. B2 of Appendix B)

thus supporting the idea that the rise observed previously can be an artifact of spreading effects. Another deviation observed between rectangular and radial trough measurements is at smaller mean monomer areas ($\sim 8 \text{ \AA}^2$ to $\sim 10 \text{ \AA}^2$). This deviation is rather expected and is most probably because of the deviatoric or shear stresses that exists in the rectangular trough deformations, as compared to the radial trough device that induces purely dilatational deformations. This phenomena is described in detail by Pepicelli et al. [61]. Thus, the surface pressure measurement shows that the newly built radial Langmuir trough can isolate true dilatational response. The two data sets are in good agreement and capture characteristic features of PtBMA at an air-water interface.

The radial Langmuir trough is designed to operate on the stage of an inverted optical microscope and was used to observe PtBMA at an air-water interface with phase contrast microscopy. Unlike atomic force microscopy (AFM), which requires interfacial material be deposited on a solid substrate, phase contrast microscopy can be used to observe out-of-plane undulations and thickness variations on the scale of the wavelength of the incident light in real time. All the images in Fig. 3.4b were taken at the center of the trough and recorded for the first compression cycle. The PtBMA polymer layer appears to uniformly cover the entire interfacial area. However, there are occasional structures that appear to be thicker than the background PtBMA film that are visible in all of the images in Fig. 3.4b. In image 1 of Fig. 3.4b, one of these structures is indicated with a black-dashed oval and subsequently tracked in images 2, 3 and 4 of Fig. 3.4b. These structures are locally thick areas of PtBMA that resulted from the chaotic nature of sample spreading. Out-of-plane undulations around these structures began to appear at the beginning of the plateau region (shown by black arrow in image 2 of Fig. 3.4b), which indicated the film began to buckle. Further compression from point 2 to 3 led to additional buckling and an

increase in amplitude of the undulations. It is notable that the period of these undulations did not change when the interface was fully compressed. During compression from points 3 to 4, wrinkles originating in the surrounding PtBMA film appeared that were approximately one order of magnitude smaller in period. Wrinkles were observed to relax upon expansion of the interface and the overall film structure appeared to be reversible (see video V1 in the Supporting Material). We observe that there is no preferential orientation of the wrinkles formed (see wrinkles pointed with dotted arrows in Fig. 3.4c). This illustrates that on an average, the interface undergoes isotropic compression as a consequence of the radial trough generating dilatational deformations. The visualization thus complements the dilatational deformations made in the radial Langmuir trough.

There have been few attempts to visualize PtBMA monolayers in situ. An effort was made by Gavranovic et al. [154], where they acquired PtBMA monolayer images using BAM. Although Gavranovic and coworkers demonstrated they could capture interface roughness for $\pi > 25$ mN/m (i.e., after the PtBMA π - A curve undergoes plateau formation) in their images, they could not specifically define or relate the structural artifacts to understand the mechanical properties of the film. In this work, we successfully show how the undulations observed in the interfacial film are related directly to the film's mechanical or rheological properties. The plateau region in our system ends at ~ 15 Å²/monomer and wrinkling of the film was widely observed as the mean monomer area was further reduced. This was expected as PtBMA is known to behave elastically during compression beyond this point [61, 154]. The period of wrinkling can be used to directly estimate an effective Young's modulus (E) for a film of known thickness. We follow the work of Imperiali and co-workers [161], who used observations of periodic wrinkling of tiled graphene oxide sheets upon unidirectional compression to estimate the film modulus from

classical elasticity theory. This theory states that an elastic film wrinkles upon compression in order to release part of its energy into bending and the corresponding wrinkling period is proportional to the Young's modulus. Following Imperiali et al. [161] we calculated the bending stiffness (B), $B = \Delta\rho g \lambda^4 / 16\pi^4$. Here, $\Delta\rho$ is the density difference between the sub-phase and super-phase fluids of the system (i.e., air and water), g is the gravitational constant, and λ is the wavelength of the periodic wrinkles. This value of B can then be used to evaluate an effective Young's modulus, $E = 12B(1 - \nu^2)/d^3$, where d is the film thickness and ν is the Poisson ratio. In image 4 of Fig. 3.4b, we observed two distinct orders of magnitude for wrinkling periods or wavelengths. We quantify these as high wavelengths (λ_{high} , solid arrows), and low wavelengths (λ_{low} , dotted arrows). By performing image analysis using the length measurement tool in NIS elements software and taking an average of the observed wrinkling period lengths, we get, $\lambda_{\text{high}} = 59.5 \pm 15.8 \mu\text{m}$ and $\lambda_{\text{low}} = 9.6 \pm 3.7 \mu\text{m}$. The reported errors represent one standard deviation. There were few locations to measure λ_{low} within image 4 of Fig. 3.4b, which required us to analyze another image from the same film at the same mean monomer area but at a location away from the central region. This image is provided in Fig. 3.4c where the low wavelength wrinkles are pointed with dotted arrows. The calculations demonstrate λ_{high} is an order of magnitude greater than λ_{low} , and each of these values will result in a specific E value when evaluated. Thus, two different values of Young's modulus for the same film indicates the presence of local variations in the film thickness, d . This information allowed us to quantitatively determine the local film thickness for a given value of the wavelength. The dashed black encircled structure and other similar structures seen in the images in Fig. 3.4b are regions of greater thickness that are a result of spreading heterogeneity. We measured λ_{high} around these structures and thus associate this value with the heterogenous part of the film. Similarly, the

homogenous part of the film is associated with the smaller wavelength, λ_{low} and we assume it provides the true effective Young's modulus, E_{low} .

The average λ_{low} gives a B_{low} value of 5.3×10^{-20} J. The homogenous film thickness required for the B_{low} calculation was approximated based on the surface coverage when the film was compressed to a monomer area of 15 \AA^2 and was 1.5 nm. Next, taking $\nu = 0.5$ for an isotropic material, we get E_{low} as 1.4×10^8 Pa. This bulk effective Young's modulus can be expressed as the surface Young's modulus (E_s) by multiplying it by monolayer thickness, d_{mono} ($E_s = E d_{\text{mono}}$). We can estimate the monolayer thickness in a similar manner like the previously calculated thickness, but here we require a non-compressed layer thickness and thus we rely on the theoretical monolayer film thickness, $d_{\text{mono}} = 1.03$ nm [162], which yields a value of $E_s \sim 150$ mN/m. Further, this surface Young's modulus value can be compared with the surface compressional modulus, K , that can be independently calculated from a compression-expansion measurement for a thin film, using the formula, $K = -A \frac{d\pi}{dA}$ [161]. For a PtBMA film at $15 \text{ \AA}^2/\text{monomer}$, $K \sim 123$ mN/m, which is in good agreement with E_s . Lastly, we quantitatively predicted the film thickness of the heterogeneous portion of the film based on λ_{high} and the true Young's modulus value, E_{low} , yielding a local thickness $d_{\text{high}} \sim 17$ nm. This value is an order of magnitude greater than the surrounding homogenous film thickness. These measurements illustrate the power of combining visualization with interfacial deformation where imaging can be used to directly extract the local structural and mechanical properties of interfacial films.

3.4.2 DPPC at Air-Water Interface

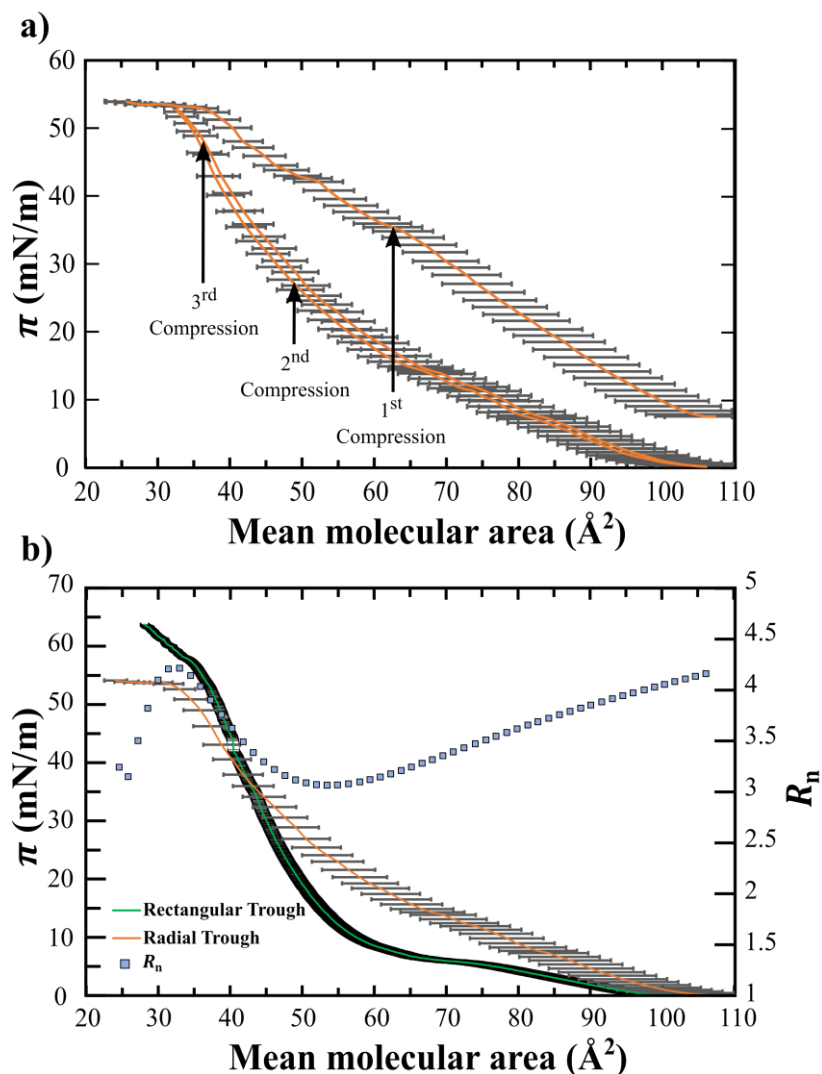


Figure 3.5 a) Surface pressure (π) as a function of mean molecular area for DPPC at an air-water interface. Three consecutive continuous compressions (orange line) measured using the radial Langmuir trough are shown. The grey error bars indicate the uncertainty in estimating the mean molecular area. b) The green line indicates DPPC surface pressure measured using the rectangular Langmuir trough, while the orange line is the same second compression curve that is plotted in a). Black error bars on rectangular trough data set represent the uncertainty in estimating mean molecular area of DPPC. The secondary y-axis data (solid blue squares) is the measured normalized capillary radius (R_n) as a function of mean molecular area.

Fig. 3.5a shows three consecutive compression curves of DPPC obtained from the radial Langmuir trough. The primary y-axis in Fig. 3.5b shows the first compression curve of DPPC at

an air-water interface measured with a rectangular Langmuir trough (green line) along with the second compression curve of DPPC at the same air-water interface shown in Fig. 3.5a (orange line). The data set obtained from the rectangular Langmuir trough agrees well with the literature [66, 98, 155, 160, 163-165]. Both data sets were obtained with the same stock sample to maintain consistency in the experiments. The black error bars (rectangular trough data) and grey error bars (radial trough data) indicate the uncertainty in estimating the mean molecular area of DPPC. The calculated percentage error in radial trough data set (6.5%) is higher than the rectangular trough (1.8%) owing to the small sample volumes spread within the radial trough, as explained previously with the PtBMA measurement. The data set on the secondary y-axis in Fig. 3.5b is the normalized capillary radius (R_n) value and is discussed later.

The first compression curve of DPPC in Fig. 3.5a, begins with an apparently high surface pressure and interestingly, it continues to increase unusually high than what is typically expected from a rectangular trough measurement (Fig. 3.5b). This gives rise to a strong hysteresis between the first and second compression curves of DPPC (Fig. 3.5a) that is unique than the typically observed hysteresis of compression-expansion curves. We repeatedly observed these two results i.e., apparently high surface pressure near the high mean molecular areas of first compression and the compression-compression hysteresis in our radial trough measurements (see independent measurement in Fig. S3 of Supporting Material or Fig. B3 of Appendix B). Although similar observations have been reported for DPPC interfaces, but they occur in the presence of excessive solvent vapor in the gas phase of the interface [166] and this has not been our experimental condition. Higher temperature (37 °C) can also result in higher π values of DPPC [167, 168] but the measurements reported in this work were performed at room temperature. Other factors like adsorption of DPPC on the Wilhelmy probe or barrier surfaces (fingers and elastic band) can also

contribute to the observations seen in Fig. 3.5a. However, we can discard the possibility of adsorption of DPPC on the Wilhelmy probe as a source of this phenomena since in both troughs the Wilhelmy probe is made up of platinum, and these behaviors are only observed in the radial trough. Although adsorption of DPPC onto the barrier surfaces is possible, it would result in loss of interfacial material. This loss of material would further result in a reduction of the maximum π achieved during subsequent compressions, but this is not the case. In our case, we attribute the observations made in Fig. 3.5a to localized spreading effects or spreading heterogeneity that can occur in the radial trough because of spreading small sample volumes in a relatively small trough area. Our working hypothesis for spreading heterogeneity is that in a small trough, material spread from a solvent may deposit unevenly around surfaces such as the Wilhelmy rod that interact with the spreading capillary wave. The contact between the surface and the spreading wave may slow the solvent spread and lead to locally high concentrations of interfacial material causing an unexpectedly large π . Depositing dilute DPPC sample in absence of Wilhelmy rod and the barrier can alleviate the effects of spreading heterogeneities. This can be seen in Fig. S 4 of Supporting Material (or Fig. B4 of Appendix B) where the apparent rise in π at high mean molecular areas for the first compression is vanished. However, use of dilute sample does not reduce the compression-compression hysteresis and more investigation is needed to understand this phenomenon. Note that, the disappearance of the apparent rise in π during the consecutive compressions (see near high mean molecular areas in Fig. 3.5a and Fig. S4) can further support our assertion that this behavior is related to the localized spreading effects. In Fig. 3.5a, the π values in subsequent compressions of DPPC reduces, and also the compression-compression hysteresis between the second and third compression curves is much less than the hysteresis between the first and second compressions. A potential explanation of this behavior is that

during the first compression-expansion cycle the compressing of the monolayer allows self-association and/or rearrangement of the DPPC molecules [165, 169] and later, homogenous re-distribution occurs during expansion. After the first expansion, subsequent compression and expansion curves are more reproducible, with less hysteresis (see Fig. S5 in Supporting Material or Fig. B5 of Appendix B). This overall behavior is reproducible and is observed repeatedly in independently prepared DPPC interfaces (see Fig. S3 in Supporting Material or Fig. B3 of Appendix B).

Fig. 3.5b, we observe significant deviation in the compression curves obtained from radial and rectangular trough, especially near the liquid-condensed/liquid-expanded (LC/LE) phase co-existence (or transition) region which is marked by a definite plateau in the rectangular trough (green line) data ($\pi \sim 6$ to 8 mN/m). For the radial trough data, instead of a plateau, we observe a steady increase in the slope of the compression curve. Similar changes in the shape near the transition region of DPPC obtained using a purely dilatational pendant drop method and rectangular trough method was reported by Li et al. [170]. A lack of a plateau in the compression curve is commonly observed in droplet based methods [171-175], and can often be attributed to experimental conditions like the presence of impurities [170, 173], material deposition methods [172] or curved or bent interfaces [170, 173]. Under certain conditions rectangular troughs that perform planar deformations can also show a slope or shoulder in the phase co-existence region. For the radial trough measurements shown in Fig. 3.5b we predict that the increasing slope is possibly a result of combination of the effects mentioned above. The DPPC sample used in our experiments is doped with TR-DHPE fluorescent dye for imaging purposes and can be considered as an impurity. TR-DHPE or other fluorescent dyes are known to bind with DPPC molecules, and this affects their phase behavior and dynamics [176, 177]. Impurities can have a

more pronounced effect on the surface pressure in a small area trough like the radial trough used here than in a typically large trough like rectangular trough [173]. Next, Jyoti et al. showed that the shape of the DPPC surface pressure is also affected by the deposition method. They observed that penetration of the syringe into the bulk phase during deposition can affect the amount of lipid in the bulk phase causing a change in the shape of the phase co-existence region. The other parameter that can result in increased surface pressure near phase co-existence region is the interfacial curvature. With curved interfaces like droplet or bubble, the lipid domains can grow away from equilibrium and thus lead to an increase in measured surface pressure [170, 173]. Although the radial trough is designed to have a planar interface, the use of a Wilhelmy rod for surface pressure measurement introduces considerable interfacial curvature due to capillary deformation, which may influence the measured surface pressure. In order to quantitatively understand this, we define a normalized capillary radius, $R_n = \frac{R_f}{C_L}$, which is a ratio of a trough length scale, R_f , to the capillary length scale, C_L . The R_n value for these DPPC measurements is displayed on the secondary y-axis of Fig. 3.5b. The detailed explanation of how the R_n value is calculated and interpreted is provided in the next section. For $R_n < 4$ the interface has significant curvature such that an artificial increase in the surface pressure is observed, while for $R_n \geq 4$ curvatures of the interface have little effect on the surface pressure. In Fig. 3.5b, R_n drops significantly near the mean molecular areas corresponding to the phase co-existence region, likely contributing to the apparent increase in π where a plateau region is expected. Past studies could qualitatively predict the influence of curvature on measured surface pressure [170, 173], but the miniaturized radial trough can do so quantitatively.

Another difference between the rectangular and radial trough surface pressure measurements can be observed below a mean molecular area of 35 \AA^2 , which is approximately

the minimum area per molecule for a true monolayer of DPPC (see Fig. 3.5b). Here, the rectangular trough data shows a distinct kink in the surface pressure curve indicating an interface collapse point and a possible transition from monolayer to multilayer film. Similar observations of the DPPC film compressed in a rectangular trough have been reported previously [165]. On the other hand, for the radial trough data the surface pressure ceases to increase below this mean molecular area even when the film is compressed. We believe that the DPPC film in the radial trough does not undergo collapse since interface collapse typically is thought to result in irreversible change, such as loss of material into the bulk [178]. In this case we observe repeatable subsequent compression-expansion curves of the DPPC film (see Fig. 3.5a and Fig. S5). Compressing the DPPC film at higher surface coverages results in a solid-like phase where elastic modulus dominates the film properties. The elastic nature of the interface gives rise to strong deviatoric stresses that depend on the kinematics of the deformation and can ultimately affect the measured surface pressure [61]. The two troughs have different deformation fields, likely resulting in the difference between the surface pressures obtained from the two troughs at these high coverages. One could assert that the rectangular trough, which produces both shear and dilatational deformations, leads to collapse in the DPPC film, while the radial trough, with pure dilatational deformations, facilitates further compression of the film without collapse. Note that at high surface coverages R_n values also decrease, but the deviation seen here is more likely because of the kinematics of the deformation as explained above.

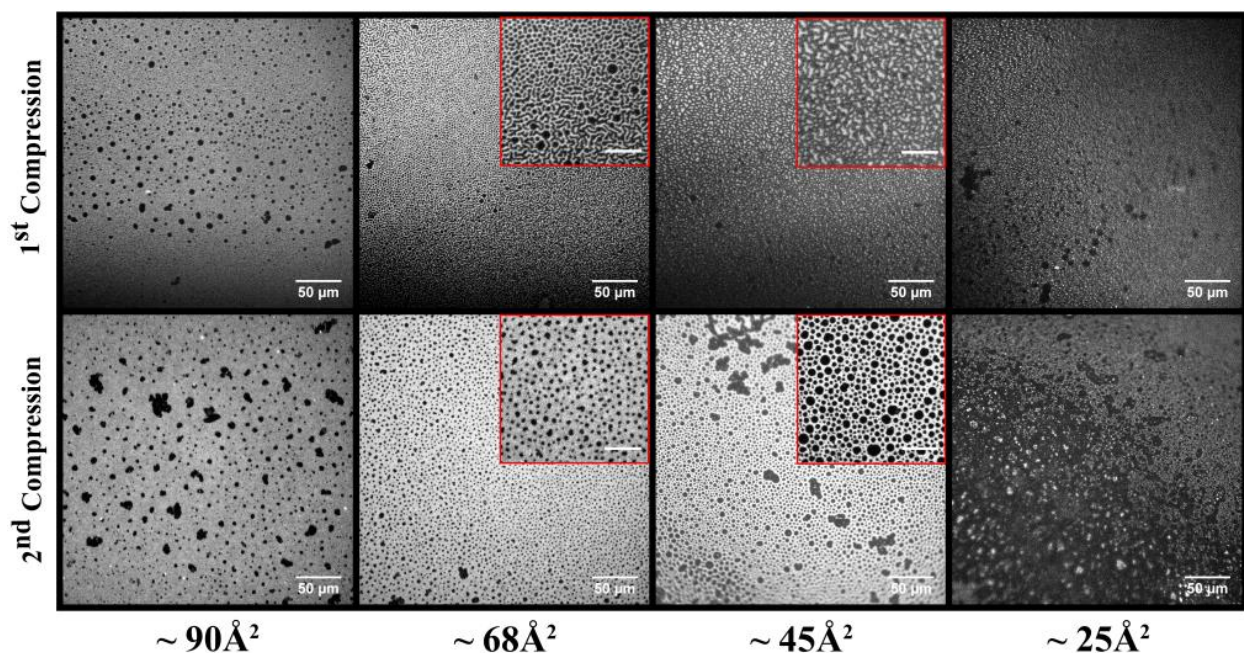


Figure 3.6 Micrographs of DPPC at an air-water interface captured independently using epifluorescence microscopy. The top row contains images acquired during the first compression cycle in the radial Langmuir trough, and the bottom row has images taken during the second (subsequent) compression cycle. Approximate mean molecular area for each image is shown at the bottom such that every column of micrographs is captured at same compression point. Scale bars for main micrographs represent 50 μm . Inset images are digitally magnified regions of the corresponding main micrographs with scale bar representing 20 μm . These inset images are enhanced with higher contrast for improved visibility.

Fig. 3.6 contains micrographs of DPPC at different mean molecular areas at an air-water interface acquired with epifluorescence microscopy for the first (top row) and the second (bottom row) compression curves in the radial Langmuir trough. The initial interfacial coverage of DPPC, the amount of compression area, and the compression speed are maintained like the one used for the results in Fig. 3.5a. Images were acquired at the same molecular area to facilitate comparison of film structure between consecutive compression cycles in the radial Langmuir trough. DPPC-rich domains appear as dark regions where the liquid-condensed (LC) structure excludes the fluorescent dye molecules. Brighter regions indicate an increased presence of the dye and are typically associated with liquid-expanded (LE) regions [179]. Each image was acquired in the central region of the available interfacial area of the trough and at a specific location on the compression curve that is specific to a corresponding mean molecular area for

DPPC. In Fig. 3.6, we observe a morphological difference between the first and second compression curve when compressed beyond $90 \text{ \AA}^2/\text{molecule}$. To the best of our knowledge such a structural difference for consecutive compression curves of DPPC has not been reported previously. When the interface is compressed to $68 \text{ \AA}^2/\text{molecule}$, we observe a complex structure consisting of mesh-like domains of DPPC along with regions of densely packed circular DPPC domains. Upon further compression to LC phase around $45 \text{ \AA}^2/\text{molecule}$, the DPPC morphology grows predominantly into a network, or mesh structure. At $25 \text{ \AA}^2/\text{molecule}$ the interface reaches a dense state with little recognizable structure. The formation of a network structure in the LC phase may be specific to non-chiral racemic DPPC that is used in this work. Studies on morphology of racemic DPPC are rare, and there are discrepancies in the literature regarding the morphology at an air-water interface. In the LC phase, Caminati et al. [180] showed that a racemic DPPC attains fractal or cholesteric structure, which is very different to its chiral counterpart that forms multilobed triskelions at the interface. Vollhardt et al. [181] reported individual straight arm structures, while McConnell et al. [177] and Kim et al. [182] reported simple circular domains for racemic DPPC in the LC phase. Moreover, investigating how the structure of racemic DPPC changes during the course of compression cycles has been missing from these studies and therefore, it is difficult to establish a coherent analysis of our study with these reported studies. Although we predominantly see a network structure of DPPC-rich domains in the first compression curve, the entire second consecutive compression curve only contains isolated circular domains of DPPC that pack more closely as the compression progresses (see bottom row, Fig. 3.6). This drastic change in the structure of DPPC during second compression is likely the result of the molecular level re-arrangement and association of DPPC domains during the first compression. These structural observations are reproducible and can be correlate with the large hysteresis observed in Fig. 3.5a. Although we lack causative evidence to connect the structural differences and the hysteresis between the first and second consecutive compression curves, it is expected that interfacial structure will influence measured surface stresses. A possible explanation for this behavior is that initial spreading of sample results in a non-equilibrium arrangement of DPPC, even at relatively low surface coverages, leading to the network formation observed during the first compression. Compression of the monolayer to high surface coverage during the first compression creates an environment where DPPC molecules can re-structure prior to expansion. Subsequent compressions then result in a

uniform film morphology and repeatable surface pressures. Images acquired during the first and second expansion of the same interface shows a similar structural difference (see Fig. S6 in Supporting Material or Fig. B6 of Appendix B). However, the networking of DPPC domains in the first expansion is much less than in the first compression. This type of loose networking in the first expansion and its disappearance in subsequent expansion was observed by Rodríguez Patino et al. [169] and they attribute it to the memory effects of the double chain hydrocarbons.

3.4.3 Capillary Deformation and Surface Pressure

Capillary deformation is important to consider when performing surface pressure measurements with a Wilhelmy probe. The probe is constructed of platinum to generate a small contact angle ($\sim 0^\circ$) with an aqueous subphase. This low contact angle between the probe and the subphase induces a significant meniscus or interfacial curvature when inserted normal to the interface. This curvature persists over a capillary length scale (C_L) and depends on surface tension, γ , the difference in lower and upper fluid densities, $\Delta\rho$, and gravitational acceleration, g , as

$$C_L = \sqrt{\frac{\gamma}{\Delta\rho g}} \quad (3.1)$$

For a clean air-water interface at 25 °C, $C_L = 2.72$ mm. In a commercial large rectangular Langmuir trough, C_L is generally much smaller than the minimum distance between the Wilhelmy probe and interfacial barriers upon maximum interfacial compression (i.e., minimum available surface area) and a correction to the measured surface pressure due to encroachment upon the C_L can be neglected. However, for small sized troughs like the radial Langmuir trough, C_L can be comparable in magnitude to length scales of the trough.

The weight of the fluid under the meniscus is directly related to surface tension, and thus the shape of the meniscus is critical in accurately measuring surface tension with this method.

Velev and coworkers showed that when the separation distance between two objects in a fluid-fluid interface is near or less than C_L , the menisci interact strongly and experience significant lateral capillary forces [183]. Any nearby interfacial curvature like the curvature from barrier components (e.g., finger-tips or elastic band), can interact with it (see inset of Fig. S7 in the Supporting Material or Fig.B7 of Appendix B) and give deviations in the surface tension measurement. The magnitude of these interactions depends on the three-phase contact angle, θ_0 , of each body interacting at the fluid-fluid interface, and the surface tension, γ . Meniscus contour plots as a function of normalized compression length of the radial trough (see Fig. S7 in the Supporting Material or Fig.B7 of Appendix B) were generated from B.E. Rapp [184], and simply illustrate that theoretically a contact angle at the finger-tip or elastic barrier that is $< 90^\circ$ will generally result in an underestimation of the mass of water measured by the Wilhelmy balance, and thus an artificially large surface pressure. The consequence for trough design is that a 90° finger-tip contact angle is desirable to minimize the influence of capillary deformation, and that when trough dimensions approach C_L , one must check for the influence of such deformations on the measured surface pressure.

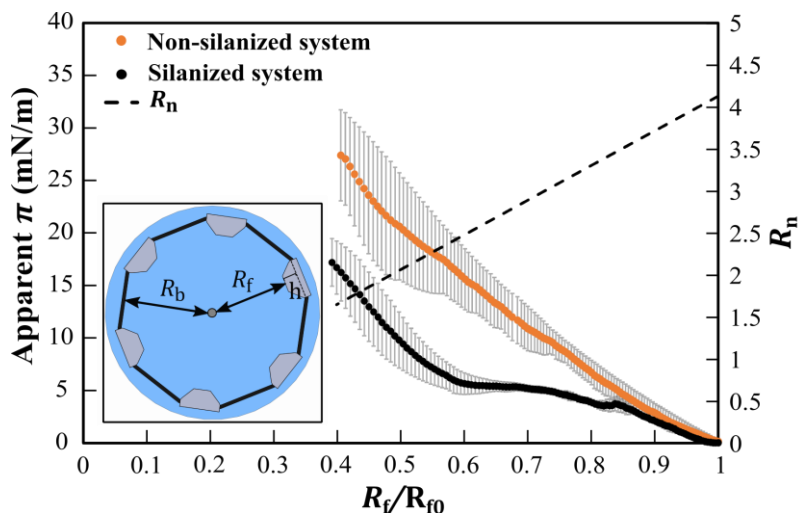


Figure 3.7 Effect of silanization of the elastic barrier and the finger-tips on the apparent surface pressure (π) measurement of a clean air-water interface in the radial Langmuir trough. Apparent π , is plotted as a function of the normalized separation distance between the finger tips and the Wilhelmy rod, R_f/R_{f0} , where R_{f0} is the maximum value of R_f . The inset illustration shows the definition of the measured values of R_f , and R_b . The width of a finger-tip cross section, h , is also indicated. Orange circles represent apparent π for the non-silanized system, while the black circles represent the silanized system. Values for normalized capillary radius (R_n) are shown with the dashed black line and are associated with the secondary y-axis. Error bars represent the maximum and minimum surface pressures measured between the two set of measurements.

The influence of capillary deformation on the measured surface pressure was tested experimentally. Two compression curves obtained in the radial Langmuir trough using a platinum Wilhelmy rod with clean interfaces are shown in Fig. 3.7. In top curve with orange data set the elastic barrier and finger-tips have not been chemically treated ($\theta_0 < 90^\circ$, non-silanized system), and in bottom curve with black circles the elastic barrier and finger-tips have been treated with a silanization solution to obtain a contact angle close to 90° (silanized system). The difference in actual contact angle for pre and post treated surfaces is shown in Fig. S8 of the Supporting Material (Fig. B8 of Appendix B) where the contact angles are estimated using the ImageJ software. The apparent rise in measured π is plotted as a function of normalized radial separation (R_f/R_{f0}). The image in the inset is an illustration of a top view of the barrier, fingers,

and interface and defines different radial length scales of the trough. The maximum radial separation, R_{f0} , is taken to be the distance between the finger-tips and the Wilhelmy rod, i.e., $R_{f0} = R_b - h$. The distance between the finger-tips and the Wilhelmy rod, R_f , changes during a compression-expansion cycle such that $R_f/R_{f0} \leq 1$. The secondary y-axis displays the normalized capillary radius, R_n , defined as $R_n = \frac{R_f}{C_L}$. Both curves indicate non-zero surface pressure values, implying the interaction of capillary curvature between the Wilhelmy rod and the barrier, but the silanization significantly reduces the deviation between measurements. R_n values change during a compression-expansion experiment even at constant surface tension, decreasing linearly with R_f . The important information obtained from Fig. 3.7 is that $R_n \geq 4$ can be expected to introduce least error in the surface pressure, while values of $R_n < 4$ may lead to erroneous non-zero surface pressures. This aligns with the theoretical observation (also recreated in Fig. S7 of Supporting Material or Fig. B7 of Appendix B) that for $R_n \geq 4$ the meniscus flattens and has little to no curvature [184] and therefore there is least influence of capillary deformation on the measured surface pressure. The relative magnitudes of R_n for any given interface, including the PtBMA interface and the DPPC interfaces discussed earlier are indicative of the magnitude of the surface pressure error expected from interfacial curvature. For convenience, we combine the result of the surface pressure measurement of pure water obtained in Fig. 3.7 and surface pressure measurements of PtBMA/DPPC interfaces in Fig. S9 of Supporting Material (or Fig. B9 of Appendix B).

The normalized capillary radius, R_n , is a function of both R_f and C_L , and since C_L can change during a compression-expansion measurement of any interfacially active material the function $C_L = f(\Gamma)$ where Γ is surface concentration, must be known a priori to calculate R_n . We used compression-expansion data from the rectangular Langmuir trough on the PtBMA

(Fig.3.4a) and DPPC (Fig. 3.5a) interfaces to obtain this relationship, from which R_n as a function of area per monomer in the radial Langmuir trough was calculated and plotted in Fig. 3.4a and Fig. 3.5b. In both figures, R_n is plotted on the secondary y-axis. For the PtBMA data in Fig. 3.4a, R_n remains large during the course of a compression, reaching a minimum of approximately 3.5 at 15 \AA^2 before increasing again at smaller areas per monomer. For DPPC data in Fig. 3.5b, R_n drops to a minimum of approximately 3 at 53 \AA^2 . This helps explain the strong agreement between the radial Langmuir trough and the rectangular Langmuir trough data for the entire PtBMA compression curves, and also why a plateau region in the DPPC data is effectively missing in the radial Langmuir trough data. For both these data sets we observe deviations in the surface pressure measured with radial and rectangular trough at low and high surface coverages even when R_n is close to 4. The discrepancy at lower coverages is attributed to the localized spreading effects while that at high coverages is a consequence of deviatoric stresses present in rectangular trough. Thus, capillary deformation is not the primary cause of these deviations. Detailed description is provided in the discussion part of Fig.3.4a and Fig.3.5b. It is worth noting that alternatives to Wilhelmy probes for surface pressure measurements, such as the microtensiometers developed by Zell et al. [185], or a wire loop tensiometer [186], should be much less influenced by capillary curvature. Such tensiometers sit flat on an interface and do not rely on meniscus formation in order to make a surface pressure measurement. The millimeter scale of these tensiometers may also allow for simultaneous surface pressure measurements and microscopy observations in future work.

3.5 Conclusions

In situ evaluations of planar interfacial morphology and rheology of complex fluid-fluid interfaces have been performed with Langmuir trough devices [66, 187] that either induce mixed

deformation fields, or purely shear deformations [109, 120, 122]. Experimental techniques that create pure dilatational deformations with simultaneous imaging are lacking, and as a consequence the experimental ability to test complex constitutive relationships is limited. To overcome this, we have developed a compact radial Langmuir trough that is capable of performing simultaneous imaging and dilatational deformation of a complex fluid-fluid interface. This compact radial trough design works in tandem with a typical inverted microscope. Two different interfacial systems were explored: PtBMA and DPPC at air-water interfaces. Surface pressure of these interfaces was measured using Wilhelmy probes while the microscopy imaging was performed on an inverted microscope. We found excellent agreement between the radial and rectangular Langmuir trough surface pressure measurements for PtBMA films, thus validating the functionality of our trough design. Additionally, the isotherm behavior observed here compares well with previous studies found in literature [61, 154]. We demonstrated the use of PtBMA micrographs to extract interfacial mechanical properties from real time images of film structure, and to quantitatively determine variations in local film thickness. This analysis is an improvement to the study performed by Gavranovic et al. [154], where they visualized PtBMA film at an air-water interface using a BAM setup, but did not use this information for analyzing the film's mechanical properties. This work is one of the first attempts to directly visualize planar polymer thin films under purely dilatational deformations and simultaneously characterize their properties using the structural information obtained from micrographs. Surface pressure measurements of DPPC at an air-water interfaces obtained from the radial Langmuir trough showed significant deviation than the one obtained from rectangular trough, especially in the phase co-existence or transition region. The surface pressure measured with radial trough showed a lack of a plateau region. This behavior has been reported in the past [170, 171, 173,

175] but the quantitative analysis of the reasons behind it have been lacking. We show with capillary length scale arguments that interfacial curvature introduced by the use of the Wilhelmy rod may contribute to this behavior. In general, surface pressure measurements obtained with a Wilhelmy probe in a small trough must be interpreted carefully. For DPPC we observed a correlation between a large hysteresis from the first to the second compression-expansion cycles and the structure as observed in microscopy. The structural differences clearly correlate with the hysteresis, but establishing a causative relationship requires further analysis.

This work reveals that simultaneous dilatational deformation and interfacial visualization can facilitate understanding of structure-property relationships and interfacial dynamics. This kind of in-situ morphological investigation is very relevant to a variety of different processes in the field of colloid and interfacial science such as 2D crystallization and self-assembly of colloidal particles [107, 119, 187-189], and self-assembly of biological membranes and proteins at interfaces [101]. This equipment and the techniques described here are intended to broaden access to simultaneous dilatational-visualization measurements of fluid-fluid interfaces that will advance understanding of structure-property relationships at interfaces, and aid in the development of more complex constitutive equations to describe experimentally observed interfacial rheological behavior. Future efforts will also seek to experimentally test interfacial constitutive relationships that decouple shear and dilatational components while also incorporating non-Newtonian behaviors that are consistent with the interfacial structures observed in microscopy.

CHAPTER 4

OSCILLATORY DILATATIONAL DEFORMATIONS OF FLUID-FLUID INTERFACES USING RADIAL LANGMUIR TROUGH

Unpublished work

Shalaka K. Kale¹, and Joseph R. Samaniuk²

Chapter 3 discusses development of the miniaturized radial Langmuir trough device that can be used to perform true dilatational deformations of fluid-fluid interfaces. The dilatational strain or deformations can be applied in the form of steady area changes or oscillatory area changes. Chapter 3 particularly focuses on applying the constant rate of change of area deformations at interfaces. Such deformations play a role in determining surface pressure-area isotherms and understanding phenomena like the relaxation dynamics of interfaces. On the other hand, oscillatory area deformations can be employed to extract the complex viscoelastic moduli of an interface. Dilatational viscoelastic properties can provide vital insights for understanding functionality, stability, and adsorption dynamics of various fluid-fluid interfaces. This chapter demonstrates a methodology to implement oscillatory area strains in the custom-built radial Langmuir trough device. The novelty of the radial Langmuir trough device is that it can perform interfacial visualization during deformations. Therefore, it can correlate the structure-property relationship of an interface. In this chapter, we investigate viscoelastic properties of a model

¹ Primary Author and Graduate researcher, Department of Chemical and Biological Engineering, Colorado School of Mines, Golden, CO.

² Graduate Advisor and Author for correspondence, Department of Chemical and Biological Engineering, Colorado School of Mines, Golden, CO.

phospholipid lung surfactant present at air-water interface and try to understand the if the microstructure can be related to the rheological behavior.

4.1 Introduction

Fluid-fluid interfaces are inherently present in many natural and synthetic processes. Dilatational rheology comes into play when the interfacial mechanical behavior is affected by the change in size of the interfacial area. Characterizing the dilatational viscoelastic properties of fluid-fluid interfaces is important because it can aid in understanding phenomena like stability of foams and emulsions [115, 190-192], adsorption mechanisms of polymer/surfactant or particle laden interfaces [112, 124, 193] or aggregation tendency of proteins at interfaces [132, 194, 195].

Phospholipids are amphiphilic molecules that are prevalent in all living organisms, and they naturally occur as a component of cell membranes. Due to their excellent biocompatibility, phospholipids have found wide-ranging applications in drug delivery formulations that includes systems like liposomes, emulsions, and wetting agents [196-198]. Phospholipids are also becoming popular in cosmetic [199] and food formulations [200] due to the increasing demand for natural and safe emulsifiers. Understanding the rheological behavior of phospholipids at fluid-fluid interfaces in such systems can be a crucial step in making viable and stable formulations. Phospholipids are also found in mammalian lung surfactant mixture. Their role is to reduce the surface tension of air-water interface at alveolar lining of the lungs and consequently this facilitates the breathing process [156, 201]. In the event of premature infant birth, the natural lung surfactants are not fully developed and this may cause respiratory distress syndrome [202, 203], and in such cases artificial lung surfactants are introduced for regulating the breathing process. The study of the factors like spreading behavior and stability of the surfactant film are important in developing effective artificial lung surfactants, and this can be

achieved with the help of dilatational interfacial measurements. These widespread applications of phospholipids at fluid-fluid interfaces have been the motivation for many research studies. One of the commonly found and extensively investigated phospholipids is dipalmitoylphosphatidylcholine (DPPC) [204]. The interfacial rheological properties of DPPC are well characterized in literature. In this work, we have chosen DPPC as a model phospholipid and we investigate the dilatational viscoelastic properties of DPPC at air-water interface using the custom-built radial Langmuir trough [205].

During the dilatational deformation (or strain) of an interface, the interface is deformed in a manner such that the shape remains constant but the interfacial area changes. This is unlike the interfacial shear deformations, where the applied strain changes the shape of the interface while maintaining a constant area. Examples from the literature mentioned in the previous paragraph showed the need to study the dilatational interfacial properties. In this work demonstrate the application of oscillatory dilatational deformations to complex fluid-fluid interface. Last few decades have seen the growth of techniques that can apply interfacial dilatational deformations, and these include Langmuir-Pockels troughs with Wilhelmy balance and pendant drop tensiometers and its variations. However, the major limitation with these conventional methods is that they can introduce mixed deformations fields (both shear and dilatational strains) [61] and therefore, it is difficult to separate the individual contributions of the deformations that relate to the interfacial properties. Therefore, there has been a demand for developing techniques that can either introduce true dilatational or shear deformations at fluid-fluid interfaces. In comparison to pure dilatational deformations, techniques for true shear deformations are well developed in literature [114]. Our recently published work focuses on development of a custom-built radial Langmuir trough device that can introduce true dilatational at fluid-fluid interfaces [205], and

details of this device is covered in Chapter 3 of this thesis. Another important limitation of the traditional methods is that they lack the ability to visualize the interface in-situ. Past research studies have shown that the interfacial rheological properties can be correlated to the underlying microstructure [16, 60, 70, 206] and therefore, it is beneficial to investigate the microstructure to understand their influence on the interfacial rheological properties. Combining the in-situ visualization techniques with traditional dilatational devices is not trivial and thus, there is a demand for such techniques. Chapter 3 discusses the afore-mentioned challenges of the traditional dilatational methods and they can be referred in that chapter. The novelty of the custom radial Langmuir trough device is that it can perform simultaneous visualization and dilatational deformation of fluid-fluid interfaces. This is achieved by a compact design of the radial Langmuir trough that has a transparent base such that it can be placed over an inverted microscope stage which allows to visualize the interface in-situ.

Dilatational deformations can be applied in the form of constant rate of change of area or oscillatory area deformations at a given frequency. The deformations cause the interfacial stress to change and the relationship between the stress and the strain gives the interfacial rheological properties. Chapter 3 showcases the use of the former type of dilatational deformations. This work focuses on the oscillatory dilatational deformations of DPPC at air-water interface, where the interfacial area is changed in harmonic pattern at a given frequency. Oscillatory area deformations aids to capture the dynamic response of the interface in presence of DPPC and therefore, quantifies the dilatational viscoelastic modulus (E) of DPPC at air-water interface. As mentioned previously, DPPC is a commonly used phospholipid in various applications. Therefore, it has been a matter of interest for scientists to study its interfacial rheological behavior [66, 98, 159, 207]. Studies have also shown that DPPC tends to exhibit microstructure

that is sensitive to external factors like presence of impurities or pH and this microstructure can be correlated to the properties like surface pressure and viscoelasticity [66, 117, 142, 164, 208]. However, investigating the DPPC microstructure in-situ during oscillatory dilatational deformation is quite rare in the literature. Thus, most of the experiments for visualization have been performed either ex-situ or are more commonly under shear deformations. In this work, we overcome this gap by using our custom radial Langmuir trough device that can induce oscillatory dilatational deformation and in-situ interfacial visualization. Out of the various for the applications and uses of DPPC that are mentioned previously, we are motivated to explore the DPPC viscoelastic properties to understand its role as a lung surfactant. DPPC is a main component of lung surfactant, and it naturally undergoes oscillatory dilatational deformations at air-water interface of the alveolar spherical space during the breathing process. In this work we limit our experimental conditions to physiologically relevant surface pressure and frequency of oscillations for DPPC at air-water interface. Three goals are achieved in this work. First, we describe the methodology for implementing the radial area oscillations using the linear motor that actuates the deformations. Second, oscillations are performed at three different desired surface coverage (or concentration) and at single oscillating frequency that is closer to the physiological conditions in mammalian lungs. Surface coverage is confirmed using surface pressure (π) measurements and its typical range is 30 to 65 mN/m [159, 209, 210]. Third, we look at the microstructure of the DPPC at air-water interface and use it to understand the surface pressure behavior and viscoelasticity.

4.2 Methods and Materials

We use the custom radial Langmuir trough to perform the dilatational oscillatory deformations. The design and operations of the radial trough is provided elsewhere [205] or can

be referred in section of chapter 3. In short, the radial Langmuir trough consists of two main parts. First is the stainless-steel sample container or the trough region. It is circular in shape with multiple steps to accommodate the fluid-fluid interface. The container is transparent from the bottom to allow interfacial visualization using an inverted optical microscope. Second is the compression assembly that is used to compress or dilate the interface located in the sample container in a uniform manner. Compression assembly has three main components, namely, elastic barrier that encloses the actual interfacial area, fingers that hold the elastic barrier and a linear motor that actuates the compressive motion. The elastic barrier forms a hexagonal area when held by six fingers that sit on linear slide bearings. This elastic barrier is placed on top of the sample container such that the barrier touches the fluid-fluid interface, and the resulting enclosed interfacial space becomes the available interfacial area. The surface-active material which is DPPC in this work is deposited in between this enclosed interfacial area. The linear slide bearings allow the motion of fingers during compression and consequently, it changes the interfacial area. The motion of the fingers and hence the interfacial area is actuated by a linear motor. The top part of the fingers contained inside an iris diaphragm which opens and shuts as the linear motor moves. The linear motor motion is governed by an in-built software, Zaber Console. This software uses C# programming language for algorithms that controls the linear motor position. Overall, the interfacial area enclosed inside the elastic barrier deforms uniformly from all sides and therefore the radial Langmuir trough induces a true dilatational deformation.

4.2.1 Dilatational Area Oscillations

To achieve the dilatational area oscillations, the motion of the linear motor must be coordinated such that the linear movement translates to oscillatory area changes. The interfacial area is approximated as circular area and a sinusoidal area change in can be expressed as follows:

$$A = A_o + A_a \cdot \sin(2\pi ft + \theta_a) \quad (4.1)$$

$$A = A_o + \pi r^2 \quad (4.2)$$

Here, A_o is the starting area for oscillation, A_a is the amplitude of area oscillations, f is the oscillation frequency, t is time, θ_a is the phase angle and r is the radius of the circular area or the radial position. Equation 4.2 can be linearized using Taylor series expansion to get,

$$A \approx 2\pi r_o \cdot r - 2A_o \quad (4.3)$$

Combining equations 4.1, 4.2 and 4.3 we can express the radius of the interfacial circular area as

$$r = \frac{A_a \cdot \sin(2\pi ft + \theta_a) + 2A_o}{2\pi r_o} \quad (4.4)$$

Here, r_o is the radial position corresponding to the starting area A_o . The radial position r can be directly related to the linear motor position L because, the motion of the linear motor causes the radial position to change. The calibration between these two values is provided in Appendix B.

Using that calibration, the motor position can be expressed as follows:

$$L = \frac{1}{-0.3197} \cdot \left(\frac{A_a \cdot \sin(2\pi ft + \theta_a) + 2A_o}{2\pi r_o} - 15.06 \right) \quad (4.5)$$

Equation 4.5 can be plugged in as the algorithm to actuate the oscillatory deformations at given A_o , A_a , and f . The algorithm is scripted in Zaber Console, and is provided in Appendix C.

Further, the oscillatory strain (γ_a) percentage is estimated by the formula, $\gamma_a = \frac{A_a - A_o}{A_o} \times 100$.

The viscoelastic modulus (E) is defined by the relationship between the change in interfacial stress (σ) due to the change in the strain/area deformations. The change in interfacial stress is related to the surface pressure (π) and is given as, $\Delta\sigma = -\Delta\pi$. The complex viscoelastic modulus is expressed as [193, 211]:

$$E = A_o \frac{-\Delta\pi}{\Delta A} \quad (4.6)$$

Here, $\Delta A = A_a - A_o$. Due to the oscillatory area strain, the surface pressure response is also sinusoidal and has a phase angle, θ_s . The phase difference, θ , between them is phase lag between the oscillatory surface pressure response and area strain and is calculated by, $\theta = \theta_s - \theta_a$. The dilatational elasticity or the dilatational storage modulus is given by $E_e = E \cos\theta$, and the dilatational viscosity or the dilatational loss modulus is given by $E_v = E \sin\theta$.

4.2.2 Sample Preparation

DPPC was obtained as a solution in chloroform from Avanti Polar Lipids Inc., USA and was diluted to a concentration of 0.198 mg/mL using HPLC grade chloroform. A fluorescent dye Texas red, 1,2-dihexadecanoyl-sn-glycero-3-phosphoethanolamine (TR-DHPE) (Invitrogen, USA) was added (0.1 wt. %) in this solution for visualization of DPPC at air-water interface. Other preparatory details are same as from the previous work [205].

Method for interface preparation and surface pressure measurement is the same as from previous work [205] and details can be referred there. A short summary is provided here. A Wilhelmy balance with platinum rod (Pt-rod) was used to record the surface pressure of the air-water interface. A clean sample container is filled with deionized water and the surface pressure for clean water is recorded. For clean water, surface pressure equals the surface tension of the water and was found to around -70 mN/m in each experiment. Next, DPPC is spread dropwise inside the elastic barrier using a 1 μ L Hamilton glass syringe and 30 mins of wait time was maintained to allow chloroform evaporation. All the experiments at performed at room temperature.

Sample visualization details are again same as from the previous work [205]. The details of the microscope can be found in there. In this work, we use 40× water dipping objective and Texas Red fluorescent filter cube to visualize DPPC at air-water interface. The labeled DPPC molecules arrange in way such that under fluorescence, the DPPC rich region appears dark, and the dye region appears bright.

4.3 Results and Discussions

The radial trough was used to perform dilatational area oscillations of DPPC sample deposited at air-water interface. As mentioned early on in this chapter, the experiments are motivated by the physiological breathing process in mammals. DPPC a main component of lung surfactant experiences oscillatory dilatational deformation during respiration. Thus, characterizing viscoelastic properties of DPPC at air-water interface can aid in understanding the role of surfactant in reducing the work required for breathing [159]. Experimental conditions therefore align with the physiological conditions. Due to lack of ability to control the environmental temperature, the experiments were not performed at physiological temperature. Two different initial surface coverages were chosen as the mean oscillation point. Surface coverage is a measure of amount of DPPC per unit interfacial area and can be expressed in mg/m^2 . As the interface undergoes compression or dilatation, the surface coverage changes and correspondingly the mean molecular area of DPPC also changes. Because of the strain deformation the surface pressure also changes. This is captured in the surface pressure versus mean molecular area plot. Lower coverage corresponds to lower surface pressure and a higher mean molecular area, and vice versa. First, the air-water interface is deposited with a certain spreading coverage of DPPC and then the interface is compressed to achieve a desired starting coverage.

4.3.1 Dilatational Oscillatory Measurements

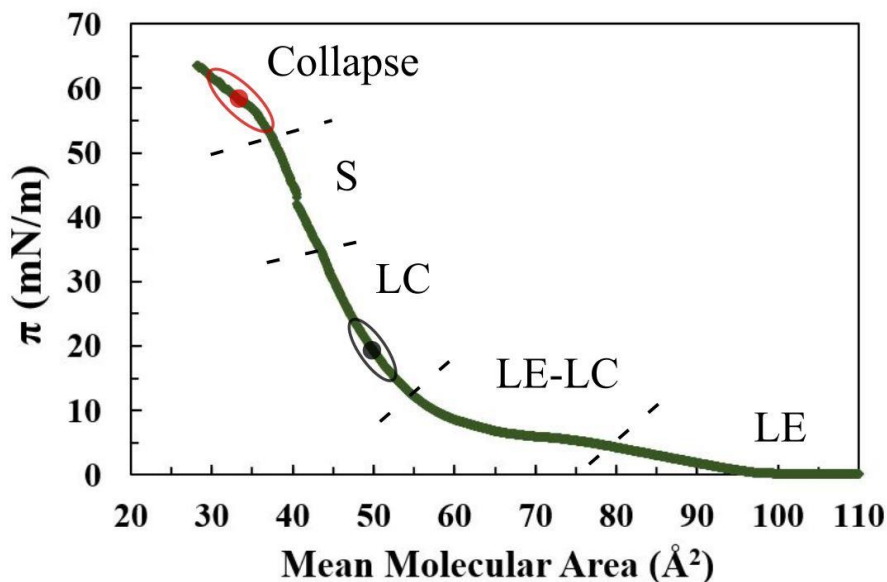


Figure 4.1 Surface pressure (π) of DPPC at air-water interface as a function of mean molecular area. The dotted lines indicate the different phase regions of DPPC during compression of the interface. The black solid circle represents lower surface coverage, and the red solid circle is a higher surface coverage. The corresponding surrounding boundaries (black oval and red oval) are the region of oscillation amplitude.

Fig. 4.1 shows surface pressure-area isotherm of DPPC at air-water interface. This compression measurement was performed with a conventional rectangular Langmuir trough with constant rate of change of area and is adopted from Chapter 3. It depicts phase behavior of DPPC molecules as the interface is compressed and the results observed are consistent with the literature [155, 182, 208]. At high mean molecular areas (85 to 110 \AA^2), the DPPC molecules at air-water interface behaves almost like gas and this phase is called as the liquid-expanded phase (LE). This phase is identified with very low π values (below 5 mN/m). Between 5 to 12 mN/m, first order phase transition occurs from LE phase to a liquid-condensed (LC) phase. Above 12 mN/m, the slope increasing drastically as the DPPC molecules pack to form LC phase structure. A second order transition to solid phase (S) begins around 28-30 mN/m and continues

up to 50 mN/m. At 50 mN/m or approximately around 34 \AA^2 the DPPC molecules pack to form a monolayer. A compression beyond this, leads to collapsing of monolayer structure. This region is identified as a decrease in slope. For the oscillatory dilatational experiments, the two different starting points are highlighted in Fig. 4.1. A lower DPPC coverage is indicated with a black solid circle, and this corresponds to a mean molecular area of $A_o \sim 50 \text{ \AA}^2$. This coverage is below the monolayer formation coverage. The higher DPPC coverage is indicated with a solid red circle, and this corresponds to $A_o \sim 34 \text{ \AA}^2$ and at this point DPPC forms a monolayer. These two areas are the fulcrum point for the oscillations. The region of small amplitude area oscillations in each case depicted by the ovals around the solid circles.

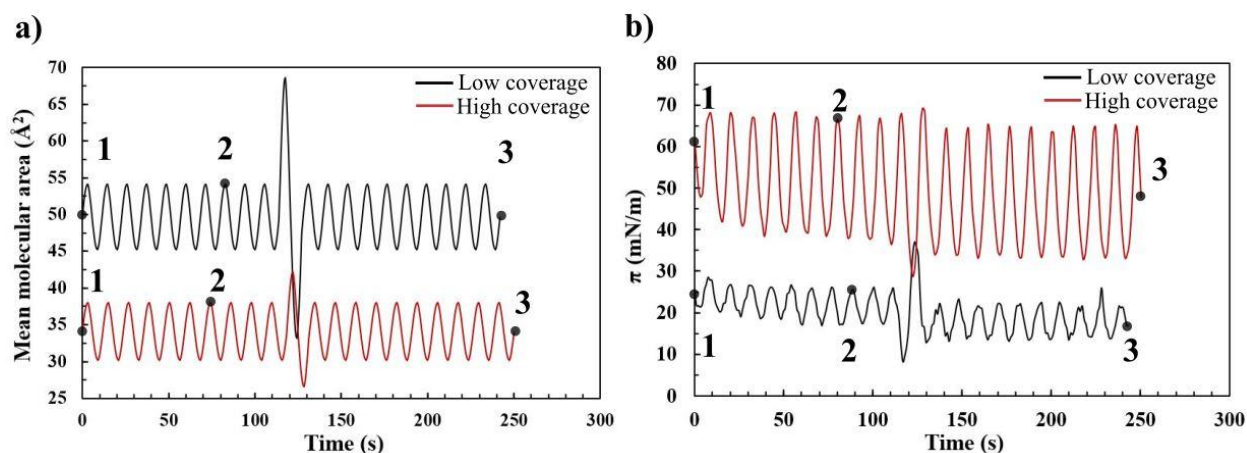


Figure 4.2 a) Induced sinusoidal area oscillations as a function of time. The y-axis represents the physical oscillatory signal expressed as mean molecular area of DPPC. Black curve is induced oscillations at lower DPPC coverage while red curve is for higher DPPC coverage. b) Surface pressure (π) response of the DPPC air- interface measured with Wilhelmy balance. Black curve is the π response at low DPPC coverage and red curve the π response at high DPPC coverage. In both part a and part b, locations 1, 2 and 3 are the points where DPPC microstructures were recorded in-situ.

Fig 4.2 represents the oscillatory signal that was induced using the radial Langmuir trough and the corresponding surface pressure response of the DPPC air-water interface.

Equation 4.5 was used to generate the oscillatory deformation using the linear motor and the associated instantaneous motor position was converted to mean molecular area of DPPC. In each experiment, the conversion was made using the known coverage of DPPC during spreading. After spreading the DPPC sample, the interface was compressed at a constant rate to achieve the desired initial coverage. Once the desired coverage was obtained, oscillations were performed after a wait time of ten seconds. Fig. 4.2b, captures the π measurements made using Wilhelmy balance for both the coverages. In each oscillatory signal, ten small amplitude oscillations were followed by one relatively large amplitude oscillation. Further, another set of the same ten small amplitude oscillations followed the large amplitude oscillation. This pattern of the signal is a representation of the breathing process. The large amplitude oscillations can be thought of as coughing, a sigh, or a yawn. The aim is to understand whether the abrupt stretching of the interface or high area strain affects the spreading behavior or microstructure of DPPC.

The work performed by Caro et. al [207], showed the effect of amplitude and frequency on the dilatational viscoelastic properties of DPPC at air-water interface. Their results depicted that for a π range of 20 to 35 mN/m i.e., a corresponding mean molecular area range of 50 to 40 \AA^2 , respectively, and with small amplitudes (up to $\gamma_a=20$) and 0.1 Hz frequency, the DPPC interface behaves reversibly and gives a linear response. This is because, the DPPC domains are predominantly in LC phase where the microstructure can rearrange reversibly. Consequently, the oscillatory π responses are reproducible. With this knowledge, we first performed oscillatory deformation at lower DPPC coverages (below a monolayer formation) and see if we observe similar results. For this, we selected a surface coverage of 2.45 mg/m² which corresponds to a mean molecular area of $A_o= 49.55$ or approximately 50 \AA^2 . At this A_o , small amplitude oscillations were performed at 7% area strain and large amplitude oscillation was performed at

30% area strain. The oscillation frequency is approximately 0.08 Hz which is typical range of breathing frequency i.e., 0.04 to 0.2 Hz [159]. The black curve in Fig. 4.2b is the π response of area oscillatory strain. We observed that the π response was reproducible for small amplitude oscillations and this in alignment with the literature. Further, we observed that, after the introduction of large amplitude oscillation, the π response was reproducible but with a reduced mean π value. Similar observations were obtained with the repeat measurements. At 30% area strain the highest π compression value reached above 35 mN/m. Above this surface pressure, the interface transitions to a solid phase from a LC phase. The DPPC domains at this transition region interact irreversibly affecting the DPPC spreading [207]. We attribute the reduced mean π value to irreversible changes in DPPC domains at high π values. We corroborate this result with the DPPC microstructure, and this is explained in the last section of this chapter.

Next, we performed similar set of oscillatory deformation at higher DPPC coverage that corresponds to a mean molecular area of 34 \AA^2 and this demonstrated with red curves in Fig 4.3a and Fig. 4.3b. At this area, DPPC forms a monolayer at the interface and the π values correspond to the collapse region. This is also the region that is very close to the physiological conditions i.e., π above 50 mN/m [98, 159]. At such high compressions, DPPC is in a solid like phase and the intermolecular structural rearrangements are irreversible. We investigate this behavior using by looking at the surface pressure response to oscillatory deformations. Ten oscillations of 10% area strain were applied followed by a single large oscillation of 20 % area strain. Large oscillation was followed by the another set of ten small amplitude oscillations. The oscillation frequency was approximately 0.08 Hz. In Fig. 4.3b, we observed that the small amplitude oscillations are reproducible but like previous measurement, after the large amplitude oscillation, there was a reduction in mean value of π . To a certain extent, this was expected behavior as the

experiment was performed in the collapse region where DPPC domains form irreversible structural changes. Another possible reason by the reduced mean value of π can be the that, at such high pressures, DPPC tends to desorb into the sub-phase and there is loss of material. For mammalian lungs, it is reported that DPPC is lost in sub-phase and the alveolar cells produce more surfactant to maintain the interfacial concentration. However, the small amplitude oscillations are still reproducible. This may occur because of the stability of the structure that is formed in the collapse region. In the collapse region, the two-dimensional monolayer DPPC structure transforms to a three-dimensional structure with bilayers [169]. Such stable structures are predicted for mammalian lungs as they are responsible to sustain the alveolar collapse at high compressions [98]. Further, with the same high coverage DPPC interface we consecutively applied two sets of oscillatory deformations. Ten small amplitude oscillations are followed by one large amplitude oscillation followed by another ten small amplitude oscillations, and this is done consecutively for a total of 42 cycles. Here, we observed that after each large amplitude oscillation there is a reduction in the mean value of π . This confirms that there is certain irreversible structural rearrangement due to large amplitude. Further, the rearranged structure seems to be stable because during the small amplitude oscillations are reproducible in each set.

For the high coverage DPPC experiment, we also evaluated the viscoelastic modulus of the interface. Past studies have shown that DPPC at air-water interface has a linear viscoelastic response in the LC phase and the modulus increase steeply with higher coverage [98, 159]. The complex dilatational viscoelastic moduli in this phase depend on both frequency and amplitude of oscillations. In the solid phase or the collapse region, the viscoelastic response is non-linear. Studies show that at pressures above 50 mN/m, dilatational elasticity dominates and this in turn supports the solid like nature of the interface at these coverages. In our experiment for high

DPPC coverage, our surface pressures are above 50 mN/m. For this, we estimate the viscoelastic moduli at both 10% and 20% area strains. Using equation 4.6 we get the complex viscoelastic modulus of $E^{10} = 133.84$ mN/m and $E^{20} = 99.57$ mN/m, for 10% and 20 % strain respectively. Notice that the moduli is lower for a higher strain. This can be explained by the non-linear response of the DPPC interface at high surface pressures. These values are similar to what is reported in previous studies for high DPPC coverages [98]. Further to understand whether the interface behaves more elastic or viscous we calculate the difference in phase angles of the oscillatory strain and oscillatory stress (surface pressure). We perform regression analysis on the sinusoidal data and fit a sine curve to get the phase angles. Using the equations, $E_e = E \cos\theta$ and $E_v = E \sin\theta$ we can estimate dilatational elasticity and viscosity respectively. For a phase difference of 0° , the interface is truly elastic and for a phase difference of 90° the interface is fully viscous. Any phase difference between these values means the interface is viscoelastic. Before calculating the phase difference, one must consider the additional phase lag imposed by the electro-mechanical response of the Wilhelmy balance that is used to make the surface pressure measurement. In the unpublished work by Samaniuk and Vermant [212], they show that Wilhelmy balance impose a significant phase lag on the measured surface pressure and is additive in nature. They calibrate the phase lag for different frequencies and for the frequency of 0.08 Hz that we use in this work the phase lag is about 20.6° . In our phase calculations we simply subtract this value to obtain the true phase difference of the interface. For 10 % area strain we get a phase difference of 5.6° and for 20% area strain we get a value of 0.9° . These phase of DPPC air-water interface indicate that the interface is highly elastic at these coverages. Moreover, at 20 % area strain the dilatational elastic moduli is low and this means a higher

compressibility (inverse of elasticity). This situation is in fact favorable for breathing processes as higher compressibility reduces the work required for respiration [98].

4.3.2 Visualization Experiments

Fig. 4.3 shows DPPC at air-water interface at two different starting mean molecular areas. The images were obtained in-situ during the deformations of the interface. Since the applied deformations are oscillatory, the interface focal plane changes during the deformations. To counter this, the focal plane is adjusted in the initial couple of oscillations. The interfacial compression velocity is lowest at the peaks of the sinusoidal wave. Therefore, it is easy to capture images at peaks. In our experiment we capture images at the beginning and end of oscillations and at highest compression point of small amplitude oscillatory deformations. In all the images DPPC rich region appears at dark area and dye rich regions appear as bright areas.

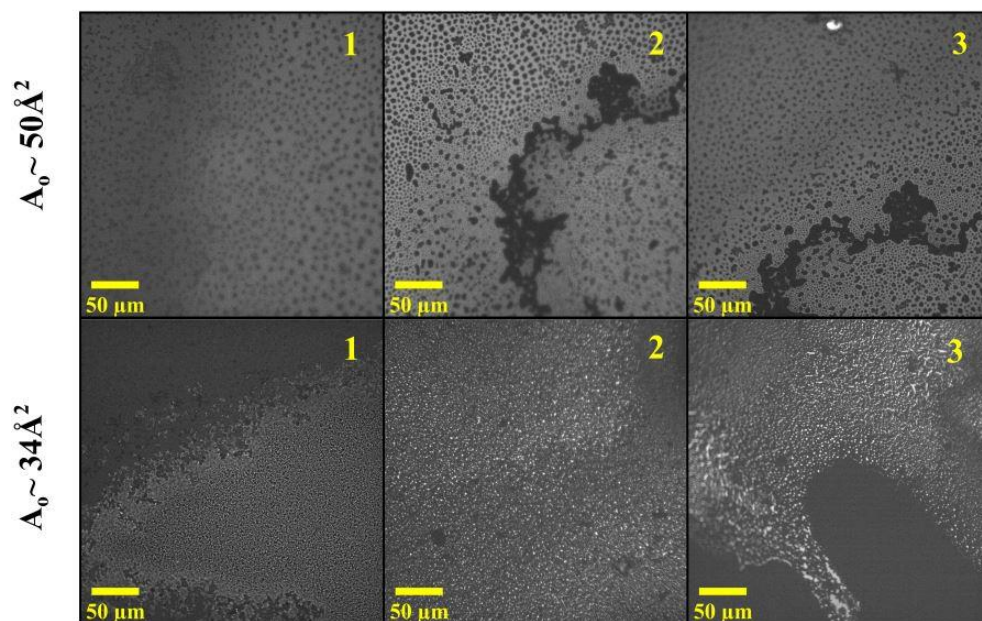


Figure 4.3 DPPC at air-water interface visualized under fluorescent microscopy. Images 1, 2 and 3 in each row correspond to location in Fig. 4.2. The scale bar represents a size of $50\ \mu\text{m}$ and the total width of the image is close to $320\ \mu\text{m}$. In both top row ($A_o \sim 50\ \text{\AA}^2$) and bottom row ($A_o \sim 34\ \text{\AA}^2$), location 1 indicates the microstructure at A_o before the oscillations begin, 2 is the microstructure at the highest compression region in small amplitude oscillation and 3 is the microstructure again at A_o but after oscillations are completed.

The top row of Fig. 4.3 shows DPPC microstructure during the oscillatory measurement starting at $A_o \sim 50\ \text{\AA}^2$. The oscillatory signal is the same as that applied for surface pressure measurements. Image 1 shows the microstructure at beginning of small amplitude oscillation (7% strain). We observed that the circular DPPC domains are uniformly spread at the interface. This structural arrangement aligns with other studies in literature in the LC phase [98]. As the oscillations begin, the interface compresses to highest peak of small amplitude oscillation and this corresponds to image 2. It is clear from image two that DPPC domains move closer and some domains aggregate to form clusters of DPPC. In terms of viscoelasticity, the cluster areas are more solid like or elastic while rest of the region is more fluid like. Further, we observed that

at the end of oscillations, which is image 3, the microstructure is very similar to that of image 2. This occurs even when the pressures are lower at end of oscillations. One way to explain this behavior is that the aggregated microstructure undergoes irreversible changes during the period of oscillation. This therefore supports the observation in surface pressure measurement made at $A_o \sim 50 \text{ \AA}^2$. DPPC forms more compact structures and do not spread well after the large amplitude oscillation and thus does not reduce the surface tension of water effectively and hence a lower π value at the end of oscillations.

The bottom row Fig. 4.3 show DPPC microstructure observed during the oscillatory measurement starting at $A_o \sim 34 \text{ \AA}^2$. Again, the oscillatory signal is same as the signal for high coverage DPPC in Fig. 4.2. In all the images 1, 2 and 3 there is no definitive microstructure as this is the collapse region of DPPC air-water interface. Maximum fluorescent dye is expelled from the DPPC molecules leaving largely a dark region under visualization. This in turn supports the observation that the interface is highly elastic in this region. In general, microscopy is not a suitable method to investigate the interfacial structure of DPPC at very high coverages. However, we looked at the images of this interface before and after oscillations at spreading coverage which was around 2.25 mg/m^2 . The microstructure was highly aggregated at this spreading coverage indicating that irreversible structural changes had occurred.

4.4 Conclusions

We used the radial Langmuir trough to perform dilatational deformations of a model lung surfactant molecule, DPPC, at air-water interface. Oscillatory surface pressure response of DPPC interface was recorded using Wilhelmy balance for the applied area oscillations. At low DPPC coverage, small amplitude oscillatory surface pressure response was reproducible. However, an application of sudden stretch to the interface or relatively large area amplitude caused a reduction

in mean surface pressure of the small oscillations that followed it. This behavior was attributed to the irreversible changes in DPPC intermolecular interaction and/or microstructure that occurred when DPPC reached a solid phase transition due to large amplitude oscillation. This result was supported by interfacial visualization of DPPC. DPPC interfacial visualization showed that the aggregated domains intact even after the oscillations ended i.e., they do not spread well and hence reduces the surface pressure reading.

To characterize the interfacial properties of DPPC near physiological conditions we chose a relatively high DPPC coverage. Small amplitude oscillatory surface pressure response was again found to be reproducible. After a large amplitude oscillation, the mean value of pressure reduced. Dilatational viscoelastic moduli were evaluated for both small and large amplitude oscillations. It was observed that the moduli for large amplitude strain was lower than small amplitude strain. This suggested the non-linear viscoelastic response of DPPC interface. Further, the interface was found to highly elastic at this DPPC coverage. Visualization of the interface showed collapsed solid like structure, and this supports the observation that interface is elastic.

Overall, we were able to correlate dilatational viscoelastic properties of DPPC at air-water interface to the DPPC microstructure. The novelty of this work is that the radial trough can perform true dilatational oscillations and direct in-situ visualization of the interface. The methodology and ability to implement dilatational area oscillations can be extended to various types of fluid-fluid interfaces.

CHAPTER 5

FUTURE WORK

The thesis work has proposed two novel techniques in combination of microscopy to characterize the material's viscoelastic properties. The work covers the design and implementation of some important applications using these methods. The emphasis of this Chapter is to highlight the future scope of these newly developed techniques beyond the stated applications. It is not feasible to include every possible application for these devices and therefore we only focus on a couple of interesting applications that are relevant to the current developments in scientific domain.

5.1 Artificial Thermal Noise for Viscoelastic Materials

One of the challenges mentioned in Chapter 2 is that the single coil electromagnetic tweezer method can be applied only to Newtonian fluids. Many interesting materials are viscoelastic, and therefore, we look at a potential way to use the electromagnetic tweezers for probing a viscoelastic material. For this, a straightforward approach is to use a two-coil system. One of the preliminary data of applying a white noise signal using a two-coil system for viscoelastic material was demonstrated in Chapter 1 (see Fig.1.1). A hurdle with this approach is that for relatively high moduli materials, the coils must be moved closer to achieve the required forces and at such short distances, there is significant coil-coil interference. Due to this, the applied forces and the resulting particle motion are inaccurate.

To compensate for the coil-coil interference, an active feedback control system can be implemented. Feedback systems for tuning the magnetic fields of electromagnets have been

developed in the past [95, 213]. The feedback system needs to be sophisticated and robust to accurately tune the force. We propose the use of an active feedback control system that can consistently track the instantaneous particle position and modify the magnitude of the magnetic field in accordance with the motion. To counter the coil-coil interference, Hall probe devices should be attached to the electromagnets such that they measure instantaneous magnetic fields. The feedback from the particle position and amount of interference can then be used to tune these magnetic fields. Additionally, all changes in the force should follow the constraints of the signal type i.e., the signal's randomness must be maintained. Execution of this plan might require collaborations with expertise from the field of electronics and magnetics.

5.2 Interactions of Lipid Membranes and 2D Particles

Understanding the interactions between biological membranes and colloidal scale or nanoparticles has been a topic of interest for researchers owing to the applications in drug delivery systems (DDS) [214] and to the potential toxicity of some artificial particles like pollutants [208, 215]. Current experimental techniques to visualize the membrane-particle interactions in-situ are limited. This is especially true for interactions of 2D particles with bio membranes. 2D particles are those whose thickness is sub-nanometer scale, and the lateral dimension is colloidal scale. Due to their unique properties like electrical conductivity, chemistry, and shape, 2D particles have become popular in many applications including DDS [216-218]. Therefore, investigating the influence of 2D particles at bio membranes like phospholipids inside lung alveoli is beneficial. With this motivation, we propose a project to study interaction of 2D graphene particles with DPPC at air-water interface. This system will serve as a prototype to study aggregation kinetics and influence of 2D graphene particles on model lung surfactant, DPPC.

Our hypothesis is that the lateral diffusion of 2D particles in contact with phospholipid monolayers is dependent on several variables, including particle chemistry, the number of stacked layers, and the membrane area density, and that this is related to both the physical position of the particle in the membrane (e.g., surfing on lipid tails vs embedded), and the influence the particle has on the surrounding phospholipid structure. For example, previous study with molecular dynamics simulation showed that non-diffusive Brownian motion or a Lévy like dynamics can be induced when the oxidation state of graphene is altered [219]. For the purposes of the use of radial Langmuir trough, the specific aim is to study how the graphene monolayer diffusion and diffusive type depend on the DPPC monolayer concentration and particle oxidation.

To achieve this aim there are three parts to study. First, fabrication of shape and size-controlled graphene particles at different oxidation state and different number of layers. The work by Goggin and Samaniuk [220] provide details of how fabrication can be achieved and we have the resources to accomplish this. The aim is to fabricate graphene discs with either monolayer or multiplayer and at various oxidation states. Second, ability to control the DPPC monolayer coverage and hence its concentration at air-water interface. This can be performed conveniently with the use of our custom radial Langmuir trough device described in Chapter 3. Third, observing the diffusion of different type of graphene particles (pristine vs oxidated) at air-water interface in the presence of DPPC monolayers. To achieve this, the equipment requires the ability to capture the particle motion in-situ. Again, this feature is available with the radial Langmuir trough. Once the desired particles are fabricated, they can be transferred to air-water interface and then DPPC at some initial coverage can be added to the same interface. The radial Langmuir trough can then be used to compression the interface to achieve different DPPC

coverages. The in-situ visualization can track motion of the deposited graphene discs. There are standard particle tracking algorithms in MATLAB (very similar to those used in Chapter 2) that can be used to track the particle motion. The motion can be used to estimate the mean squared displacement (MSD) and diffusion of the graphene discs. The diffusion analysis will provide information on the type of diffusion. We expect that the magnitude of diffusion of graphene particles reduces as the DPPC concentration increases.

CHAPTER 6

CONCLUSIONS

The need for rheological characterization of materials has gained importance as it provides insights to materials fundamental properties that are directly or indirectly related to their quality and performance. In this thesis, we attempt to address certain challenges of conventional tools that have been used in the domain of microrheology and interfacial rheology to characterize the viscoelastic properties of complex materials. To overcome those challenges, we introduced methods that are a combination of our novel rheological tools and microscopy.

In Chapter 2 we show that artificial thermal noise can probe a Newtonian fluid with viscosity that is an order of magnitude higher than the typical measurable limit of passive particle tracking microrheology (PTM). We use single coil electromagnetic tweezer to produce stochastic magnetic forces that fluctuates the probe particle with approximately 10 kT external energy. Our results show that the magnitude of the applied forces is proportional to the particle fluctuations. The main advantage of this technique is the random nature of the of applied forces that allows us to use the standard hydrodynamic model like the Stokes-Einstein equation to evaluate viscosity. The reproducibility of this technique depends on the variations in the physical properties like magnetic susceptibility of the colloidal scale superparamagnetic particle.

Chapter 3 and 4 demonstrates that simultaneous dilatational deformations and microscopic interfacial visualization enables understanding of the structure-property relationship of complex fluid-fluid interfaces. To achieve this, we developed a compact radial Langmuir trough device that operates in tandem with inverted optical microscope. Further, the unique

feature of simultaneous deformation and visualization allows to test and develop complex constitutive equations.

In Chapter 3, we performed constant rate of change of area deformations to measure the surface pressure-area isotherms of an acrylic polymer PtBMA and a lung surfactant DPPC at air-water interface. The last section of this chapter discusses a critical challenge of miniaturizing a trough system. Due to the compact size of the radial trough, the interfacial curvature or capillary deformation effects are high, and they affect the measured surface pressure. To minimize this, we silanized the parts of the radial trough that are in contact with the air-water interface. This allows to achieve a contact angle close to 90° and hence reduce the curvature. In case of PtBMA, the curvature effects were negligible, and the surface pressure measurement was in great agreement to the literature. Moreover, in one of its kind experiments we were able to visualize the wrinkling of PtBMA thin film in-situ during the interfacial compression. Based on the period of wrinkling we were able to extract the dilatational compression modulus or the Young's modulus of the PtBMA film at air-water interface. In case of DPPC at air-water interface, the curvature effects had significant effects on the surface pressure measurements. One of the possible reasons to explain this was the change in microstructure of DPPC during the interfacial deformation.

Chapter 4 is the on-going work that focuses on the application of oscillatory dilatational area deformations of fluid-fluid interfaces. These type deformations allow us to capture the dynamic response of the interface and to characterize their viscoelastic modulus. We performed oscillatory area deformation on DPPC at air-water interface. Viscoelastic moduli at different oscillatory amplitudes were estimated and related to the changes in DPPC structure that were observed using fluorescent microscopy.

In summary, our novel rheological tools provide methods for characterizing material properties in both bulk and fluid-fluid interfaces. The proposed methods are a step forward in advancing the theoretical and experimental approach in rheology.

REFERENCES CITED

- [1] D. Doraiswamy, The origins of rheology: a short historical excursion, *Rheology Bulletin* 71 (2002) 1-9.
- [2] K. Walters, History of rheology, *Rheology-Volume I* (2010) 14.
- [3] P.A. Janmey, M. Schliwa, *Rheology, Current biology* : CB 18(15) (2008) R639-R641.
- [4] D. Breuer, W.B. Moore, 10.08 - Dynamics and Thermal History of the Terrestrial Planets, the Moon, and Io, in: G. Schubert (Ed.), *Treatise on Geophysics (Second Edition)*, Elsevier, Oxford, 2015, pp. 255-305.
- [5] M.T.K. Kubo, M.L. Rojas, A.C. Miano, P.E.D. Augusto, Chapter 1 Rheological Properties of Tomato Products, *Tomato Chemistry, Industrial Processing and Product Development*, The Royal Society of Chemistry 2019, pp. 1-25.
- [6] S. Ebnesajjad, 12 - Fabrication and Processing of Polytetrafluoroethylene Dispersions, in: S. Ebnesajjad (Ed.), *Fluoroplastics (Second Edition)*, William Andrew Publishing, Oxford, 2015, pp. 278-299.
- [7] P.A. Cornwell, A review of shampoo surfactant technology: consumer benefits, raw materials and recent developments, *International Journal of Cosmetic Science* 40(1) (2018) 16-30.
- [8] C.R. Vithanage, M.J. Grimson, B.G. Smith, The effect of temperature on the rheology of butter, a spreadable blend and spreads, *Journal of Texture Studies* 40(3) (2009) 346-369.
- [9] P. Deptuła, D. Łysik, K. Pogoda, M. Cieśluk, A. Namiot, J. Mystkowska, G. Król, S. Głuszek, P.A. Janmey, R. Bucki, Tissue Rheology as a Possible Complementary Procedure to Advance Histological Diagnosis of Colon Cancer, *ACS Biomaterials Science & Engineering* 6(10) (2020) 5620-5631.
- [10] S. Róžańska, Chapter 6 - Extensional Rheology in Food Processing, in: J. Ahmed, P. Ptaszek, S. Basu (Eds.), *Advances in Food Rheology and Its Applications*, Woodhead Publishing 2017, pp. 125-157.
- [11] H. Münstedt, Extensional Rheology and Processing of Polymeric Materials, *International Polymer Processing* 33(5) (2018) 594-618.
- [12] Q. Huang, N.J. Alvarez, Y. Matsumiya, H.K. Rasmussen, H. Watanabe, O. Hassager, Extensional Rheology of Entangled Polystyrene Solutions Suggests Importance of Nematic Interactions, *ACS Macro Letters* 2(8) (2013) 741-744.
- [13] Rheometer geometries: relative measuring geometries. <https://wiki.anton-paar.com/us-en/rheometer-geometries-relative-measuring-geometries/>.

- [14] D. Weihs, T.G. Mason, M.A. Teitell, Bio-Microrheology: A Frontier in Microrheology, *Biophysical Journal* 91(11) (2006) 4296-4305.
- [15] K. Joyner, S. Yang, G.A. Duncan, Microrheology for biomaterial design, *APL bioengineering* 4(4) (2020) 041508-041508.
- [16] G.G. Fuller, J. Vermant, Complex Fluid-Fluid Interfaces: Rheology and Structure, *Annual Review of Chemical and Biomolecular Engineering* 3(1) (2012) 519-543.
- [17] H. Münstedt, Rheological Measurements and Structural Analysis of Polymeric Materials, *Polymers (Basel)* 13(7) (2021) 1123.
- [18] G.M. Conley, C. Zhang, P. Aebischer, J.L. Harden, F. Scheffold, Relationship between rheology and structure of interpenetrating, deforming and compressing microgels, *Nature Communications* 10(1) (2019) 2436.
- [19] S. Portal-Marco, M.À. Vallvé, O. Arteaga, J. Ignés-Mullol, C. Corbella, E. Bertran, Structure and physical properties of colloidal crystals made of silica particles, *Colloids and Surfaces A: Physicochemical and Engineering Aspects* 401 (2012) 38-47.
- [20] V. Calabrese, S. Varchanis, S.J. Haward, J. Tsamopoulos, A.Q. Shen, Structure-property relationship of a soft colloidal glass in simple and mixed flows, *Journal of Colloid and Interface Science* 601 (2021) 454-466.
- [21] J. Larsson, A. Sanchez-Fernandez, A.E. Leung, R. Schweins, B. Wu, T. Nylander, S. Ulvenlund, M. Wahlgren, Molecular structure of maltoside surfactants controls micelle formation and rheological behavior, *Journal of Colloid and Interface Science* 581 (2021) 895-904.
- [22] D.M. Schenck, J. Fiegel, Tensiometric and Phase Domain Behavior of Lung Surfactant on Mucus-like Viscoelastic Hydrogels, *ACS Applied Materials & Interfaces* 8(9) (2016) 5917-5928.
- [23] J.C.-W. Lee, K.M. Weigandt, E.G. Kelley, S.A. Rogers, Structure-Property Relationships via Recovery Rheology in Viscoelastic Materials, *Physical review letters* 122 24 (2019) 248003.
- [24] P.A. Janmey, P.C. Georges, S. Hvidt, Basic rheology for biologists, *Methods Cell Biology* 83 (2007) 3-27.
- [25] M. Faith, *Understanding Rheology*, Oxford University Press, New York, 2001.
- [26] M.L. Gardel, M.T. Valentine, D.A. Weitz, Microrheology, in: K.S. Breuer (Ed.), *Microscale Diagnostic Techniques*, Springer Berlin Heidelberg, Berlin, Heidelberg, 2005, pp. 1-49.
- [27] W. Liu, C. Wu, Rheological Study of Soft Matters: A Review of Microrheology and Microrheometers, *Macromolecular Chemistry and Physics* 219(3) (2018) 1700307.
- [28] N. Yang, R. Lv, J. Jia, K. Nishinari, Y. Fang, Application of Microrheology in Food Science, *Annual review of food science and technology* 8 (2017) 493-521.

- [29] P.E. Arratia, Complex fluids at work, *Physics* 4 (2011) 9.
- [30] B.A. Krajina, C. Tropini, A. Zhu, P. DiGiacomo, J.L. Sonnenburg, S.C. Heilshorn, A.J. Spakowitz, Dynamic Light Scattering Microrheology Reveals Multiscale Viscoelasticity of Polymer Gels and Precious Biological Materials, *ACS Central Science* 3(12) (2017) 1294-1303.
- [31] A.M. Puertas, T. Voigtmann, Microrheology of colloidal systems, *Journal of Physics: Condensed Matter* 26(24) (2014) 243101.
- [32] D. Weihs, T.G. Mason, M.A. Teitell, Bio-microrheology: a frontier in microrheology, *Biophys J* 91(11) (2006) 4296-305.
- [33] P. Cicutta, A.M. Donald, Microrheology: a review of the method and applications, *Soft Matter* 3(12) (2007) 1449-1455.
- [34] E. Nazockdast, J.F. Morris, Active microrheology of colloidal suspensions: Simulation and microstructural theory, *Journal of Rheology* 60(4) (2016) 733-753.
- [35] T.A. Waigh, Advances in the microrheology of complex fluids, *Reports on Progress in Physics* 79(7) (2016).
- [36] T.A. Waigh, Microrheology of complex fluids, *Reports on Progress in Physics* 68(3) (2005) 685-742.
- [37] Q. Xia, H. Xiao, Y. Pan, L. Wang, Microrheology, advances in methods and insights, *Advances in Colloid and Interface Science* (2018).
- [38] F.C. MacKintosh, C.F. Schmidt, Microrheology, *Current Opinion in Colloid & Interface Science* 4(4) (1999) 300-307.
- [39] P. Edera, D. Bergamini, V. Trappe, F. Giavazzi, R. Cerbino, Differential dynamic microscopy microrheology of soft materials: A tracking-free determination of the frequency-dependent loss and storage moduli, *Physical Review Materials* 1(7) (2017) 073804.
- [40] E.M. Furst, T.M. Squires, *Microrheology*, Oxford University Press 2017.
- [41] R. Kubo, The fluctuation-dissipation theorem, *Reports on progress in physics* 29(1) (1966) 255.
- [42] T.G. Mason, D.A. Weitz, Optical measurements of frequency-dependent linear viscoelastic moduli of complex fluids, *Physical review letters* 74(7) (1995) 1250-1253.
- [43] T.G. Mason, Estimating the viscoelastic moduli of complex fluids using the generalized Stokes–Einstein equation, *Rheologica Acta* 39(4) (2000) 371-378.
- [44] A. Heilbronn, Eine neue Methode zur Bestimmung der Viskosität lebender Protoplasten, 1922.

- [45] W. Seifriz, An Elastic Value of Protoplasm, with Further Observations on the Viscosity of Protoplasm, *Journal of Experimental Biology* 2(1) (1924) 1.
- [46] J.V.I. Timonen, B.A. Grzybowski, Tweezing of Magnetic and Non-Magnetic Objects with Magnetic Fields, *Advanced Materials* 29(18) (2017) 1603516-n/a.
- [47] C. Haber, D. Wirtz, Magnetic tweezers for DNA micromanipulation, *Review of Scientific Instruments* 71(12) (2000) 4561-4570.
- [48] C. Chi-Han, H. Yu-Yen, C. Meng-Han, L. Huei-Huang, L. Gwo-Bin, New magnetic tweezers for investigation of the mechanical properties of single DNA molecules, *Nanotechnology* 17(5) (2006) 1217.
- [49] F. Amblard, B. Yurke, A. Pargellis, S. Leibler, A magnetic manipulator for studying local rheology and micromechanical properties of biological systems, *Review of Scientific Instruments* 67(3) (1996) 818-827.
- [50] L.G. Wilson, W.C.K. Poon, Small-world rheology: an introduction to probe-based active microrheology, *Physical Chemistry Chemical Physics* 13(22) (2011) 10617-10630.
- [51] R. Sarkar, V.V. Rybenkov, A Guide to Magnetic Tweezers and Their Applications, *Frontiers in Physics* 4(48) (2016).
- [52] W. Stephenson, G. Wan, S. Tenenbaum, P. Li, *Nanomanipulation of Single RNA Molecules by Optical Tweezers*, 2014.
- [53] A.H.B. de Vries, B.E. Krenn, R. van Driel, J.S. Kanger, Micro Magnetic Tweezers for Nanomanipulation Inside Live Cells, *Biophysical Journal* 88(3) (2005) 2137-2144.
- [54] F. Ziemann, J. Radler, E. Sackmann, Local measurements of viscoelastic moduli of actin networks using an oscillating magnetic bead micro-rheometer, *Biophysical Journal* 66(6) (1994) 2210-2216.
- [55] M. Keller, J. Schilling, E. Sackmann, Oscillatory magnetic bead rheometer for complex fluid microrheometry, *Review of Scientific Instruments* 72(9) (2001) 3626-3634.
- [56] A.R. Bausch, W. Möller, E. Sackmann, Measurement of local viscoelasticity and forces in living cells by magnetic tweezers, *Biophysical Journal* 76(1 Pt 1) (1999) 573-579.
- [57] T. Andersen, P. Auk-Emblem, M. Dornish, 3D cell culture in alginate hydrogels, *Microarrays* 4(2) (2015) 133-161.
- [58] N. Cao, *Fabrication of alginate hydrogel scaffolds and cell viability in calcium-crosslinked alginate hydrogel*, 2011.
- [59] J.B. Rose, S. Pacelli, A.J.E. Haj, H.S. Dua, A. Hopkinson, L.J. White, F.R. Rose, Gelatin-based materials in ocular tissue engineering, *Materials* 7(4) (2014) 3106-3135.

- [60] N. Jaensson, J. Vermant, Tensiometry and rheology of complex interfaces, *Current Opinion in Colloid & Interface Science* 37 (2018) 136-150.
- [61] M. Pepicelli, T. Verwijlen, T.A. Tervoort, J. Vermant, Characterization and modelling of Langmuir interfaces with finite elasticity, *Soft Matter* 13(35) (2017) 5977-5990.
- [62] T. Verwijlen, L. Imperiali, J. Vermant, Separating viscoelastic and compressibility contributions in pressure-area isotherm measurements, *Advances in Colloid and Interface Science* 206 (2014) 428-436.
- [63] P. Erni, Deformation modes of complex fluid interfaces, *Soft Matter* 7(17) (2011) 7586-7600.
- [64] S. Reynaert, C.F. Brooks, P. Moldenaers, J. Vermant, G.G. Fuller, Analysis of the magnetic rod interfacial stress rheometer, *Journal of Rheology* 52(1) (2008) 261-285.
- [65] C.F. Brooks, G.G. Fuller, C.W. Frank, C.R. Robertson, An Interfacial Stress Rheometer To Study Rheological Transitions in Monolayers at the Air–Water Interface, *Langmuir* 15(7) (1999) 2450-2459.
- [66] K. Kim, S.Q. Choi, J.A. Zasadzinski, T.M. Squires, Interfacial microrheology of DPPC monolayers at the air-water interface, *Soft Matter* 7(17) (2011) 7782-7789.
- [67] S.Q. Choi, S.G. Jang, A.J. Pascall, M.D. Dimitriou, T. Kang, C.J. Hawker, T.M. Squires, Synthesis of Multifunctional Micrometer-Sized Particles with Magnetic, Amphiphilic, and Anisotropic Properties, *Advanced Materials* 23(20) (2011) 2348-2352.
- [68] P. Erni, P. Fischer, E.J. Windhab, V. Kusnezov, H. Stettin, J. Lauger, Stress- and strain-controlled measurements of interfacial shear viscosity and viscoelasticity at liquid/liquid and gas/liquid interfaces, *Review of Scientific Instruments* 74(11) (2003) 4916-4924.
- [69] S. Vandebril, A. Franck, G.G. Fuller, P. Moldenaers, J. Vermant, A double wall-ring geometry for interfacial shear rheometry, *Rheologica Acta* 49(2) (2010) 131-144.
- [70] L.M.C. Sagis, E. Scholten, Complex interfaces in food: Structure and mechanical properties, *Trends in Food Science & Technology* 37(1) (2014) 59-71.
- [71] D. Wirtz, Particle-tracking microrheology of living cells: principles and applications, *Annual review of biophysics* 38 (2009) 301-26.
- [72] M. Ehrenberg, J.L. McGrath, Binding between particles and proteins in extracts: implications for microrheology and toxicity, *Acta Biomaterialia* 1(3) (2005) 305-315.
- [73] A. Palmer, J. Xu, S.C. Kuo, D. Wirtz, Diffusing wave spectroscopy microrheology of actin filament networks, *Biophysical journal* 76(2) (1999) 1063-1071.

- [74] O. Galy, P. Latour-Lambert, K. Zrelli, J.-M. Ghigo, C. Beloin, N. Henry, Mapping of Bacterial Biofilm Local Mechanics by Magnetic Microparticle Actuation, *Biophysical Journal* 103(6) (2012) 1400-1408.
- [75] B.W. Peterson, Y. He, Y. Ren, A. Zerdoum, M.R. Libera, P.K. Sharma, A.-J. van Winkelhoff, D. Neut, P. Stoodley, H.C. van der Mei, H.J. Busscher, Viscoelasticity of biofilms and their recalcitrance to mechanical and chemical challenges, *FEMS Microbiology Reviews* 39(2) (2015) 234-245.
- [76] T.M. Squires, T.G. Mason, Fluid Mechanics of Microrheology, *Annual Review of Fluid Mechanics* 42 (2010) 413-438.
- [77] T.A. Waigh, Advances in the microrheology of complex fluids, *Reports on progress in physics. Physical Society (Great Britain)* 79(7) (2016) 074601.
- [78] W. Liu, C. Wu, Rheological Study of Soft Matters: A Review of Microrheology and Microrheometers, *Macromolecular Chemistry and Physics* 219(3) (2017) 1700307.
- [79] J.C. Crocker, D.G. Grier, Methods of Digital Video Microscopy for Colloidal Studies, *Journal of Colloid and Interface Science* 179(1) (1996) 298-310.
- [80] T. Mason, K. Ganesan, J. van Zanten, D. Wirtz, S. C. Kuo, Particle Tracking Microrheology of Complex Fluids, 1997.
- [81] M.D. Graham, Microhydrodynamics, Brownian Motion, and Complex Fluids, Cambridge University Press, Cambridge, 2018.
- [82] K. Joyner, S. Yang, G.A. Duncan, Microrheology for biomaterial design, *APL Bioengineering* 4(4) (2020) 041508.
- [83] N.D. Schnellbacher, U.S. Schwarz, The power of a single trajectory, *New Journal of Physics* 20(3) (2018) 031001.
- [84] T. Kuhn, J. Hettich, R. Davtyan, J.C.M. Gebhardt, Single molecule tracking and analysis framework including theory-predicted parameter settings, *Scientific Reports* 11(1) (2021) 9465.
- [85] E. Barkai, Y. Garini, R. Metzler, Strange kinetics of single molecules in living cells, *Physics Today* 65(8) (2012) 29-35.
- [86] X. Bian, C. Kim, G.E. Karniadakis, 111 years of Brownian motion, *Soft Matter* 12(30) (2016) 6331-6346.
- [87] T. Savin, P.S. Doyle, Static and Dynamic Errors in Particle Tracking Microrheology, *Biophysical Journal* 88(1) (2005) 623-638.
- [88] K.M. Schultz, E.M. Furst, Microrheology of biomaterial hydrogelators, *Soft Matter* 8(23) (2012) 6198-6205.

- [89] A. Kowalczyk, C. Oelschlaeger, N. Willenbacher, Tracking errors in 2D multiple particle tracking microrheology, *Measurement Science and Technology* 26(1) (2014) 015302.
- [90] I. Cohen, D. Weihs, Rheology and microrheology of natural and reduced-calorie Israeli honeys as a model for high-viscosity Newtonian liquids, *Journal of Food Engineering* 100(2) (2010) 366-371.
- [91] R. Conroy, Force Spectroscopy with Optical and Magnetic Tweezers, in: A. Noy (Ed.), *Handbook of Molecular Force Spectroscopy*, Springer US, Boston, MA, 2008, pp. 23-96.
- [92] M. Tassieri, T.A. Waigh, J. Trinick, A. Aggeli, R.M.L. Evans, Analysis of the linear viscoelasticity of polyelectrolytes by magnetic microrheometry—Pulsed creep experiments and the one particle response, *Journal of Rheology* 54(1) (2010) 117-131.
- [93] H. Lee, Y. Shin, S.T. Kim, E.L. Reinherz, M.J. Lang, Stochastic optical active rheology, *Applied Physics Letters* 101(3) (2012) 031902.
- [94] J.T. Park, G. Paneru, C. Kwon, S. Granick, H.K. Pak, Rapid-prototyping a Brownian particle in an active bath, *Soft Matter* (2020).
- [95] P. Kollmannsberger, B. Fabry, High-force magnetic tweezers with force feedback for biological applications, *Review of Scientific Instruments* 78(11) (2007).
- [96] F.S. Gnesotto, F. Mura, J. Gladrow, C.P. Broedersz, Broken detailed balance and non-equilibrium dynamics in living systems: a review, *Reports on Progress in Physics* 81(6) (2018) 066601.
- [97] M.A. Fernandez-Rodriguez, F. Grillo, L. Alvarez, M. Rathlef, I. Buttinoni, G. Volpe, L. Isa, Feedback-controlled active brownian colloids with space-dependent rotational dynamics, *Nature Communications* 11(1) (2020) 4223.
- [98] R. Wüstneck, J. Perez-Gil, N. Wüstneck, A. Cruz, V.B. Fainerman, U. Pison, Interfacial properties of pulmonary surfactant layers, *Advances in Colloid and Interface Science* 117(1) (2005) 33-58.
- [99] P.A. Ruhs, L. Boni, G.G. Fuller, R.F. Inglis, P. Fischer, In-situ quantification of the interfacial rheological response of bacterial biofilms to environmental stimuli, *PLoS One* 8(11) (2013) e78524.
- [100] E.R. Catapano, L.R. Arriaga, G. Espinosa, F. Monroy, D. Langevin, I. López-Montero, Solid character of membrane ceramides: a surface rheology study of their mixtures with sphingomyelin, *Biophysical journal* 101(11) (2011) 2721-2730.
- [101] H. Jin, F. Jiao, M.D. Daily, Y. Chen, F. Yan, Y.-H. Ding, X. Zhang, E.J. Robertson, M.D. Baer, C.-L. Chen, Highly stable and self-repairing membrane-mimetic 2D nanomaterials assembled from lipid-like peptoids, *Nature communications* 7 (2016) 12252-12252.

- [102] J.H.J. Thijssen, J. Vermant, Interfacial rheology of model particles at liquid interfaces and its relation to (bicontinuous) Pickering emulsions, *Journal of Physics: Condensed Matter* 30(2) (2017) 023002.
- [103] J.M. Rodríguez Patino, C. Carrera Sánchez, M.R. Rodríguez Niño, Implications of interfacial characteristics of food foaming agents in foam formulations, *Advances in Colloid and Interface Science* 140(2) (2008) 95-113.
- [104] B.S. Murray, Interfacial rheology of food emulsifiers and proteins, *Current Opinion in Colloid & Interface Science* 7(5) (2002) 426-431.
- [105] G. Narsimhan, Characterization of Interfacial Rheology of Protein-Stabilized Air-Liquid Interfaces, *Food Engineering Reviews* 8(3) (2016) 367-392.
- [106] J. Krägel, S.R. Derkach, Interfacial shear rheology, *Current Opinion in Colloid & Interface Science* 15(4) (2010) 246-255.
- [107] R. McGorty, J. Fung, D. Kaz, V.N. Manoharan, Colloidal self-assembly at an interface, *Materials Today* 13(6) (2010) 34-42.
- [108] N. Ballard, A.D. Law, S.A.F. Bon, Colloidal particles at fluid interfaces: behaviour of isolated particles, *Soft Matter* 15(6) (2019) 1186-1199.
- [109] S. Barman, G.F. Christopher, Simultaneous Interfacial Rheology and Microstructure Measurement of Densely Aggregated Particle Laden Interfaces Using a Modified Double Wall Ring Interfacial Rheometer, *Langmuir* 30(32) (2014) 9752-9760.
- [110] T. Li, K. Lilja, R.J. Morris, G.B. Brandani, Langmuir-Blodgett technique for anisotropic colloids: Young investigator perspective, *Journal of Colloid and Interface Science* 540 (2019) 420-438.
- [111] S. Razavi, B. Lin, K.Y.C. Lee, R.S. Tu, I. Kretzschmar, Impact of Surface Amphiphilicity on the Interfacial Behavior of Janus Particle Layers under Compression, *Langmuir* 35(48) (2019) 15813-15824.
- [112] A.J. Mendoza, E. Guzmán, F. Martínez-Pedrero, H. Ritacco, R.G. Rubio, F. Ortega, V.M. Starov, R. Miller, Particle laden fluid interfaces: Dynamics and interfacial rheology, *Advances in Colloid and Interface Science* 206 (2014) 303-319.
- [113] A. Maestro, D. Jones, C. Sánchez de Rojas Candela, E. Guzman, M.H.G. Duits, P. Cicuti, Tuning Interfacial Properties and Processes by Controlling the Rheology and Structure of Poly(N-isopropylacrylamide) Particles at Air/Water Interfaces, *Langmuir* 34(24) (2018) 7067-7076.
- [114] E. Guzmán, J. Tajuelo, J.M. Pastor, M.Á. Rubio, F. Ortega, R.G. Rubio, Shear rheology of fluid interfaces: Closing the gap between macro- and micro-rheology, *Current Opinion in Colloid & Interface Science* 37 (2018) 33-48.

- [115] M. Karbaschi, M. Lotfi, J. Krägel, A. Javadi, D. Bastani, R. Miller, Rheology of interfacial layers, *Current Opinion in Colloid & Interface Science* 19(6) (2014) 514-519.
- [116] L.M.C. Sagis, P. Fischer, Nonlinear rheology of complex fluid–fluid interfaces, *Current Opinion in Colloid & Interface Science* 19(6) (2014) 520-529.
- [117] K. Kim, S.Q. Choi, Z.A. Zell, T.M. Squires, J.A. Zasadzinski, Effect of cholesterol nanodomains on monolayer morphology and dynamics, *Proceedings of the National Academy of Sciences of the United States of America* 110(33) (2013) E3054-60.
- [118] I. Buttinoni, Z.A. Zell, T.M. Squires, L. Isa, Colloidal binary mixtures at fluid–fluid interfaces under steady shear: structural, dynamical and mechanical response, *Soft Matter* 11(42) (2015) 8313-8321.
- [119] D. Truzzolillo, H. Sharaf, U. Jonas, B. Loppinet, D. Vlassopoulos, Tuning the Structure and Rheology of Polystyrene Particles at the Air–Water Interface by Varying the pH, *Langmuir* 32(27) (2016) 6956-6966.
- [120] S. Barman, G.F. Christopher, Role of capillarity and microstructure on interfacial viscoelasticity of particle laden interfaces, *Journal of Rheology* 60(1) (2015) 35-45.
- [121] Y.-J. Lin, S. Barman, P. He, Z. Zhang, G.F. Christopher, S.L. Biswal, Combined interfacial shear rheology and microstructure visualization of asphaltenes at air-water and oil-water interfaces, *Journal of Rheology* 62(1) (2018) 1-10.
- [122] M. Molaei, J.C. Crocker, Interfacial microrheology and tensiometry in a miniature, 3-d printed Langmuir trough, *Journal of Colloid and Interface Science* 560 (2020) 407-415.
- [123] J. Yang, K. Yu, T. Tsuji, R. Jha, Y.Y. Zuo, Determining the surface dilational rheology of surfactant and protein films with a droplet waveform generator, *Journal of Colloid and Interface Science* 537 (2019) 547-553.
- [124] B.A. Noskov, M.M. Krycki, Formation of protein/surfactant adsorption layer as studied by dilational surface rheology, *Advances in Colloid and Interface Science* 247 (2017) 81-99.
- [125] T. Morioka, M. Kawaguchi, Surface dilational moduli of polymer and blended polymer monolayers spread at air-water interfaces, *Advances in Colloid and Interface Science* 214 (2014) 1-16.
- [126] B.A. Noskov, G. Loglio, R. Miller, Dilational surface visco-elasticity of polyelectrolyte/surfactant solutions: Formation of heterogeneous adsorption layers, *Advances in Colloid and Interface Science* 168(1) (2011) 179-197.
- [127] A.P. Kotula, S.L. Anna, Regular perturbation analysis of small amplitude oscillatory dilatation of an interface in a capillary pressure tensiometer, *Journal of Rheology* 59(1) (2015) 85-117.

- [128] A. Torcello-Gómez, M. Wulff-Pérez, M.J. Gálvez-Ruiz, A. Martín-Rodríguez, M. Cabrerizo-Vílchez, J. Maldonado-Valderrama, Block copolymers at interfaces: Interactions with physiological media, *Advances in Colloid and Interface Science* 206 (2014) 414-427.
- [129] J. Maldonado-Valderrama, J.M.R. Patino, Interfacial rheology of protein–surfactant mixtures, *Current Opinion in Colloid & Interface Science* 15(4) (2010) 271-282.
- [130] B.S. Murray, Rheological properties of protein films, *Current Opinion in Colloid & Interface Science* 16(1) (2011) 27-35.
- [131] D. Langevin, F. Monroy, Interfacial rheology of polyelectrolytes and polymer monolayers at the air–water interface, *Current Opinion in Colloid & Interface Science* 15(4) (2010) 283-293.
- [132] G.L. Lin, J.A. Pathak, D.H. Kim, M. Carlson, V. Riguero, Y.J. Kim, J.S. Buff, G.G. Fuller, Interfacial dilatational deformation accelerates particle formation in monoclonal antibody solutions, *Soft Matter* 12(14) (2016) 3293-3302.
- [133] S. Amin, G.V. Barnett, J.A. Pathak, C.J. Roberts, P.S. Sarangapani, Protein aggregation, particle formation, characterization & rheology, *Current Opinion in Colloid & Interface Science* 19(5) (2014) 438-449.
- [134] J.S. Bee, D.K. Schwartz, S. Trabelsi, E. Freund, J.L. Stevenson, J.F. Carpenter, T.W. Randolph, Production of particles of therapeutic proteins at the air–water interface during compression/dilation cycles, *Soft Matter* 8(40) (2012) 10329-10335.
- [135] M. Nagel, T.A. Tervoort, J. Vermant, From drop-shape analysis to stress-fitting elastometry, *Advances in Colloid and Interface Science* 247 (2017) 33-51.
- [136] B.M. Abraham, K. Miyano, S.Q. Xu, J.B. Ketterson, Centro-symmetric technique for measuring shear modulus, viscosity, and surface tension of spread monolayers, *Review of Scientific Instruments* 54(2) (1983) 213-219.
- [137] J.J. Kokelaar, A. Prins, M. De Gee, A new method for measuring the surface dilational modulus of a liquid, *Journal of Colloid and Interface Science* 146(2) (1991) 507-511.
- [138] M. Matsumoto, Y. Tsujii, K.-I. Nakamura, T. Yoshimoto, A trough with radial compression for studies of monolayers and fabrication of Langmuir-Blodgett films, *Thin Solid Films* 280(1) (1996) 238-243.
- [139] O. Senkel, R. Miller, V.B. Fainerman, Compression and expansion of surfactant adsorption layers at the liquid/air interface studied by a glass funnel method, *Colloids and Surfaces A: Physicochemical and Engineering Aspects* 178(1) (2001) 49-56.
- [140] K. Miyano, T. Maeda, Langmuir trough with four movable barriers, *Review of Scientific Instruments* 58(3) (1987) 428-435.
- [141] T.M. Bohanon, A.M. Lee, J.B. Ketterson, P. Dutta, Surface tension anisotropy and relaxation in uniaxially compressed Langmuir monolayers, *Langmuir* 8(10) (1992) 2497-2500.

- [142] A.K. Sachan, J.A. Zasadzinski, Interfacial curvature effects on the monolayer morphology and dynamics of a clinical lung surfactant, *Proceedings of the National Academy of Sciences of the United States of America* 115(2) (2018) E134-e143.
- [143] S.E.H.J. van Kempen, H.A. Schols, E. van der Linden, L.M.C. Sagis, Non-linear surface dilatational rheology as a tool for understanding microstructures of air/water interfaces stabilized by oligofructose fatty acid esters, *Soft Matter* 9(40) (2013) 9579-9592.
- [144] A. Holm, C.J. Wrasman, K.-C. Kao, A.R. Riscoe, M. Cagnello, C.W. Frank, Langmuir–Blodgett Deposition of Graphene Oxide—Identifying Marangoni Flow as a Process that Fundamentally Limits Deposition Control, *Langmuir* 34(33) (2018) 9683-9691.
- [145] A.-C. Schöne, T. Roch, B. Schulz, A. Lendlein, Evaluating polymeric biomaterial–environment interfaces by Langmuir monolayer techniques, *Journal of The Royal Society Interface* 14(130) (2017) 20161028.
- [146] Y.Y. Zuo, R. Chen, X. Wang, J. Yang, Z. Policova, A.W. Neumann, Phase Transitions in Dipalmitoylphosphatidylcholine Monolayers, *Langmuir* 32(33) (2016) 8501-8506.
- [147] D.M. Goggin, J.R. Samaniuk, Dynamics of pristine graphite and graphene at an air-water interface, *AIChE Journal* 64(8) (2018) 3177-3187.
- [148] B.C. Allen, B.E. Sturgeon, A.G. Sostarecz, Brewster Angle Microscopy and Langmuir Monolayer Films: Construction of an Instrument and Basic Software Development for Visualization of Lipid Domains and Lipid Raft Formation, *The FASEB Journal* 32(1_supplement) (2018) 541.3-541.3.
- [149] W. Daear, M. Mahadeo, E.J. Prenner, Applications of Brewster angle microscopy from biological materials to biological systems, *Biochimica et Biophysica Acta (BBA) - Biomembranes* 1859(10) (2017) 1749-1766.
- [150] Z. Sun, D. Zheng, S. Baldelli, Distortion Correction for a Brewster Angle Microscope Using an Optical Grating, *Analytical Chemistry* 89(4) (2017) 2186-2190.
- [151] Y.-K. See, J. Cha, T. Chang, M. Ree, Glass Transition Temperature of Poly(tert-butyl methacrylate) Langmuir–Blodgett Film and Spin-Coated Film by X-ray Reflectivity and Ellipsometry, *Langmuir* 16(5) (2000) 2351-2355.
- [152] A. Maestro, L.J. Bonales, H. Ritacco, T.M. Fischer, R.G. Rubio, F. Ortega, Surface rheology: macro- and microrheology of poly(tert-butyl acrylate) monolayers, *Soft Matter* 7(17) (2011) 7761-7771.
- [153] T.J. Joncheray, S.A. Bernard, R. Matmour, B. Lepoittevin, R.J. El-Khoury, D. Taton, Y. Gnanou, R.S. Duran, Polystyrene-b-poly(tert-butyl acrylate) and polystyrene-b-poly(acrylic acid) dendrimer-like copolymers: two-dimensional self-assembly at the air-water interface, *Langmuir* 23(5) (2007) 2531-8.

- [154] G.T. Gavranovic, J.M. Deutsch, G.G. Fuller, Two-Dimensional Melts: Polymer Chains at the Air–Water Interface, *Macromolecules* 38(15) (2005) 6672-6679.
- [155] G. Ma, H.C. Allen, DPPC Langmuir Monolayer at the Air–Water Interface: Probing the Tail and Head Groups by Vibrational Sum Frequency Generation Spectroscopy, *Langmuir* 22(12) (2006) 5341-5349.
- [156] E.J.A. Veldhuizen, H.P. Haagsman, Role of pulmonary surfactant components in surface film formation and dynamics, *Biochimica et Biophysica Acta (BBA) - Biomembranes* 1467(2) (2000) 255-270.
- [157] W. Bernhard, Lung surfactant: Function and composition in the context of development and respiratory physiology, *Annals of anatomy = Anatomischer Anzeiger : official organ of the Anatomische Gesellschaft* 208 (2016) 146-150.
- [158] M. Chakraborty, S. Kotecha, Pulmonary surfactant in newborn infants and children, *Breathe* 9(6) (2013) 476-488.
- [159] R. Wüstneck, N. Wüstneck, B. Moser, U. Pison, Surface Dilatational Behavior of Pulmonary Surfactant Components Spread on the Surface of a Pendant Drop. 2. Dipalmitoyl Phosphatidylcholine and Surfactant Protein B, *Langmuir* 18(4) (2002) 1125-1130.
- [160] R. Pichot, R.L. Watson, I.T. Norton, Phospholipids at the Interface: Current Trends and Challenges, *International Journal of Molecular Sciences* 14(6) (2013) 11767-11794.
- [161] L. Imperiali, K.-H. Liao, C. Clasen, J. Fransaer, C.W. Macosko, J. Vermant, Interfacial Rheology and Structure of Tiled Graphene Oxide Sheets, *Langmuir* 28(21) (2012) 7990-8000.
- [162] A.R. Esker, C. Mengel, G. Wegner, Ultrathin Films of a Polyelectrolyte with Layered Architecture, *Science (New York, N.Y.)* 280(5365) (1998) 892-895.
- [163] A. Ładniak, M. Jurak, A.E. Wiącek, Langmuir monolayer study of phospholipid DPPC on the titanium dioxide–chitosan–hyaluronic acid subphases, *Adsorption* 25(3) (2019) 469-476.
- [164] M.V. Meli, I.H. Lin, N.L. Abbott, Preparation of microscopic and planar oil-water interfaces that are decorated with prescribed densities of insoluble amphiphiles, *Journal of the American Chemical Society* 130(13) (2008) 4326-33.
- [165] M.R. Rodríguez Niño, A. Lucero, J.M. Rodríguez Patino, Relaxation phenomena in phospholipid monolayers at the air–water interface, *Colloids and Surfaces A: Physicochemical and Engineering Aspects* 320(1) (2008) 260-270.
- [166] N. Wüstneck, R. Wüstneck, V.B. Fainerman, U. Pison, R. Miller, Investigation of over-compressed spread l-dipalmitoyl phosphatidylcholine films and the influence of solvent vapour in the gas phase on Π/A isotherms measured by using the captive bubble technique, *Colloids and Surfaces A: Physicochemical and Engineering Aspects* 164(2) (2000) 267-278.

- [167] Y.Y. Zuo, R. Chen, X. Wang, J. Yang, Z. Policova, A.W. Neumann, Phase Transitions in Dipalmitoylphosphatidylcholine Monolayers, *Langmuir : the ACS journal of surfaces and colloids* 32(33) (2016) 8501-8506.
- [168] S.L. Duncan, R.G. Larson, Comparing experimental and simulated pressure-area isotherms for DPPC, *Biophysical journal* 94(8) (2008) 2965-2986.
- [169] J.M. Rodríguez Patino, A.L. Caro, M.R. Rodríguez Niño, A.R. Mackie, A.P. Gunning, V.J. Morris, Some implications of nanoscience in food dispersion formulations containing phospholipids as emulsifiers, *Food Chemistry* 102(2) (2007) 532-541.
- [170] J.B. Li, R. Miller, D. Vollhardt, G. Weidemann, H. Möhwald, Isotherms of phospholipid monolayers measured by a pendant drop technique, *Colloid and Polymer Science* 274(10) (1996) 995-999.
- [171] S.M.I. Saad, Z. Policova, E.J. Acosta, M.L. Hair, A.W. Neumann, Mixed DPPC/DPPG Monolayers at Very High Film Compression, *Langmuir* 25(18) (2009) 10907-10912.
- [172] A. Jyoti, R.M. Prokop, A.W. Neumann, Manifestation of the liquid-expanded/liquid-condensed phase transition of a dipalmitoylphosphatidylcholine monolayer at the air-water interface, *Colloids and Surfaces B: Biointerfaces* 8(3) (1997) 115-124.
- [173] J. Li, R. Miller, H. Möhwald, Characterisation of phospholipid layers at liquid interfaces 2. Comparison of isotherms of insoluble and soluble films of phospholipids at different fluid/water interfaces, *Colloids and Surfaces A: Physicochemical and Engineering Aspects* 114 (1996) 123-130.
- [174] A. Jyoti, R.M. Prokop, J. Li, D. Vollhardt, D.Y. Kwok, R. Miller, H. Möhwald, A.W. Neumann, An investigation of the compression rate dependence on the surface pressure-surface area isotherm for a dipalmitoyl phosphatidylcholine monolayer at the air/water interface, *Colloids and Surfaces A: Physicochemical and Engineering Aspects* 116(1) (1996) 173-180.
- [175] N. Anton, P. Pierrat, L. Lebeau, T.F. Vandamme, P. Bouriat, A study of insoluble monolayers by deposition at a bubble interface, *Soft Matter* 9(42) (2013) 10081-10091.
- [176] M.J. Skaug, M.L. Longo, R. Faller, The Impact of Texas Red on Lipid Bilayer Properties, *The Journal of Physical Chemistry B* 115(26) (2011) 8500-8505.
- [177] H.M. McConnell, L.K. Tamm, R.M. Weis, Periodic structures in lipid monolayer phase transitions, *Proceedings of the National Academy of Sciences of the United States of America* 81(10) (1984) 3249-3253.
- [178] S. Baoukina, L. Monticelli, H.J. Risselada, S.J. Marrink, D.P. Tieleman, The molecular mechanism of lipid monolayer collapse, *Proceedings of the National Academy of Sciences* 105(31) (2008) 10803-10808.
- [179] H.M. McConnell, Structures and Transitions in Lipid Monolayers at the Air-Water Interface, *Annual Review of Physical Chemistry* 42(1) (1991) 171-195.

- [180] G. Caminati, S. Cicchi, L. Lascialfari, A. Brandi, Separation of Enantiomers of a Phospholipid in Langmuir Monolayers by a New Selector, *Chirality* 27(11) (2015) 784-787.
- [181] D. Vollhardt, N. Nandi, S.D. Banik, Nanoaggregate shapes at the air/water interface, *Physical Chemistry Chemical Physics* 13(11) (2011) 4812-4829.
- [182] K. Kim, S.Q. Choi, J.A. Zasadzinski, T.M. Squires, Nonlinear chiral rheology of phospholipid monolayers, *Soft Matter* 14(13) (2018) 2476-2483.
- [183] O.D. Velev, N.D. Denkov, V.N. Paunov, P.A. Kralchevsky, K. Nagayama, Direct measurement of lateral capillary forces, *Langmuir* 9(12) (1993) 3702-3709.
- [184] B.E. Rapp, Chapter 21 - Capillarity, in: B.E. Rapp (Ed.), *Microfluidics: Modelling, Mechanics and Mathematics*, Elsevier, Oxford, 2017, pp. 445-451.
- [185] Z.A. Zell, S.Q. Choi, L.G. Leal, T.M. Squires, Microfabricated deflection tensiometers for insoluble surfactants, *Applied Physics Letters* 97(13) (2010) 133505.
- [186] Y. Hu, K.Y.C. Lee, J. Israelachvili, Sealed Minitrough for Microscopy and Long-Term Stability Studies of Langmuir Monolayers, *Langmuir* 19(1) (2003) 100-104.
- [187] B. Madivala, J. Fransaer, J. Vermant, Self-Assembly and Rheology of Ellipsoidal Particles at Interfaces, *Langmuir* 25(5) (2009) 2718-2728.
- [188] L. Wu, X. Wang, G. Wang, G. Chen, In situ X-ray scattering observation of two-dimensional interfacial colloidal crystallization, *Nature Communications* 9(1) (2018) 1335.
- [189] M. Wang, A.M. Mihut, E. Rieloff, A.P. Dabkowska, L.K. Månsson, J.N. Immink, E. Sparr, J.J. Crassous, Assembling responsive microgels at responsive lipid membranes, *Proceedings of the National Academy of Sciences of the United States of America* 116(12) (2019) 5442-5450.
- [190] B.A. Noskov, Dilational surface rheology of polymer and polymer/surfactant solutions, *Current Opinion in Colloid & Interface Science* 15(4) (2010) 229-236.
- [191] P. Fischer, P. Erni, Emulsion drops in external flow fields — The role of liquid interfaces, *Current Opinion in Colloid & Interface Science* 12(4) (2007) 196-205.
- [192] D. Langevin, Coalescence in foams and emulsions: Similarities and differences, *Current Opinion in Colloid & Interface Science* 44 (2019) 23-31.
- [193] B.A. Noskov, A.G. Bykov, Dilational rheology of monolayers of nano- and microparticles at the liquid-fluid interfaces, *Current Opinion in Colloid & Interface Science* 37 (2018) 1-12.
- [194] A. Kannan, I.C. Shieh, G.G. Fuller, Linking aggregation and interfacial properties in monoclonal antibody-surfactant formulations, *Journal of Colloid and Interface Science* 550 (2019) 128-138.

- [195] A. Kannan, I.C. Shieh, D.L. Leiske, G.G. Fuller, Monoclonal Antibody Interfaces: Dilatation Mechanics and Bubble Coalescence, *Langmuir* 34(2) (2018) 630-638.
- [196] J. Li, X. Wang, T. Zhang, C. Wang, Z. Huang, X. Luo, Y. Deng, A review on phospholipids and their main applications in drug delivery systems, *Asian Journal of Pharmaceutical Sciences* 10(2) (2015) 81-98.
- [197] P. van Hoogevest, A. Wendel, The use of natural and synthetic phospholipids as pharmaceutical excipients, *Eur J Lipid Sci Technol* 116(9) (2014) 1088-1107.
- [198] R.P. Singh, H.V. Gangadharappa, K. Mruthunjaya, Phospholipids: Unique carriers for drug delivery systems, *Journal of Drug Delivery Science and Technology* 39 (2017) 166-179.
- [199] A. Ahmad, H. Ahsan, Lipid-based formulations in cosmeceuticals and biopharmaceuticals, *Biomedical Dermatology* 4(1) (2020) 12.
- [200] L. Cui, E.A. Decker, Phospholipids in foods: prooxidants or antioxidants?, *Journal of the Science of Food and Agriculture* 96(1) (2016) 18-31.
- [201] K. Sehlmeier, J. Ruwisch, N. Roldan, E. Lopez-Rodriguez, Alveolar Dynamics and Beyond - The Importance of Surfactant Protein C and Cholesterol in Lung Homeostasis and Fibrosis, *Frontiers in physiology* 11 (2020) 386.
- [202] M. Chakraborty, S. Kotecha, Pulmonary Surfactant in Newborn Infants and Children – A Review, 2013.
- [203] E. Hermans, M. Saad Bhamla, P. Kao, G.G. Fuller, J. Vermant, Lung surfactants and different contributions to thin film stability, *Soft Matter* 11(41) (2015) 8048-8057.
- [204] C. Autilio, J. Pérez-Gil, Understanding the principle biophysics concepts of pulmonary surfactant in health and disease, *Archives of Disease in Childhood - Fetal and Neonatal Edition* 104(4) (2019) F443-F451.
- [205] S.K. Kale, A.J. Cope, D.M. Goggin, J.R. Samaniuk, A miniaturized radial Langmuir trough for simultaneous dilatational deformation and interfacial microscopy, *Journal of Colloid and Interface Science* 582 (2021) 1085-1098.
- [206] A. Maestro, E. Santini, D. Zabiegaj, S. Llamas, F. Ravera, L. Liggieri, F. Ortega, R.G. Rubio, E. Guzman, Particle and Particle-Surfactant Mixtures at Fluid Interfaces: Assembly, Morphology, and Rheological Description, *Advances in Condensed Matter Physics* 2015 (2015) 917516.
- [207] A. Lucero Caro, M.R. Rodríguez Niño, J.M. Rodríguez Patino, The effect of pH on surface dilatational and shear properties of phospholipid monolayers, *Colloids and Surfaces A: Physicochemical and Engineering Aspects* 327(1) (2008) 79-89.

- [208] A.J. Sheridan, J.M. Slater, T. Arnold, R.A. Campbell, K.C. Thompson, Changes to DPPC Domain Structure in the Presence of Carbon Nanoparticles, *Langmuir* 33(39) (2017) 10374-10384.
- [209] L. Xu, G. Bosiljevac, K. Yu, Y.Y. Zuo, Melting of the Dipalmitoylphosphatidylcholine Monolayer, *Langmuir* 34(15) (2018) 4688-4694.
- [210] E. Hermans, J. Vermant, Interfacial shear rheology of DPPC under physiologically relevant conditions, *Soft Matter* 10(1) (2014) 175-186.
- [211] F. Ravera, G. Loglio, V.I. Kovalchuk, Interfacial dilational rheology by oscillating bubble/drop methods, *Current Opinion in Colloid & Interface Science* 15(4) (2010) 217-228.
- [212] J.R. Samaniuk, J. Vermant, Small-amplitude oscillatory dilatational rheology at fluid-fluid interfaces using a Wilhelmy balance, 2017.
- [213] L. Chen, A. Offenhausser, H.J. Krause, Magnetic tweezers with high permeability electromagnets for fast actuation of magnetic beads, *The Review of scientific instruments* 86(4) (2015) 044701.
- [214] C.L. Ting, Z.-G. Wang, Interactions of a charged nanoparticle with a lipid membrane: implications for gene delivery, *Biophysical journal* 100(5) (2011) 1288-1297.
- [215] A.H.R. Koch, S. Morsbach, T. Bereau, G. Lévêque, H.-J. Butt, M. Deserno, K. Landfester, G. Fytas, Probing Nanoparticle/Membrane Interactions by Combining Amphiphilic Diblock Copolymer Assembly and Plasmonics, *The Journal of Physical Chemistry B* 124(5) (2020) 742-750.
- [216] H. Zhang, T. Fan, W. Chen, Y. Li, B. Wang, Recent advances of two-dimensional materials in smart drug delivery nano-systems, *Bioactive Materials* 5(4) (2020) 1071-1086.
- [217] Z. Xue, Q. Sun, L. Zhang, Z. Kang, L. Liang, Q. Wang, J.-W. Shen, Graphene quantum dot assisted translocation of drugs into a cell membrane, *Nanoscale* 11(10) (2019) 4503-4514.
- [218] M. Bramini, G. Alberini, E. Colombo, M. Chiacchiaretta, M.L. DiFrancesco, J.F. Maya-Vetencourt, L. Maragliano, F. Benfenati, F. Cesca, Interfacing Graphene-Based Materials With Neural Cells, *Frontiers in systems neuroscience* 12 (2018) 12.
- [219] P. Chen, H. Yue, X. Zhai, Z. Huang, G.-H. Ma, W. Wei, L.-T. Yan, Transport of a graphene nanosheet sandwiched inside cell membranes, *Science advances* 5(6) (2019) eaaw3192-eaaw3192.
- [220] D.M. Goggin, J.R. Samaniuk, 2D Colloids: Size- and Shape-Controlled 2D Materials at Fluid–Fluid Interfaces, *Langmuir* 37(48) (2021) 14157-14166.

APPENDIX A

SUPPLEMENTARY MATERIAL MAGNETIC TWEEZERS

A.1 Estimating the Cutoff Frequency

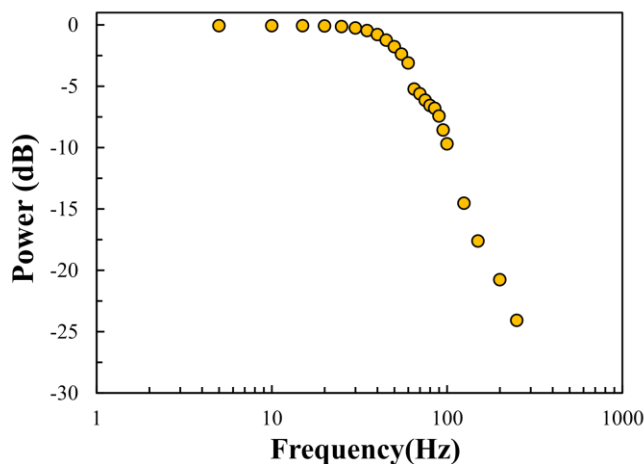


Figure A.1 Yellow circles show the power estimated for the electromagnetic coil as a function of frequency. Power is calculated from the amplitude ratio of a sine wave at 1A evaluated at various frequencies. The cutoff frequency is approximately 60Hz at -3dB. Based on this, the operational or usable signal frequency that is selected for this work is 25Hz.

A.2 MATLAB Algorithm for Randomizing ‘Directed’ Displacements

In the MATLAB code we have a track matrix (‘tr’) that that gives the position coordinates of every particle in pixels. For randomization, we first calculate displacements at lag frame 1 and call it ‘trTemp’. We randomize this trTemp matrix by multiplying each row by either ‘-1’ or ‘+1’. We ensure that each assignment of the directionality has equal probability, and each assignment is independent of the other. This is done using the ‘randi’ built-in function. After randomizing we re-build a new track matrix based on the randomized particle locations and call it as ‘trNew’. We then use this ‘trNew’ matrix to calculate displacements (‘Disp’) at every lag frame. Overall, this modification makes the displacements random with a Gaussian

distribution and a mean of zero. Further, the displacements are used to estimate the *MSD*. The detailed code to calculate displacement is given below.

```
function [Disp,tr] = Disp(tr);
```

```
%This series calculates displacements of each particle, for all lag times, and outputs a 4-column matrix, "Disp", containing those displacements. The first two columns contain x and y coordinate displacements respectively, the third column indicates the lag time associated with the displacement, and the fourth column indicates the particle number.
```

```
Disp has 4 columns: [x-displacement y-displacement lag-time Particle#]
```

```
i = 1; j = 1; u = 1;
```

```
[n,m] = size(tr); %find size of tr
```

```
tsteps = max(tr(:,3))-1; %find the number of time steps
```

```
%tsteps = max(tr(:,3)); %find the number of time steps
```

```
part = unique(tr(:,4)); %find particle numbers in tr
```

```
[p1 p2] = size(part); %p1 is the number of particles in tr
```

```
Counter = 1;
```

```
%% Randomizing the displacements at lag frame 1 and re-building a new track matrix
```

```
trTemp = zeros(tsteps,3); %%initialize trTemp
```

```
trNew = tr; %initialize trNew with tr as the 1st row of trNew will be same as tr
```

```
%This loop if consecutive frames are considered
```

```
a = 0; % Variable for assigning +ve/-ve values to displacements or trTemp (see if/else loop)
```

```
for i = 1:p1; %consider all particles
```

```
    i = part(i); %make i particle numbers, not just an index
```

```
    rows = find(tr(:,4)==i); %rows is vector of row numbers in "tr" that refer to paricle i
```

```
    for j = 1:tsteps; %for each particle consider each time step
```

```
        trTemp(rows(j),:) = [(tr(rows(j+1),[1 2])-tr(rows(j),[1 2])),j]; %take difference between consecutive rows for getting displacements at lag frame '1'
```

```
        a = randi([0,1],1,1);
```

```
        if a==0
```

```
            trTemp(rows(j),:) = [(trTemp(rows(j),[1,2]).*(-1)),j]; %make negative
```

```

else
    trTemp(rows(j,:),:) = [(trTemp(rows(j),[1,2]).*(1)),j]; %make positive
end

trNew(rows(j+1,:),) = [(trNew(rows(j),[1 2])+trTemp(rows(j),[1 2])),j+1,i];
end

end

%%Converting the new track matrix 'trNew' to a displacement matrix. Calculate randomized
displacement for all lag times.

tstepsNew = max(trNew(:,3))-1;
for u = 1:tstepsNew;
    for i = 1:p1;                %consider all particles
        i = part(i);           %make i particle numbers, not just an index
        rows = find(tr(:,4)==i); %rows is vector of row numbers in "tr" that refer to particle i
        for j = 1:u:(tstepsNew-(u-1)); %for each particle consider each time step
            %When using spacing of 'u' you can comment out initializing matrix 'Disp' in line 18
            Disp(Counter,:) = [(trNew(rows(j+u),[1 2])-trNew(rows(j),[1 2])),u,i]; %After tr
modification with random tracks
            Counter = Counter + 1;
        end
    end
end

end

end
end
end

```

A.3 Scanning Electron Microscopy (SEM) of Probe Particles

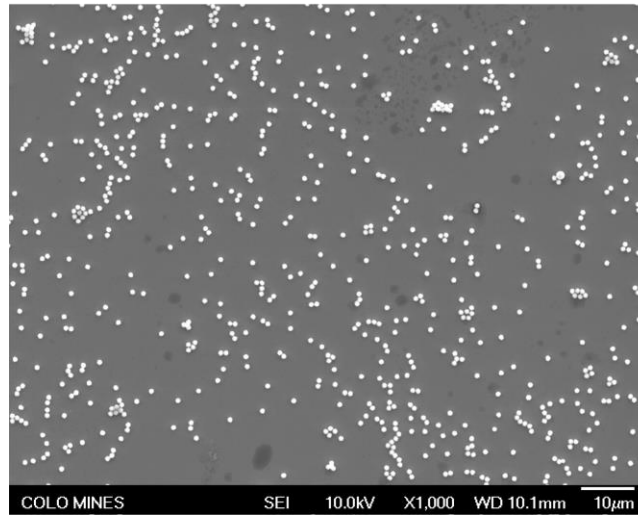


Figure A.2 SEM image of 1 μm diameter superparamagnetic probe particles.

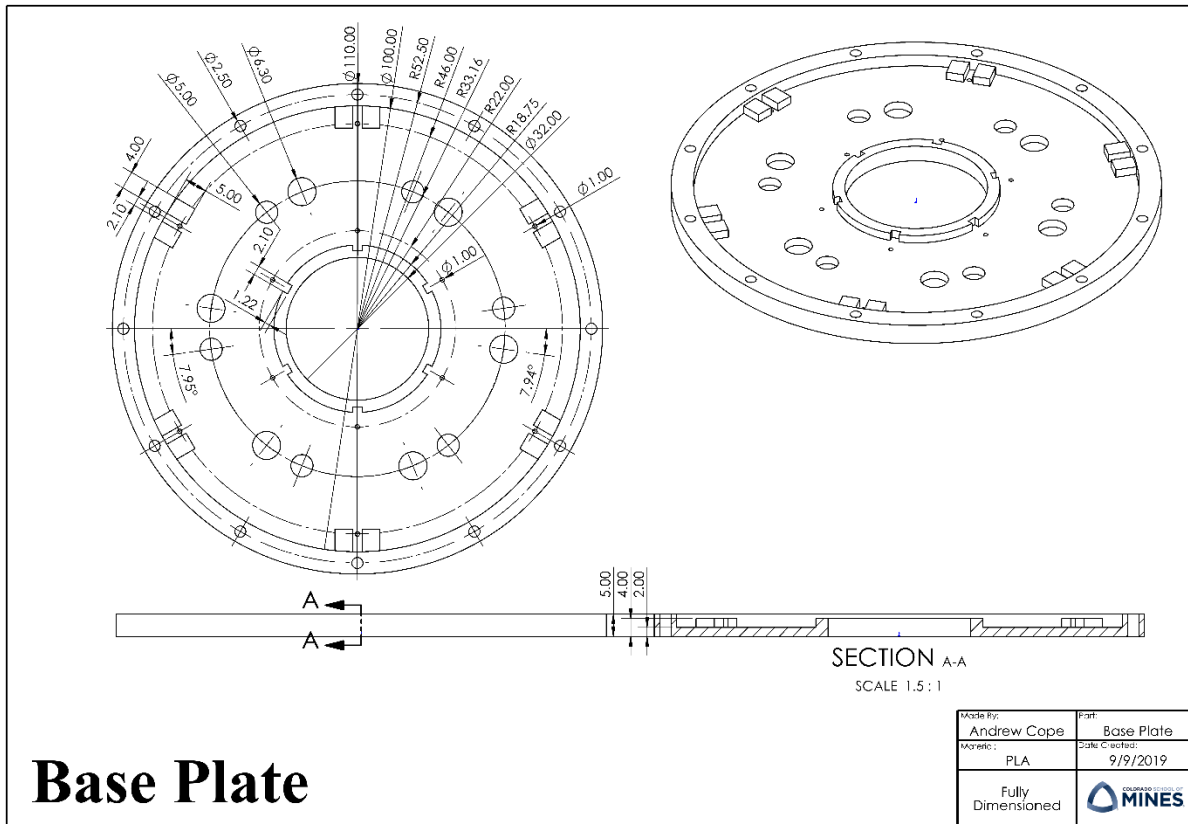
APPENDIX B

SUPPLEMENTARY MATERIAL RADIAL LANGMUIR TROUGH

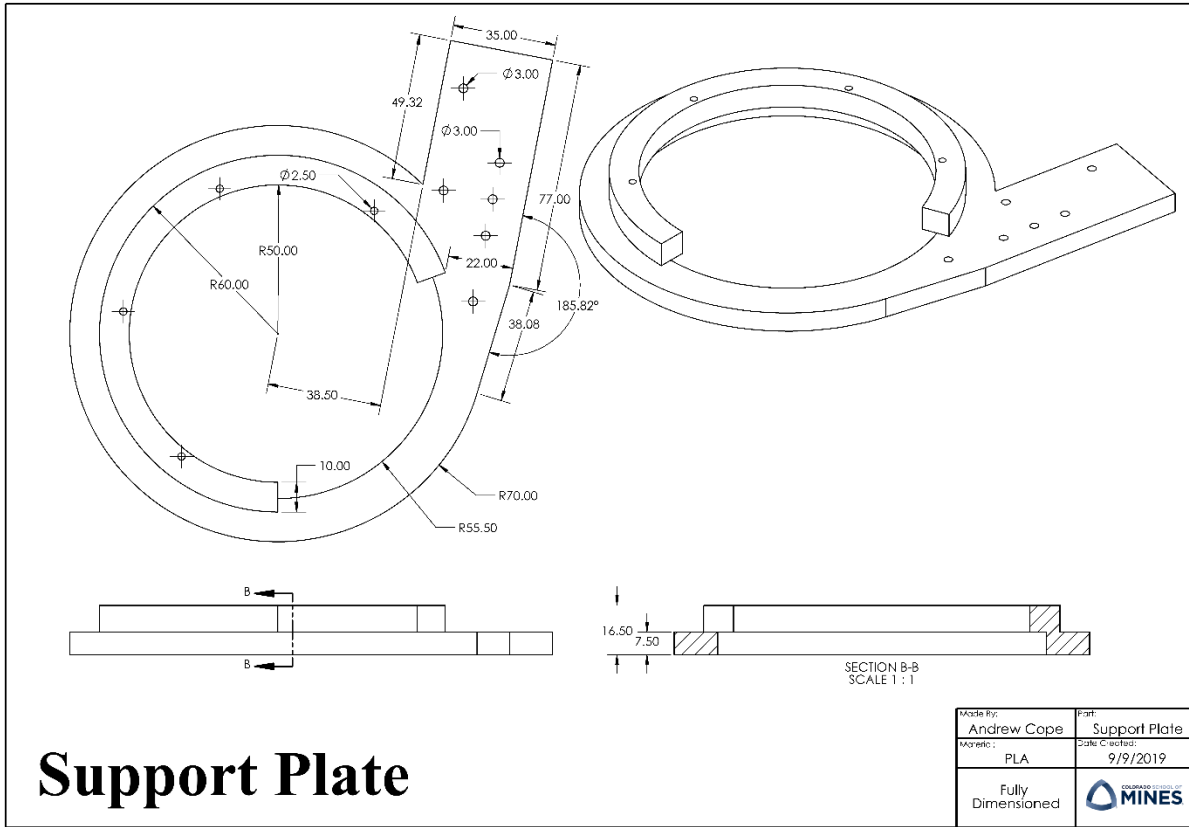
B.1 SolidWorks Drawings for the Radial Trough Parts

All dimensions are in 'mm'

Base Plate



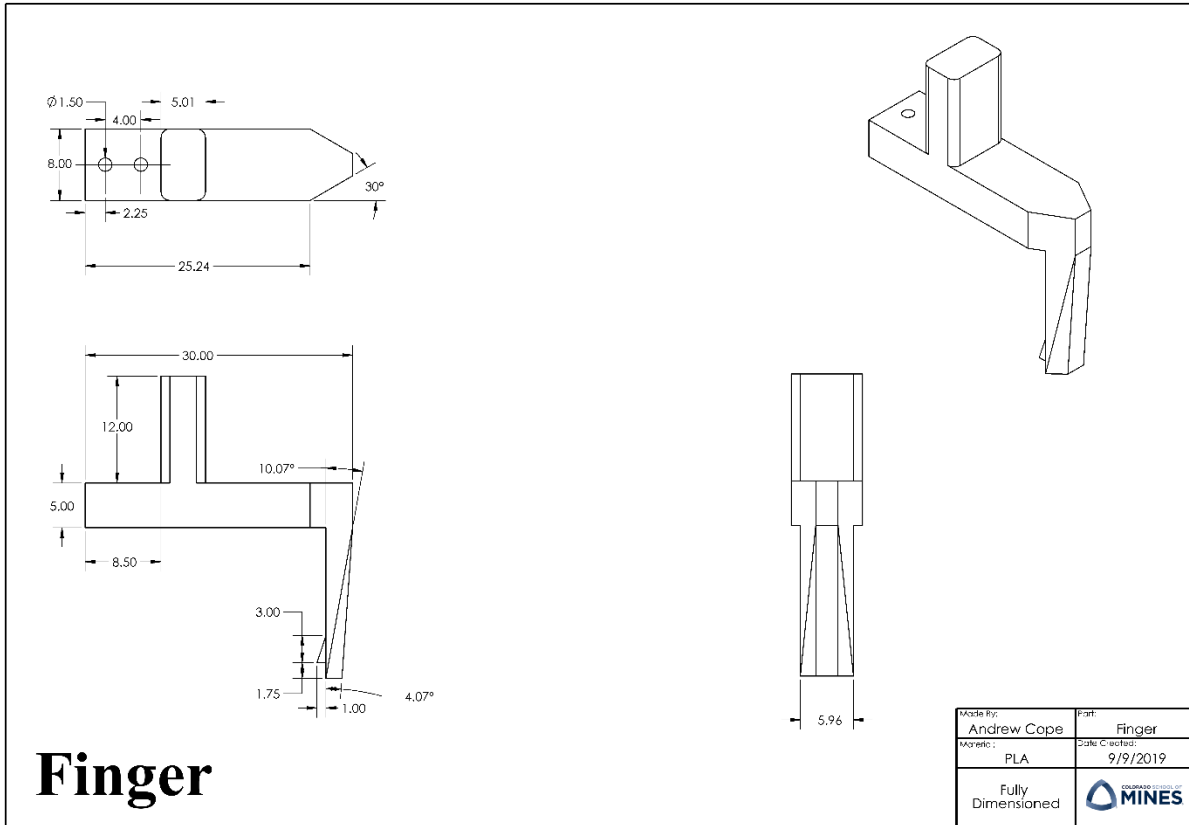
Support Plate



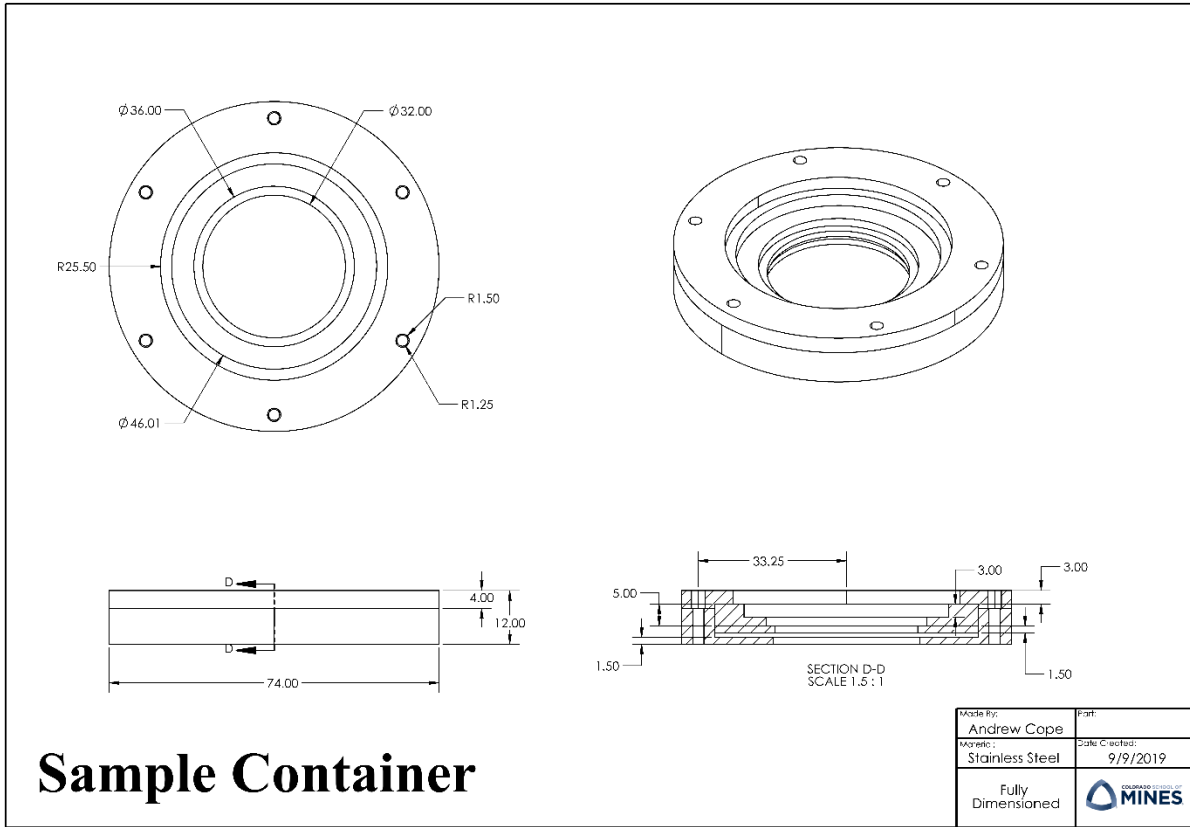
Support Plate

Made By: Andrew Cope	Part: Support Plate
Made In: PLA	Date Created: 9/9/2019
Fully Dimensioned	

Finger



Sample Container



B.2 Calibration and Interfacial Area Calculations

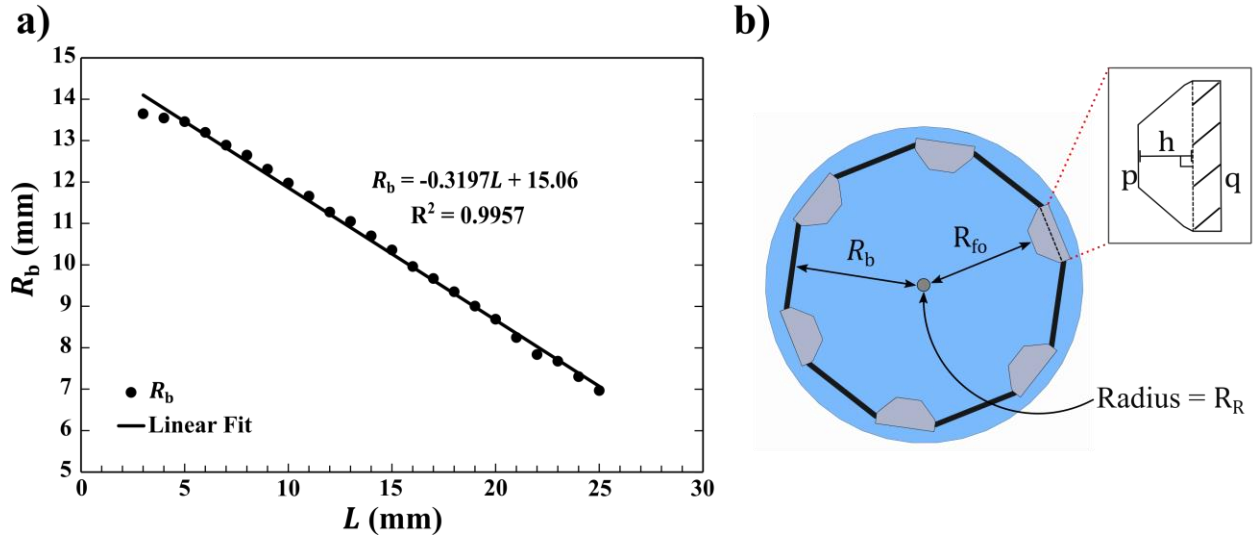


Figure B.1 a) Calibration curve for estimating radial distance, R_b , as a function of stepper-motor position, L for the radial Langmuir trough. b) Illustration of the top view of air-water interface in presence of platinum Wilhelmy rod. Inset is the magnification of finger-tip section that sits at the interface. The shaded region is occupied the elastic barrier.

The amount of material to be spread at air-water can be calculated from initial surface coverage value which requires the initial interfacial area evaluation. This initial area or the interfacial area at fully open trough configuration, A_0 , is approximated as circular region with radius R_b that is defined in Fig. B 1. Correction was made to this area by compensating the area lost by the six finger-tips and the Wilhelmy rod (if present). In presence of the Wilhelmy rod (radius $R_R = 0.5$ mm), this area was estimated according to the equation:

$$A_0 = \pi R_b^2 - 6 \left((p + q) \frac{h}{2} \right) - \pi R_R^2 \quad (\text{B.1})$$

The finger-tips have trapezoidal shape with height, h , and the parallel sides, p and q , and thus the area was calculated accordingly for all six fingers. In the visualization measurements, where the Wilhelmy rod was absent, only the first two terms on right hand side of the above equation were used to calculate A_0 . Using the above equation, value of A_0 turned out to be approximately 528.37 mm^2 . The value of R_b changes during the compression and it can be estimated based on the calibration curve provided in Fig. B1a. Consequently, the corresponding interfacial area can be evaluated using the same formula given above. At complete compression or fully closed trough with minimum area, A_{\min} , the compression ratio was $A_{\min}/A_0 \sim 5$.

B.3 Error Propagation

The error approximation in evaluating the mean monomer area for PtBMA and mean molecular area for DPPC is based on estimating the error in surface coverage, since conversion from surface coverage to monomer/molecular areas only involves constant values. Surface coverage error involves the error propagation in estimating sample concentration, trough area and sample volume deposited.

Surface coverage (S) = (Concentration of sample \times Volume of sample deposited) / Trough area

$$\text{Uncertainty in surface coverage } (\delta S) = S \times \sqrt{\left(\frac{\delta m}{m}\right)^2 + \left(\frac{\delta v}{v}\right)^2 + \left(\frac{\delta v_i}{v_i}\right)^2 + \left(\frac{\delta A_0}{A_0}\right)^2}$$

Where, m is the mass of the material, v is the volume of solvent used in making the sample and v_i is the volume of the spread deposited at the air-water interface. Terms with prefix δ represent the uncertainty in the respective measurement.

B.4 Dilute PtBMA Sample at Air-Water Interface

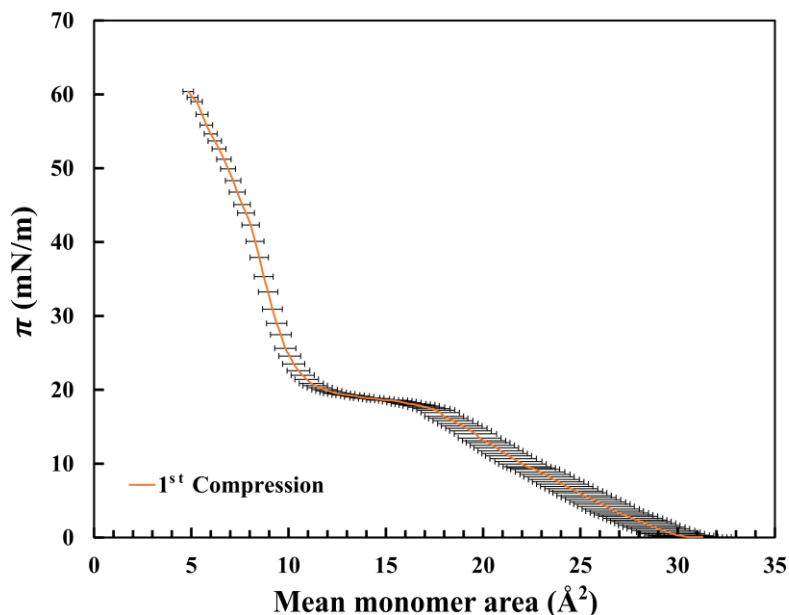


Figure B.2 Surface pressure (π) of compression curve with dilute PtBMA sample (ten times low concentration i.e., 0.02 mg/mL) and initial surface coverage of $\sim 0.75 \text{ mg/m}^2$ obtained using radial Langmuir trough. Error bars represent percentage uncertainty of 5.55% in estimating the mean monomer area. The curve does not show any apparent rise in π .

The result with dilute PtBMA sample does not show any apparent rise in π . Considering the large sample volume of the dilute sample, it was spread in the absence of the elastic barrier and the Wilhelmy probe. This was done because relatively large sample volumes were required of the dilute sample (on the order of 20 μL), and the suspending chloroform solvent can potentially interact with the elastic barrier prior to evaporation. In the absence of barrier, it is difficult to estimate the surface coverage accurately, because it is likely that once the barrier is introduced after solvent evaporation, some material may be present outside the enclosed barrier area. This leads to an untraceable error in estimating surface coverage. Therefore, we rely on using relatively concentrated samples and spread them in presence of Wilhelmy probe and the

barrier. Additionally, spreading the material inside the radial trough barrier area is more consistent to spreading in rectangular trough.

B.5 Reproducible DPPC Surface Pressure Measurement

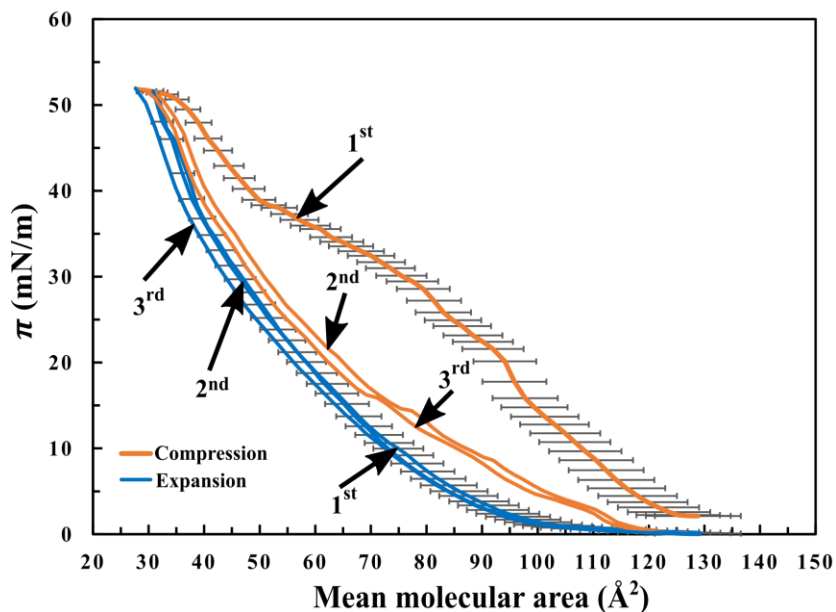


Figure B.3 Surface pressure (π) measurement of independently prepared DPPC at air-water interface obtained using radial Langmuir trough. Orange line data shows the consecutive compressions while blue line data shows the consecutive expansions. Arrows indicate the order of compression and expansion. Error bars represent percentage uncertainty of 6.05% in estimating the mean molecular area. For convenience error bars are only provided for first compression and expansion. Initial surface coverage is $\sim 0.75 \text{ mg/m}^2$.

The first compression curve shows an apparent rise in π . Next, there is a huge hysteresis between the first and the second compression curve. These two results are consistent with the observations made in Fig. 3.5a of Chapter 3. Note that the exact reproducibility of the magnitude of the apparent rise in π and the shape of the first curve is not guaranteed since these observations are an artifact of localized spreading. Moreover, the curves start at relatively higher mean molecular area than the curves obtained in Fig. 5a of main manuscript as the initial surface

coverages are different. The shape of the consecutive compression curves obtained here is reproducible when compared to the one obtained in Fig. 3.5a of Chapter 3. Additionally, the expansion curves are also reproducible (see expansion curves in this figure and expansion curve in Fig. B 5).

B.6 Dilute DPPC Sample at Air-Water Interface

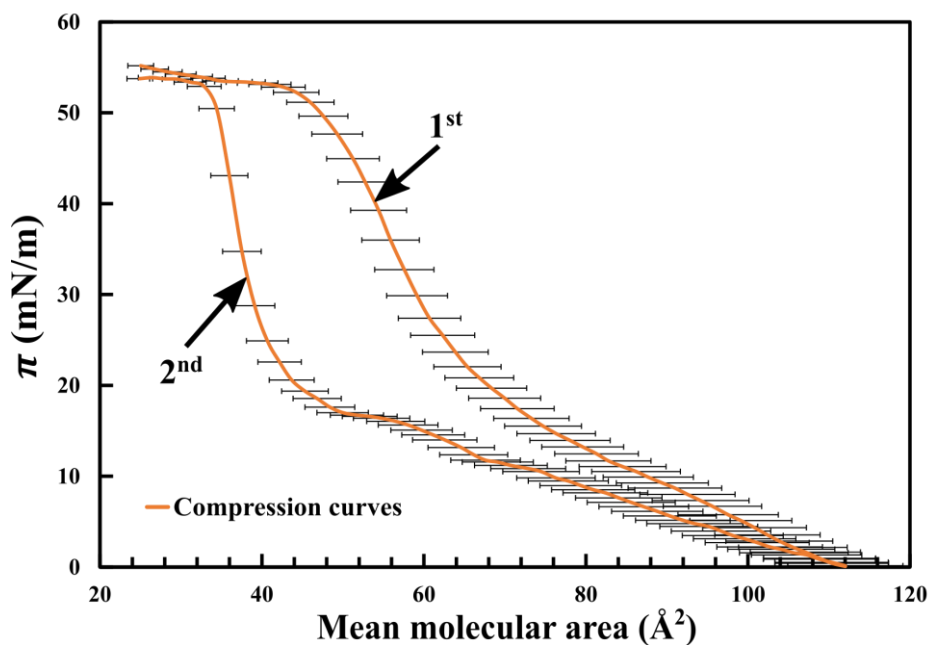


Figure B.4 Surface pressure (π) of first and second compression curves of dilute DPPC sample with ten times low concentration (0.02 mg/mL) and initial surface coverage of $\sim 1.1 \text{ mg/m}^2$ obtained using radial Langmuir trough. Error bars represent percentage uncertainty of 6.35% in estimating the mean molecular area. The curve does not show an apparent rise in π .

The result with the dilute DPPC sample does not show an apparent rise in beginning of the compression curve and there is significant hysteresis between the two curves. The spreading method is similar to the one explained with dilute PtBMA sample. Refer description in section B.4 above.

B.7 Reproducible Compression-Expansion Curves of Concentrated DPPC Sample

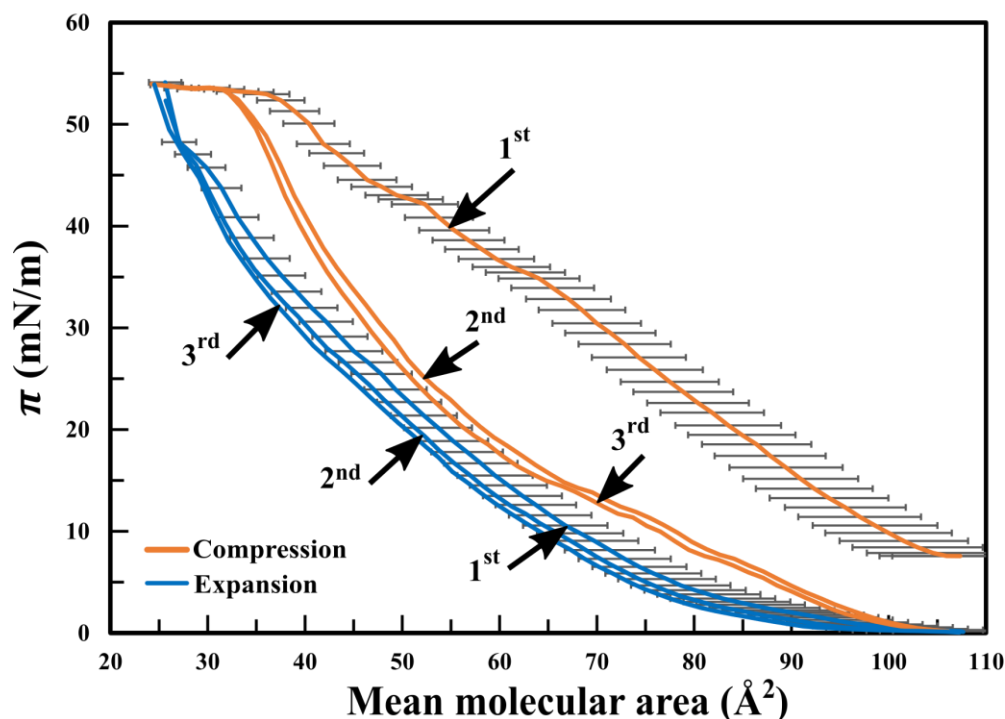


Figure B.5 Surface pressure (π) measurement of relatively concentrated DPPC (0.2 mg/mL) at air-water interface showing three continuous compression-expansion curves. Orange line data shows the consecutive compressions while blue line data shows the consecutive expansions. Arrows indicate the order of compression and expansion. Error bars represent percentage uncertainty of 6.5% in estimating the mean molecular area. For convenience error bars are only provided for the first compression-expansion cycle. Initial surface coverage is ~ 1.1 mg/m².

The data set above is the same experimental data that is shown in Fig. 5a of the main manuscript but with the expansion curves. We observed that after the first compression-expansion cycle, the data is reproducible for the subsequent cycles. This is presumably because the material is re-distributed more homogeneously after the first cycle. Overall, comparison of this measurement with the data presented in Fig. B 3 shows that there is reproducibility in independent measurements.

B.8 DPPC Visualization During Expansion

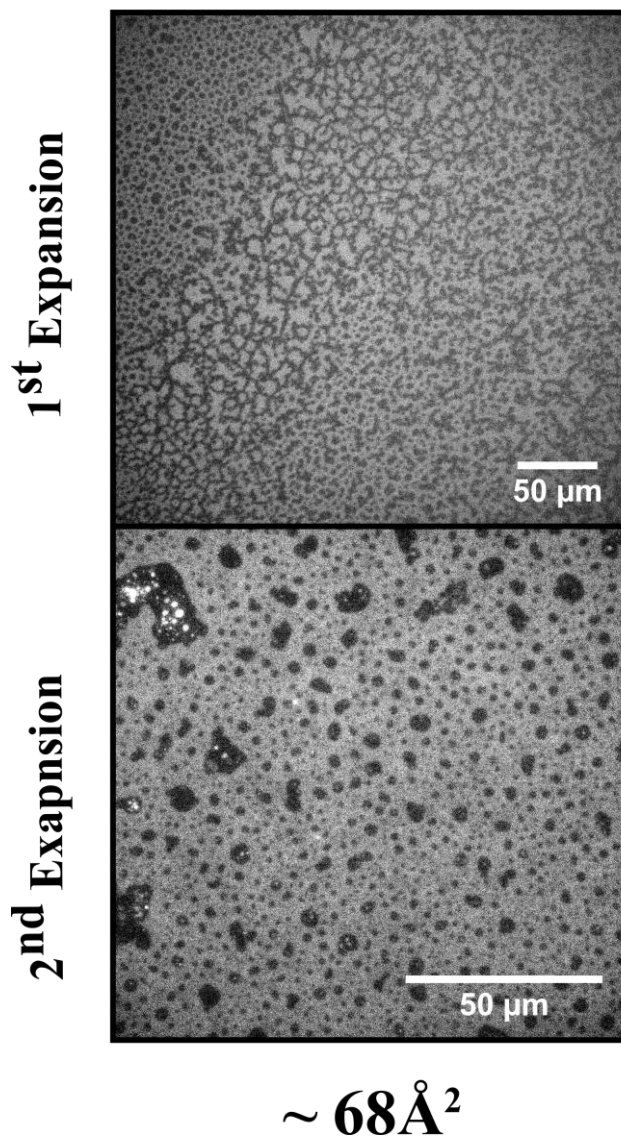


Figure B.6 Micrographs of DPPC at air-water interface during expansion. The images are acquired using radial Langmuir trough and are of the same interface whose compression micrographs are reported in Fig. 6 of main manuscript. 1st expansion is imaged with 40× objective while 2nd expansion was imaged with 100× objective.

B.9 Meniscus Contour Plots/ Interaction of Menisci

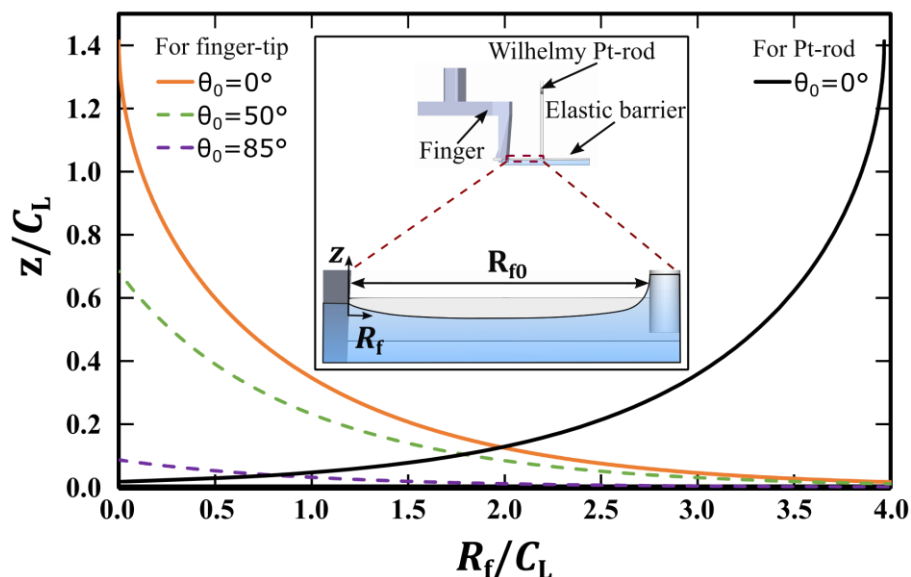


Figure B.7 Theoretical meniscus shape of an air-water interface. Interface pinning height (z) due to meniscus formation is normalized by the capillary length scale (C_L) of water at 20 °C i.e. 2.72 mm, and is plotted as a function of normalized separation distance (R_f) between the Wilhelmy rod and finger-tip. Meniscus shape at the finger-tip and the Wilhelmy rod are calculated separately. The inset illustration qualitatively shows a side view of the meniscus formation at the air-water interface in the presence of the finger-tip, elastic barrier and the Wilhelmy rod. The pinning height (z) as a function of contact angle (θ_0) is calculated for three different values of θ_0 for the finger tips. $\theta_0 = 0^\circ$ (solid orange line) for complete wetting, $\theta_0 = 50^\circ$ (dashed green line) and $\theta_0 = 85^\circ$ (dashed purple line). For the platinum Wilhelmy rod we plot the result for constant contact angle of $\theta_0 = 0^\circ$ (solid black line).

As contact angle changes, so will the shape of any meniscus created by a solid object inserted normal to a fluid-fluid interface. The results above show meniscus shape for a clean air-water interface as it varies with contact angle, with all lengths scaled by C_L . Low contact angles will result in a steep curvature of the interface, as illustrated for the platinum Wilhelmy rod on the secondary y-axis (solid black line), which has $\theta_0 = 0^\circ$, and also for the barrier (primary y-axis) in the case when $\theta_0 = 0^\circ$ (solid orange line). The maximum radial separation ($R_{f0}/C_L \sim 4$) is representative of the situation when the radial Langmuir trough is completely open. Although

the contact angle of the platinum rod cannot be altered, the finger wettability can be changed and will influence the shape of the meniscus. The green dashed line was calculated for a finger contact angle of $\theta_0 = 50^\circ$, and the purple dashed line was calculated for a finger contact angle of $\theta_0 = 85^\circ$. The results above show that if the menisci formed at the finger-tip and at the platinum rod in the radial Langmuir trough interact, then this interaction will be a strong function of the separation distance R_f/C_L .

B.10 Contact Angle Measurement

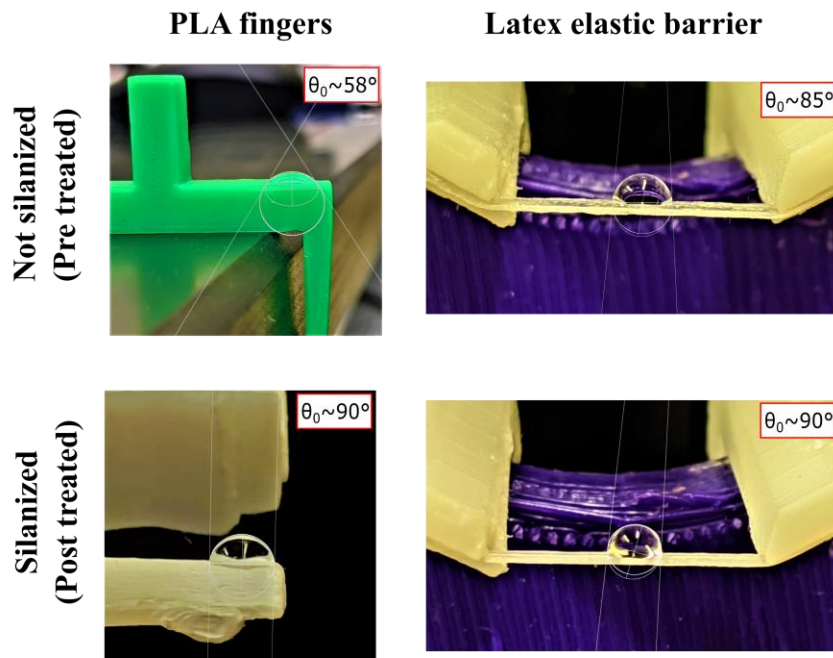


Figure B.8 Contact angle measurement for not silanized (pre-treated) and silanized (post treated) finger and elastic barrier processed using ImageJ software. The estimated value for contact angle (θ_0) is mentioned on the top right corner of each image.

Fig. B 8 shows images acquired for measuring actual contact angles for the trough parts. DI water drop was put on each surface to evaluate the contact angle. The acquired images were processed for contact angle estimation using the ‘Contact Angle’ plugin of ImageJ software. The software puts a tangent line at the three-phase contact point for estimating the contact angle. The average of contact angles obtained from left and right tangent lines are reported as the actual contact angle. This average value is reported on the top right corner of each image in Fig. S 8. We observe that before treating the surfaces they are more hydrophilic, especially the PLA finger. After silanization treatment both surfaces achieve a contact angle close to 90° .

B.11 Combining Clean Water and PtBMA/DPPC Film Compression Measurement

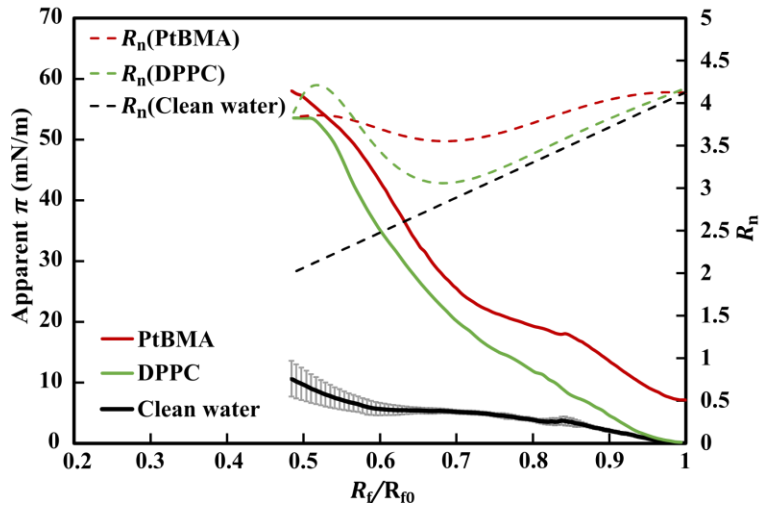


Figure B.9 Apparent surface pressure (π , solid line) during compression, is plotted as a function of the normalized separation distance between the finger tips and the Wilhelmy rod, R_f/R_{f0} , where R_{f0} is the maximum value of R_f . Red, green and black lines are the data set obtained with radial trough for PtBMA at air-water interface (Fig. 3.4a), DPPC at air-water interface (Fig. 3.5b) and clean water (Fig. 3.7) interface respectively. Gray error bars for the clean water data shows the maximum and minimum values of π obtained from two independent measurements. The secondary y-axis represents the normalized capillary radius (R_n , dashed lines). The interface is compressed such that the compression ratio is approximately 4.

Clean water data is obtained after the barrier surfaces were silanized and it shows that as R_n decreases, the apparent π increases. For PtBMA interface, R_n is greater than 3.5 while for DPPC it is greater than 3 during the entire compression.

APPENDIX C

ZABER CONSOLE SCRIPTS

This algorithm is specific to Zaber Console which is a software associated with the linear stepper motor used in construction of the radial Langmuir trough. The code can implement sinusoidal area changes of the with one given frequency and two types of amplitudes.

```
#template(methods);

private const double FREQ = .2;    /* Desired Frequency in Hz */

private const int MAXCYCLES = 5; /* Number of oscillations per frequency */

private const int TIMEBETWEEN = 1000; /* Delay time after reaching OFP (1000 = 1 second)
*/

private const double MSTEP_SIZE = 0.0238125; /* A-LST0250A microstep size, um to
microsteps; when using decimel then write 0.0238125M */

private const double MSTEP_SPEED = 0.01449275; /* Converts microsteps/s to micrometers/s
(Calculated from ZaberSpeedSetting Excel file) */

private const int AMP1 = 2000;    /* Amplitude in um */

private const int AMP2 = 4000;    /* Amplitude in um */

private const int OFP = 12000;    /* OFP means Oscillation Folcrum Position or the
position, in um, that the linear stage will oscillate around */

private const int SET_SPEED = 1000; /* This is the initial speed that the motor will move
to the OFP before oscillations begin, in um/s */

private const double RESOLUTION = 2; /* Use resolution and delay time based on Excel
Sheet for desired Frequency */

private const int DelayTime = 0; /* Excel Sheet Location - C:\Users\samaniuk_a\Colorado
School of Mines\Joseph Samaniuk - Shalaka Kale\Zaber Console Scripts */
```

```

private const double dt = 1/RESOLUTION; /* delta t is the time between every sample */

private const double TotSamples = RESOLUTION/FREQ; /* Total samples in a cycle */

public override void Run()
{
    int Amp1, Amp2 = 0;

    Int32 StartPosition = (int) (OFP/MSTEP_SIZE); /* Make OFP start location */

    Conversation.Request(Command.SetTargetSpeed, (int)
(SET_SPEED/MSTEP_SPEED)); /* Command that sets speed for initial movement to OFP
using SET_SPEED */

        Conversation.Request(Command.MoveAbsolute, StartPosition); /* Command
that moves motor to OFP */

            Sleep (TIMEBETWEEN);

                Amp1 = (int) (AMP1 / MSTEP_SIZE); /* Converts amplitude to microsteps and halves
amplitude each TRIAL */

                    Amp2 = (int) (AMP2 / MSTEP_SIZE); /* Converts amplitude to microsteps and halves
amplitude each TRIAL */

                        double W = (double) FREQ*2*Math.PI; /* converting Hz to rad/s */

                            for (int j = 0; j < MAXCYCLES; j++) /* Outer loop for number of cycles */

                                {

                                    for (int i = 0; i < (int) TotSamples; i++) /* Inner loop for motion, based on speed
and resolution/data points desired [Sampling every cycle] */

                                        {

                                            double Pos_Pre = (double) (Math.Sin(W * dt * i)); /* Calculate the new
position to move to each iteration of inside loop */

```

```

        double Speed_Pre = (double) (Math.Cos(W * dt * i)); /* Calculate
sinusoidal speed, created from derivative of sin, Math.cos uses seconds (C# function) */

        int Speed = (int) ((AMP1 * W * Math.Abs(Speed_Pre))/MSTEP_SPEED);
/* This uses um for AMPLITUDE and converts to microsteps/s with MSTEP_SPEED */

        if (Speed < ((.000015*1000)/(MSTEP_SPEED))) /* The speed resolution
is 0.000015 mm/s, and this makes sure that we do not send a too small of a speed to the motor,
causing error */

        {

            Output.Write(Speed);

            Output.WriteLine();

            continue; /* Checks the i value and restarts loop, without executing
the speed function */

        }

        int Pos = (int) (Amp1 * Pos_Pre + StartPosition); /* Using move absolute
so need StartPosition to keep oscillation around StartPosition */

        if (j == 2)

        {

            Speed = (int) ((AMP2 * W *
Math.Abs(Speed_Pre))/MSTEP_SPEED); /* This uses um for AMPLITUDE and converts to
microsteps/s with MSTEP_SPEED */

            if (Speed < ((.000015*1000)/(MSTEP_SPEED))) /* The speed
resolution is 0.000015 mm/s, and this makes sure that we do not send a too small of a speed to
the motor, causing error */

            {

                Output.Write(Speed);

```

```

        Output.WriteLine();

        continue; /* Checks the i value and restarts loop, without
executing the speed function */

    }

    Pos = (int) (Amp2 * Pos_Pre + StartPosition); /* Using move
absolute so need StartPosition to keep oscillation around StartPosition */

}

    Conversation.Request(Command.SetTargetSpeed, Speed); /* Set speed to
move to next position */

    Conversation.Request(Command.MoveAbsolute, Pos); /* Move to next
position calculated by resolution */

    Sleep (DelayTime); /* Adjustment to get correct cycle time based on
FREQ */

}

    Output.Write("Number of Cycles Completed: "); /* Update Cycle counter to
screen */

    Output.Write((j+1));

    Output.WriteLine();

} /* End of the loop for different cycles within 1 frequency */

    Conversation.Request(Command.MoveAbsolute, StartPosition); /* Command that moves
motor to StartPosition */

    Output.Write("Finished!"); /* All cycles completed */

    Output.WriteLine();

}

```

APPENDIX D

COPYRIGHT PERMISSIONS

This document includes the copyright permissions from the journal and co-authors of two published work.

For “Active particle tracking microrheology using artificial thermal noise”

Shalaka Kale

From: AIPRights Permissions <Rights@aip.org>
Sent: Tuesday, February 1, 2022 9:39 AM
To: Shalaka Kale
Subject: [External] RE: Permission to use JOR's article (first author) in PhD thesis/dissertation

Follow Up Flag: Follow up
Flag Status: Completed

Dear Dr. Kale:

You are permitted to include your published article or portions from it in your thesis, provided you also include a credit line referencing the original publication.

Our preferred format is (please fill in the citation information):

"Reproduced from [FULL CITATION], with the permission of the Society of Rheology."

If the thesis will be available electronically, please include a link to the version of record on the journal site.

Please let us know if you have any questions.

Sincerely,

Susann LoFaso
Manager, Rights & Permissions

AIP Publishing
1305 Walt Whitman Road | Suite 300 | Melville NY 11747-4300 | USA
t +1.516.576.2268
slofaso@aip.org | publishing.aip.org
Follow us: [Facebook](#) | [Twitter](#) | [LinkedIn](#)

From: Shalaka Kale <skkale@mines.edu>
Sent: Thursday, January 27, 2022 6:49 PM
To: AIPRights Permissions <Rights@aip.org>
Subject: Permission to use JOR's article (first author) in PhD thesis/dissertation

Hi there,

I am Shalaka Kale, the first author of one the recent publications in JOR entitled, "Active particle tracking microrheology using artificial thermal noise". I wanted to include this article in parts/as whole in my PhD thesis work. Can you please guide me through the steps to acquire necessary copyright permissions for the same?


Please let me know I you need any additional information from my side or other co-authors/corresponding author.

Thank you and best regards,
Shalaka Kale
PhD Candidate|Soft Matter and Interfaces Lab|Samaniuk Group
CBE Department|Colorado School of Mines
skkale@mines.edu

For “A miniaturized radial Langmuir trough for simultaneous dilatational deformation and interfacial microscopy”

CCC RightsLink®

Home Help Email Support Sign in Create Account



A miniaturized radial Langmuir trough for simultaneous dilatational deformation and interfacial microscopy
Author: Shalaka K. Kale, Andrew J. Cope, David M. Goggin, Joseph R. Samaniuk
Publication: Journal of Colloid and Interface Science
Publisher: Elsevier
Date: 15 January 2021
© 2020 Elsevier Inc. All rights reserved.

Journal Author Rights

Please note that, as the author of this Elsevier article, you retain the right to include it in a thesis or dissertation, provided it is not published commercially. Permission is not required, but please ensure that you reference the journal as the original source. For more information on this and on your other retained rights, please visit: <https://www.elsevier.com/about/our-business/policies/copyright#Author-rights>

[BACK](#) [CLOSE WINDOW](#)

© 2022 Copyright - All Rights Reserved | Copyright Clearance Center, Inc. | Privacy statement | Terms and Conditions
Comments? We would like to hear from you. E-mail us at customer@copyright.com

Shalaka Kale

From: Goggin, David M. (Fed) <david.goggin@nist.gov>
Sent: Monday, March 28, 2022 7:40 AM
To: Shalaka Kale; Drew Cope
Cc: Joseph Samaniuk
Subject: [External] RE: Requesting co-author permission for our radial trough manuscript published in JCIS

Hi Shalaka,

I approve of you using that manuscript in your thesis.

Best,
David

David Goggin, Ph.D.
NRC Postdoctoral Research Associate
National Institute of Standards and Technology (NIST)
Applied Chemicals & Materials Division
Nanoscale Reliability Group
325 Broadway, MS 647 | Boulder, CO 80305 | o: (303) 497-4110 | c: (651) 301-1800

From: Shalaka Kale <skkale@mines.edu>
Sent: Sunday, March 27, 2022 10:29 PM
To: Drew Cope <acope569@gmail.com>; Goggin, David M. (Fed) <david.goggin@nist.gov>
Cc: Joseph Samaniuk <samaniuk@mines.edu>
Subject: Requesting co-author permission for our radial trough manuscript published in JCIS

Hello Andrew and David,

I hope you both are doing well.

I am currently in the process of completing my PhD thesis and I need approval from both of you to include our manuscript entitled, “A miniaturized radial Langmuir trough for simultaneous dilatational deformation and interfacial microscopy” in my thesis.

I would greatly appreciate if you could reply to this email with your approval decision.

Thanks and regards,
Shalaka Kale
PhD Candidate | Soft Matter and Interfaces Lab | Samaniuk Group
CBE Department | Colorado School of Mines
skkale@mines.edu
(720)338-2038

Shalaka Kale

From: Drew Cope <acope569@gmail.com>
Sent: Sunday, March 27, 2022 10:35 PM
To: Shalaka Kale
Cc: Goggin, David M. (Fed); Joseph Samaniuk
Subject: [External] Re: Requesting co-author permission for our radial trough manuscript published in JCIS

Hey Shalaka!

I approve

Thank you,
Andrew Cope

On Sun, Mar 27, 2022, 22:29 Shalaka Kale <skkale@mines.edu> wrote:

Hello Andrew and David,

I hope you both are doing well.

I am currently in the process of completing my PhD thesis and I need approval from both of you to include our manuscript entitled, "A miniaturized radial Langmuir trough for simultaneous dilatational deformation and interfacial microscopy" in my thesis.

I would greatly appreciate if you could reply to this email with your approval decision.

Thanks and regards,

Shalaka Kale

PhD Candidate | Soft Matter and Interfaces Lab | Samaniuk Group

CBE Department | Colorado School of Mines

skkale@mines.edu